Additive Manufacturing of Ti64 Alloy in-situ Modified with Additions of Boron or Oxygen

A thesis

submitted in fulfilment

of the requirements for the degree

of

Doctor of Philosophy in Engineering

at

The University of Waikato

by

Benjamin Ivan Jackson

THE UNIVERSITY OF
WAIKATO
Te Whare Wānanga o Waikato

2022

Abstract

Selective laser melting (SLM) is a metal additive manufacturing process that enables the production of complex, near net shape, parts with fully functional mechanical properties. The use of titanium alloys in SLM is a good fit due to a high material utilisation and net shape production with this expensive material. While titanium alloys have attractive properties of high specific strength and excellent corrosion resistance, these and other attributes may be modified through various methods for further improvements of the material. Strengthening mechanisms of interstitial hardening and particulate reinforcement are viable approaches for enhancing titanium alloys, however these often increase processing difficulty. Near net shape processes, like SLM, have the potential to produce functional parts with these modified properties.

This study explored the use of SLM for the fabrication of titanium parts, modified in-situ during processing with small amounts of boron or oxygen to develop enhanced properties. The in-situ incorporation of these different elements was performed during SLM using blended powders. Simple mixing of feedstock Ti64 alloy powder with small amounts of either amorphous boron or TiO_2, and subsequent SLM consolidation, has the potential to develop interstitial (oxygen) and particulate (boron) strengthened materials.

This work analytically compares the properties of samples created using different process parameters, related through energy density. By examining variation in porosity and hardness with respect to these process parameters, it was possible to establish optimum processing conditions for manufacturing the in-situ modified material. Novel samples were developed for SLM that simplify the multi-level, multi-factor investigation of these process parameters into a single specimen for easy preparation and testing. Further investigation of how processing may influence the distribution and homogeneity of the modified material was studied through the influence of stress relief and sub-beta transus annealing heat treatments. Characterisation of these materials and treatment conditions were

performed to determine the effect the additives have on the mechanical and wear properties.

Most significantly this work demonstrated that small amounts (approx. 0.2 wt%) of boron or oxygen could be effectively combined with Ti64 via SLM processing. Optimised parameters (resulting in energy density of 54.4 J/mm^3) were able to produce high density parts with uniform incorporation. Typical microstructures were developed for SLM produced Ti64, consisting of columnar colonies of fine lamellar martensite that extend in the build direction. Additional oxygen changed this very little, however boron had a significant effect, refining the grain structure and preventing the formation of columnar colonies. Enhancements in compressive strength and hardness resulted from boron or oxygen addition with compressive yield strength increased by up to 10% and 16% respectively. Improvements in these properties were retained in the different heat treatment conditions when compared to unmodified Ti64. While strengthening of Ti64 was achieved by inclusion of the additives, little improvement in wear performance was found.

This work identifies a viable method of modifying properties of titanium through in-situ processes during SLM. The findings of this study will have implications for the production of Ti64 alloys during the SLM processes and may guide future work on developing materials specific for additive manufacturing.

Acknowledgments

This thesis has been made possible only through the fantastic support I have received from so many. Firstly, I would like to thank the fantastic team at TiDA Ltd, for hosting me for the duration of this project. Dr Mike Fry, your encouragement and continued support has kept me going. Thanks for the entertaining conversations/debates we have had along the way, I look forward to many more. Also, thanks to Simon and Dr Aamir for your support on this journey.

To my supervisors from the University of Waikato, Dr Rob Torrens, Dr Leandro Bolzoni, and Dr Fei Yang, your guidance though this project and your patience has been most appreciated. Thank you for keeping me to task despite all the distractions I managed to find along the way.

I would further like to thank those who have assisted with experimental and who have made time to share their expertise. Especially the team in the Callaghan Innovation Advanced Materials group and members of the TiTeNZ research program.

Mum and Dad, I can finally get a real job now. To my brothers, yes, I have finished. You have all been fantastically supportive and kept me sane on this journey.

Most significantly I would like to thank my partner, Dr Chanelle Gavin. We started this journey together on our respective projects, and while mine has been a little longer, you have been right there beside me, supporting, encouraging, and providing the motivation I needed to complete this. I promise to make up for the missed evenings and weekends, we deserve a holiday.

Contents

List of Figures

List of Tables

List of Abbreviations

3D	Three-dimensional
AM	Additive manufacturing
ASTM	American Society for Testing and Materials
BCC	Body centred cubic
BSD	Back scattered diffraction
CP	Commercially pure
DED	Directed energy deposition
EBM	Electron beam melting
EDS	Energy dispersive X-ray spectroscopy
HCP	Hexagonal close packed
IGF	Inert gas fusion
LA ICP-MS	Laser ablation inductively coupled mass spectrometry
LOF	Lack of fusion
MMC	Metal matrix composites
PBF	Powder bed fusion
SE	Secondary Electron
SEM	Scanning electron microscopy
SLM	Selective laser melting
TMC	Titanium matrix composites
XRD	X-ray diffraction

Chapter 1

Introduction and Literature Review

1.1 Titanium and Titanium Alloys

Titanium has many applications and uses in today's society. Its unique combination of material properties, including: specific strength, corrosion resistance, and fatigue performance, make it applicable to a range of industries; these include medical, aerospace, and marine applications.

The majority of elemental titanium is used in its oxide form as whitening and opacifying agents with applications in the paper industry and in paint pigments. Titanium also finds use in steel production as an additive to refine the grain structure and reduce the oxygen content of a number of different alloys [1].

Titanium is the fourth most abundant metallic element on earth, occurring in mineral deposits of rutile and ilmenite [2]. Despite being abundant with desirable material properties, titanium is restricted from wider use due to its complex extraction and difficult processing; making titanium alloys relatively expensive compared to iron and aluminium.

Raw titanium metal is produced through the Kroll process developed in 1932. Titanium oxide in rutile and ilmenite ore is reacted with chlorine and coke to produce titanium tetrachloride. This is further reduced in magnesium to produce titanium metal in a sponge form. Impurities are removed from the sponge through acid leaching or for higher purity, through vacuum distilling. The sponge is sold as such and processed into ingots through a number of melting techniques [3]. Vacuum arc remelting is currently the most common production technique for ingot. Alloying elements are added to the sponge prior to melting to develop the desired alloy composition. Melting is typically performed twice to ensure acceptable homogeneity of the alloy, triple melting is occasionally performed for better uniformity off structure and diffusion of impurities [1].

The most significant property of titanium contributing to cost of refinement is its high reactivity. This further complicates casting processes as many refractory materials can react and add impurities to titanium. Powder metallurgy techniques have been identified as potentially lowering the cost of titanium products [4]. Many powder metallurgy processes are near net shape, reducing machining costs. Lower temperatures for sintering further reduce production costs. The attractive nature of titanium powder processing has led to numerous investigations and development of this field [5]. Specific attention has been paid to the fabrication of titanium matrix composites (TMC's) through powder metallurgy techniques to develop more diverse material properties than can be achieved by the metal and its alloys alone.

Titanium's reactivity means that in the presence of oxygen it rapidly reacts to form a protective titanium oxide passivating layer that prevents further attack. Titanium is also reactive with carbon and nitrogen and will easily form carbides and nitrides when in the presence of these elements at elevated temperatures [1]. The reactivity of titanium causes it to be highly corrosion resistant due to the highly stable reaction products, which form protective coatings. It is impervious to attack from dilute sulphuric and hydrochloric acids along with most organic acids. Hot chloride solutions also have little corrosive effect. Its corrosion resistance has led to applications in salt water environments and chemical processing plants [6].

The most recognised properties of titanium are its high strength to weight ratio and also corrosion resistance. Table 1.1 provides a comparison between the strength of commercially pure (CP) titanium (Grade 2) and its most common commercial alloy Ti64 (Grade 5) with those of common steel and aluminium grades. A density around 40% lower than steel and strength significantly higher than that of Aluminium 6061 clearly identifies titanium as being suited to high strength applications where mass must be minimised, for example aerospace.

Table 1.1: Select properties of common titanium alloys with commercial steel and aluminium grades [7].

Alloy	Ultimate Tensile Strength (MPa)	Density (g/cm^3)	Melting Point (^oC)
Aluminium 6061 T6 Tempered	300	2.70	588
Titanium Grade 2, Annealed	430	4.51	1660
Titanium Ti64 (Grade 5), Annealed	950	4.43	1660
AISI 1080 Steel, Cold Drawn	450	7.87	1370-1400
ASTM A36 Steel Bar	400-550	7.85	1370-1400

1.1.1 The Crystallography of Titanium

Pure titanium exists in a hexagonal close packed (HCP) crystallographic structure, known as alpha phase (α), from room temperature to approximately 890°C. An allotropic transformation occurs at this temperature to body centred cubic (BCC) structure known as beta phase (β), which remains stable up to the melting point (1668°C). The alpha and beta structures are indicated in Figure 1.1. The transition temperature at which this phase change occurs is known as the beta transus temperature. This beta transus temperature can be modified by the addition of alloying elements [8].

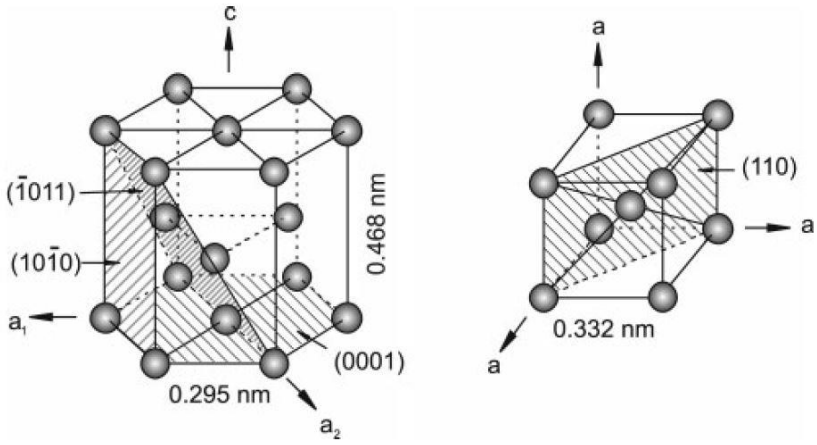

Figure 1.1: Titanium base crystallographic structures. Alpha phase hexagonal close packed (HCP) on the left and beta phase body centred cubic (BCC) structure on the right [8][1].

[1] Republished with permission of John Wiley & Sons, from Titanium and titanium alloys: fundamentals and applications, "Structure and Properties of Titanium and Titanium Alloys", M. Peters, J. Hemptenmacher, J. Kumpfert, C. Leyens, Copyright © 2003 Wiley-VCH Verlag GmbH & Co. KGaA (2003); permission conveyed through Copyright Clearance Centre, Inc.

Additional elements can be combined with titanium in a process called alloying, where these alloying elements result in materials with new combinations of properties. Generally speaking, alloying elements either raise or lower the beta transus and are known as alpha stabilising (aluminium, carbon, nitrogen, and oxygen) and beta stabilising (vanadium and molybdenum) respectively. Alloying elements are also added to refine the grain structure or strengthen the material as a whole. Different combinations of alloying elements give rise to a number of different classes of titanium alloys. Typically these are denoted: alpha, near-alpha, alpha-beta (α+β), and metastable beta [1, 6].

A number of elements have a detrimental effect on many of the properties of titanium and efforts during production and processing are made to minimise these. Embrittlement of titanium is caused by nitrogen and carbon. Oxygen and iron have strengthening effects on the material but with large reductions in ductility. In titanium production these elements must be held to acceptably low levels as their effect on material properties is significant. Occasionally iron and oxygen content will be raised to develop high strength in alloys for specific applications [1, 9].

The allotropic nature of titanium makes the microstructures it forms numerous and fairly complex. Cooling from the beta phase causes the transformation of the close packed bcc plane (110) to that of the alpha HCP basal plane (0001). Twelve different close packed planes/slip directions exist in the beta phase which result in twelve differently orientated alpha lamellae nucleating and growing in a single beta grain. This finite number of alpha orientations gives rise to a basket weave microstructure known as a Widmanstätten pattern (Figure 1.2) within each beta grain [1, 8].

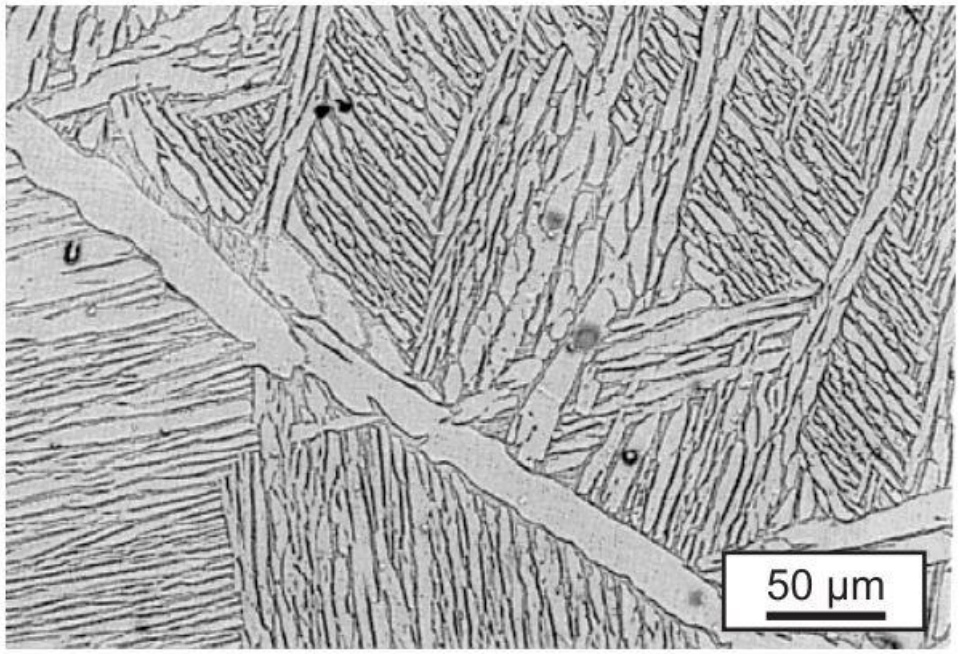

Figure 1.2: Optical micrograph of etched Ti64 material presenting a basket weave Widmanstätten pattern that typically forms from transformed β phase grains [8][2].

Martensitic phases can be induced in titanium alloys with rapid cooling from above the martensite start temperature. A diffusionless transformation of BCC beta to HCP alpha occurs which generates a fine needle like structure in a basket weave pattern as orientations are controlled by the same processes described previously. Two different forms of martensite have been identified. Alpha prime martensite (α') is a hexagonal structure. Alpha double prime (α'') is of super saturated orthorhombic structure. Martensites are unstable at room temperature and will subsequently decompose with heat treatment. Martensite formation does not coincide with embrittlement however does increase strength of the material [8].

1.1.2 Material Properties of Titanium Alloys

Peters, et al. [8] present a chart (Table 1.2) that relates the properties of different classes of titanium alloys. Alpha alloys generally have higher strength, which comes at the cost of ductility. They are also known for corrosion and creep resistance. Beta alloys have increased ductility due to the higher number of slip systems in the BCC structure (twelve) as opposed to only three in HCP alpha.

[2] Republished with permission of John Wiley & Sons, from Titanium and titanium alloys: fundamentals and applications, "Structure and Properties of Titanium and Titanium Alloys", M. Peters, J. Hemptenmacher, J. Kumpfert, C. Leyens, Copyright © 2003 Wiley-VCH Verlag GmbH & Co. KGaA (2003); permission conveyed through Copyright Clearance Centre, Inc.

Table 1.2: Trends in properties for different classes of titanium alloy [8][3].

	Alpha	Alpha-beta	Beta
Density	+	+	-
Strength	-	+	++
Ductility	-/+	+	+/-
Fracture Toughness	+	-/+	+/-
Creep strength	+	+/-	-
Corrosion Behaviour	++	+	+/-
Oxidation behaviour	++	+/-	-
Weldability	+	+/-	-
Cold formability	--	-	-/+

Alpha alloys cannot be heat treated as they only exist as a single phase at room temperature and offer no opportunity for a phase transformation to modify the materials structure. Alpha-beta alloys have both titanium phases present at room temperature. Through heat treatment, the presentation of these phases can be varied greatly, resulting in significant changes in material properties. The response of an alpha-beta alloy, Ti64, to three heat treatments are given in Table 1.3. Different heat treatments can cause the strength of Ti64 to change by up to 200 MPa and create changes in ductility, where the most ductile material presents with lower strength. This makes the heat treatment conditioning of Ti64 especially critical when considering its application. Beta alloys contain enough beta stabilisers to maintain beta phase at room temperature, however solution treating and ageing can also modify the strength of these alloys.

[3] Republished with permission of John Wiley & Sons, from Titanium and titanium alloys: fundamentals and applications, "Structure and Properties of Titanium and Titanium Alloys", M. Peters, J. Hemptenmacher, J. Kumpfert, C. Leyens, Copyright © 2003 Wiley-VCH Verlag GmbH & Co. KGaA (2003); permission conveyed through Copyright Clearance Centre, Inc.

Table 1.3: Effect of standard heat treatments on Ti64 [1].

Condition	Yield Strength (MPa)	Tensile Strength (MPa)	Elongation to fracture (%)
Duplex annealed	917	965	18
Mill annealed	945	1069	10
Solution treated +aged	1103	1151	13

Of all titanium alloys, the most common is the alpha-beta alloy Ti64 (Grade 5) due to its excellent balance between properties and formability. Post fabrication heat treatments can be performed to further modify its properties to suit many applications. This material accounts for approximately half of produced titanium metal [10]. Ti64 is an alloy that incorporates approximately 6wt% aluminium and 4wt% vanadium to develop alpha-beta alloy properties. The composition of this alloy is defined in the ASTM B348 standard and listed in Table 1.4 [11]. An extra low interstitial (ELI) version of this alloy is also available (Grade 23) where impurities, specifically oxygen content, are more carefully controlled. Select mechanical properties of these alloy grades are presented in Table 1.5. With only slightly reduced oxygen content, the yield strength of Ti64 ELI material is reduced significantly (up to 150 MPa below Grade 5 Ti64). This identifies how small differences in oxygen content can have significant effects on titanium's material properties. This sensitivity of titanium to oxygen is another factor that contributes to its high cost as material refining must take place where oxygen and other contaminants are controlled to a very high standard.

Table 1.4: Typical composition of Ti64 alloy [1, 11].

	Alloying Elements wt%		**Impurity limits, wt% max**				
	Al	V	N	C	H	Fe	O
Ti64 (Grade 5)	5.5-6.75	3.5-4.5	0.05	0.08	0.015	0.4	0.2
Ti64 ELI (Grade 23)	5.5-6.5	3.5-4.5	0.03	0.08	0.0125	0.25	0.13

Table 1.5: Ti64 Grade 5 and Grade 23 mechanical properties for annealed condition material [1]

Alloy	Tensile Strength (MPa)	0.2% Yield Strength (MPa)	Elongation (%)	Young's Modulus (GPa)
Ti64 (Grade 5)	900-993	830-924	14	110-146
Ti64 ELI (Grade 23)	830-896	760-827	15	110-146

While titanium alloys have many desirable mechanical properties, they show poor tribological performance. This is especially notable as titanium's biocompatibility encourages its use in medical implants such as joint replacements where wear performance is critical. These properties have limited the application of titanium directly in wear applications [12].

Characteristics of titanium alloys tribological performance include: high coefficients of friction, severe adhesive wear, low abrasion resistance, and a tendency to seize. Mechanisms contributing to these poor wear properties have been identified as [13, 14]:

- Low thermal conductivity causing the contact patch to get hot which reduces local mechanical properties and encourages chemical erosion.
- Reactivity of titanium causing severe adhesive wear with incompatible materials.
- The oxide film responsible for titanium's corrosion resistance has a low shear strength so is broken under wearing conditions. A new oxide film reforms and the process repeats, causing significant damage over time. The disrupted oxide debris further accelerates wear by changing the mechanism to three-body abrasion.

Methods to modify the base properties of titanium alloys are in constant development. Investigating how the material may be improved results in new applications that benefit from other unique properties that titanium carries. Aside from alloying, some methods that are used to modify titanium include: coatings, diffusion hardening treatments, and metal matrix composites. Properties often targeted for improvement include hardness and wear resistance.

1.2 Modified Titanium Alloys

1.2.1 Titanium Matrix Composites (TMC)

Metal matrix composites (MMC's) are a group of materials that consist of a reinforcing fibre, whisker, or particulate in a ductile metal matrix for the development of modified material properties. These composites are developed for a number of property enhancements. The improvement of thermal stability, specific modulus, strength, and wear resistance in MMC's has been reported on by Tjong and Ma [15]. Through combining the strength and stiffness of ceramics with the properties of metals, improvements in shear, compression, wear, and service temperature can be achieved [16, 17]. One large development area is improving the specific properties of light metals and alloys for use in products where weight is a critical factor. Industries that make use of these alloys include aerospace and motorsport. Aluminium alloy MMC's have been applied in a number of automotive applications including fibre reinforced pistons and crank cases. Titanium MMCs have also been developed for these industries and been applied in landing gear and valve components [18, 19].

Materials selection for a MMC system is critical to ensuring performance enhancement of the product. Key factors that must be considered for selecting a suitable reinforcement material for use in a metal matrix include[16]:

- Superior mechanical properties such as stiffness, hardness and strength.
- Physical material properties of melting point, density, and solubility in the metal matrix.
- Thermal expansion coefficient should closely match that of the metal matrix to prevent stress cracking during heat cycles.
- Thermodynamic stability in the matrix at elevated temperatures that will occur during processing and use.

Various ceramics meet all the criteria for reinforcing materials in MMCs. The properties of some common types of reinforcement are listed in Table 1.6. These reinforcements exhibit a range of thermal expansion coefficients to match with a chosen matrix material. For MMC's, processing is often at elevated temperature

(sintering or casting), so stability of the reinforcement must be considered not only for service temperatures but for fabrication.

Table 1.6: Select properties of reinforcement materials commonly used in MMCs [16, 20].

	Density ($g.cm^{-3}$)	Thermal Expansion Coeff. ($10^{-6}\ ^oK^{-1}$)	Tensile Strength (MPa)	Elastic Modulus (GPa)
Al_2O_3	3.98	7.92	221 (1090°C)	379 (1090°C)
B_4C	2.52	6.08	2759 (24°C)	448 (24°C)
Si	2.33	3.06	(varied)	112
SiC	3.21	5.40	(varied)	324 (1090°C)
WC	15.63	5.09	(varied)	669 (24°C)
TiC	4.93	7.60	118.6 (1000°C)	439.43 (24°C)
TiB_2	4.50	8.28	529	414 (1090°C)
TiB	4.56	11.32	(varied)	427

MMC's can be made using continuous or discontinuous reinforcement. Continuous reinforcement uses long fibres aligned in the matrix to achieve directionally enhanced properties. These fibres are used in the form of monofilaments or fibre tows. Discontinuous reinforcement occurs through small whiskers or particulates evenly distributed throughout the MMC. These particulates can be incorporated into the matrix material by adding the particulates themselves (ex-situ) or be the result of reactions and precipitation that takes place between the matrix and elements present during processing (in-situ).

Titanium, with its very high specific strength and corrosion resistance is a viable material for replacing steel and other high strength alloys in aerospace and other weight critical applications. It has been the focus of large research efforts in terms of developing titanium matrix composite (TMC) materials. The properties typically displayed for TMC's include corrosion resistance, thermal stability, and high specific properties of modulus and strength [21]. Investigations have also focused on improving other properties including wear resistance and creep resistance [22]. Both continuous and discontinuous reinforcement have been developed to achieve these ends.

1.2.1.1 TMC Continuous Reinforcement

Continuous reinforcement of titanium occurs via ex-situ processes and was the focus of early work in this area with a number of different materials considered [23]. Carbon fibre tows proved too costly as a reinforcement of titanium due to severe chemical reactions between the fibre and matrix during processing that damaged the fibres and eliminated any benefits of the reinforcement [18]. Alumina (Al_2O_3) fibre reinforcement of titanium has also been considered. The alumina fibres are chemically unstable in a titanium matrix and degrade during processing and service. This degradation led to developments in thin unreactive coatings for alumina fibres to prevent chemical attack. Nano thickness Nb and Y_2O_3 coatings on the alumina showed no reactions between the matrix and fibre. Despite the successful coatings the difficulties of achieving homogeneity with fibre alignment and coating has made the method of fibre tow reinforced titanium unviable [18].

Monofilament reinforcement has taken preference as the continuous reinforcing method for TMC's, the most viable material has been silicon carbide. This reinforcement is not chemically stable in a titanium matrix and pyrocarbon coatings are commercially used to provide a barrier to chemical attack. This still develops a brittle reaction zone surrounding the fibre, the thickness of which is dependent upon time held at elevated temperatures. Despite the mismatch of thermal expansion coefficient and reactivity, silicon carbide monofilaments are still the primary continuous reinforcement used for TMC's [24]. Applications of this material have included landing struts for the F16 Jet Fighter [25].

1.2.1.2 TMC Discontinuous Reinforcement

Discontinuous reinforcement of titanium has also been investigated for several reinforcing materials. Benefits of discontinuous reinforcement include enhanced mechanical properties, isotropy of properties, and economic benefits in production and secondary processing. Specific enhancements of discontinuous TMC's include increased creep resistance and wear resistance [22, 26].

Chemical stability issues have prevented the use of some common discontinuous reinforcements including alumina and carbon. With these materials added as ex-

situ particulates, reactions occur at the interface resulting in brittle products and reduced interfacial strength. Protective coatings have been considered however applying these to particulates is a difficult process and not cost effective [27]. Although titanium's reactivity eliminates several common reinforcements via ex-situ processes there is good compatibility with other materials that offer excellent properties, and many can be incorporated via in-situ processes. Some reinforcements with application in titanium are listed in Table 1.7 along with select properties. There is a close match between the thermal expansion coefficient of titanium and many of these reinforcements suggesting they are suitable materials for TMC's. High hardness of the particulates also suggests that reinforcement of the titanium matrix could be considerable.

Table 1.7: Comparison between properties of reinforcements with application in a titanium matrix [28].

	Ti	TiB	TiB_2	TiC	TiN	B_4C	SiC
Density ($g.cm^{-3}$)	4.57	4.56	4.52	4.92	5.43	2.51	3.19
Elastic modulus (GPa)	110	371	540	450	390	445	430
Thermal expansion at room temp. ($x10^{-6}$ K^{-1})	8.6	7.15	6.2	7.95	9.35	4.78	4.63
Melting/decomposition Temp. (^oC)	1668	2200	2970	3054	3220	2720	2970
Vickers hardness (kg/mm^2)	150	1800	2200	3200	2300	3870	2500

A number of the discontinuous reinforcements listed in Table 1.7 are suitable for titanium as they are a product of reactions between the titanium matrix and other elements (TiB, TiC). An in-situ particulate generation process can be used for these materials where the reinforcement is the final stable product of a complete reaction with titanium. For in-situ processing the solubility of the elements in titanium across the full range of processing and service temperatures, as well as alternative, undesirable, reaction products must be considered.

1.2.1.3 Boron Compound Discontinuous Reinforcement of Titanium

Of the previously mentioned discontinuous reinforcements, compounds of boron and titanium offer great potential as titanium reinforcement materials. Titanium forms three intermetallic boron compounds with titanium: TiB_2, Ti_3B_4, and TiB. The

phase diagram in Figure 1.3 indicates the transition concentrations and temperatures at which these Ti-B compounds form [29].

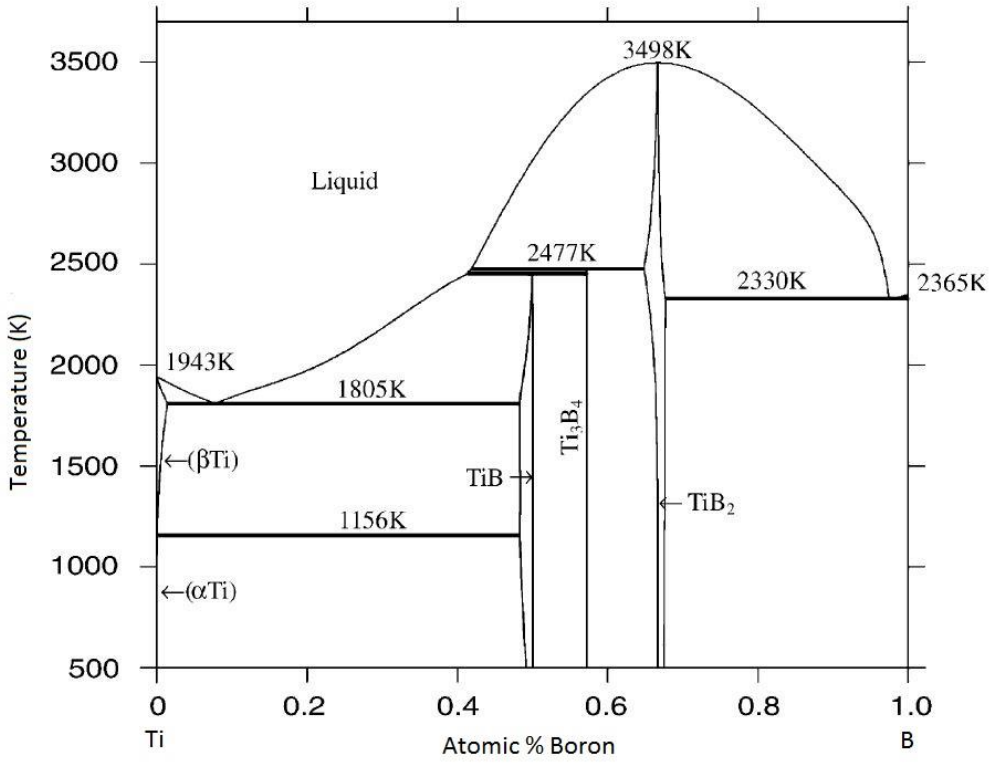

Figure 1.3: Titanium-Boron phase diagram [29][4].

The eutectic point seen in the titanium rich sector of the Ti-B phase diagram occurs at 1532°C and 1.64 wt% boron (6.9 at%). The eutectic point discussed is for the addition of boron to pure titanium. Alloying elements added to the material can cause this to shift, for Ti64 this eutectic point is similar to pure titanium at 1.55 wt% boron (6.5 at%). The solubility of boron in solid titanium is very low for both alpha and beta phases however is completely soluble in liquid phase, which is highly advantageous for processing [30]. This enables boron to be blended into the melt of titanium and during solidification, titanium can react and form the in-situ discontinuous particulates.

TiB_2 has attractive properties for using as a reinforcing material in a titanium matrix. These include high hardness of 3000 kg/mm^2, high melting point 3000°C

[4] Republished with permission of Elsevier Science & Technology Journals, from Journal of Alloys and Compounds, "Thermodynamic assessment of the Ti–B system", X. Ma, C. Li, Z. Du, W. Zhang, Copyright © 2003 Elsevier B.V. (2004); permission conveyed through Copyright Clearance Centre, Inc.

and modulus of 540 GPa. Issues using TiB_2 in titanium matrix arise as the brittle Ti_3B_4 easily forms at the interface during processing which greatly reduces the strength of the compound [28].

Titanium mono-boride (TiB) has been recognised as potentially the most advantageous reinforcement of titanium alloys with reviews summarising research into formation, properties, and applications performed by a number of researchers with [31-34]. Its high hardness, high elastic modulus, low solubility, and thermal expansion coefficient close to that of titanium, make it a clear choice for use in the discontinuous reinforcement of TMCs.

TiB exhibits high stability in a titanium matrix without forming intermediate phases at the interface and has excellent crystallographic compatibility. This results in good adhesion between the two materials [30]. TiB also holds an economic advantage over other titanium compounds considered for reinforcement as solid-state synthesis can take place at low temperatures of between 900-1300^{o}C. Perhaps the most advantageous property is that TiB naturally forms single crystal whiskers (particulates with high length to width ratio) in a titanium matrix. Whisker reinforcement offers greater improvements in stiffness and strength than other discontinuous reinforcement [28].

The reaction chemistry for TiB composites has been well studied. Favourable reactions between the titanium matrix and a number of boron containing additive materials exist such that boron reinforcement materials can be generated in-situ during processing. These include TiB_2, pure B, CrB, and B_4C [34]. Titanium and boron can react in solid state, making fabrication through in-situ powder metallurgy processes viable such as reactive hot pressing and powder extrusion [26, 34]. Due to the high solubility of boron in liquid titanium, solution precipitation is favourable for in situ-TiB formation, where particulates react and precipitate during solidification, this also occurs under rapid solidification processes. Cai, et al. [22] reports the reactions that occur for in-situ synthesis of TiB in excess titanium are as follows with Gibbs free energy of reaction values also given for each:

$$\mathrm{Ti} + \mathrm{B} \rightarrow \mathrm{TiB} \;\; \Delta\mathrm{G}(\mathrm{R}, 1000\mathrm{K}) = -157\ \mathrm{kJ/mol}$$ **Equation 1.1**

$$\mathrm{Ti} + 2\mathrm{B} \rightarrow \mathrm{TiB_2}\ \Delta\mathrm{G}(\mathrm{R}, 1000\mathrm{K}) = -308\ \mathrm{kJ/mol}$$ **Equation 1.2**

$$\mathrm{Ti} + \mathrm{TiB_2} \rightarrow 2\mathrm{TiB} \;\; \Delta\mathrm{G}(\mathrm{R}, 1000\mathrm{K}) = -6.3\ \mathrm{kJ/mol}$$ **Equation 1.3**

The negative Gibbs free energy of Equation 1.1, 1.2, 1.3 indicates that both reactions to form TiB and TiB_2 will proceed. However, Cai, et al. [22] and Zhang et al. [35] establish that in excess titanium the decomposition of TiB_2 into TiB will occur as the Gibbs free energy of this reaction is also negative, making TiB the more stable reinforcing material.

TiB forms as a mixture of both B27 orthorhombic phase and metastable B_f crystals. Intimate mixing of these two structures is possible as B27(200) plane exactly mates with the $B_f(110)$ or $(1\bar{1}0)$ (with B27[010]//B_f[001]) [36]. In experiments where TiB is produced in the rapid solidification process of laser cladding on a titanium alloy substrate, three different morphologies of TiB are observed: fine needles (200 nm by 15 µm), plates (1 µm by 3 µm by 15 µm), and coarse single needles or whiskers (3 µm by 50 µm). The single whisker morphology develops in TiB as the growth rate is fastest in the (010) direction [34].

The properties of TiB can only be determined through approximation or estimated through multi-phase systems such as Ti-TiB composites as a single component sample of TiB for experimentation is yet to be produced. This difficulty arises as pure TiB forms at a peritectic point from liquid Ti and TiB_2 at 50 at% as indicated in the phase diagram (Figure 1.3).

In determining the stiffness of TiB whiskers the Tsai-Halpin theory has been successfully used by Atri et al. [37]. Varying volume fractions of TiB in titanium matrix were used to estimate the elastic modulus of TiB at 371 GPa. Suggestions have been made that TiB whiskers may exhibit elastic anisotropy due to the whisker morphology and growth characteristics. Gorsse and Miracle [33] again applied the Tsai-Halpin equation to this problem. Estimates were made for the transverse and longitudinal elastic moduli from measurements made on samples

with a high degree of whisker alignment. Transverse and longitudinal moduli were estimated at 450 GPa and 514 GPa respectively resulting in polycrystalline modulus of 482 GPa, much higher than previous models. Microstructural texture may have resulted in incorrect back-calculation as extrusion was used as the means to align the fibres. The extrusion textured titanium matrix would have a higher stiffness in the extruded direction and as such overestimation of the reinforcement stiffness would result.

Thermal expansion coefficient is a critical property required for determining the compatibility between matrix and reinforcement. The most accurate method of determining this is from single crystals for determination of thermal expansion coefficient in principle crystallographic directions. Single crystals are yet to be produced for TiB and, as with stiffness, this has had to be approximated from TiB rich material. Estimates based on this material have determined an expansion coefficient of 7.45×10^{-6}/K at room temperature and 11.6×10^{-6}/K at 1625K [28].

The nature of the single crystal whisker morphology of TiB in titanium has seen dramatic increases in stiffness when relatively high proportions of TiB have been used. With 10vol% TiB an increase in elastic modulus of 20-25% was achieved by Godfrey et al. [38]. Gorsse et al. [39] reported TMC's containing 20% volume TiB achieved near 50% increase in Young's Modulus. With increasing volume fraction of TiB stiffness increases, however this is at the expense of ductility. Volume reinforcement of 30% typically results in very little, if any, ductility [34].

Strength of Ti-TiB composites varies greatly depending on composition. Values in ultimate tensile strength range between 673 MPa and 1820 MPa. Saito, et al. [4] provide an in depth study into the strength of TiB whisker reinforced commercially pure titanium. Compositions containing 10, 20 and 30vol% show ultimate strength increases from 1080 MPa to 1820 MPa, more than double that of wrought CP titanium, which typically exhibits ultimate strength of 550 MPa. Numerous investigations involving TiB reinforcement of titanium have been performed through many different methods. Morsi and Patel [34] have tabulated many of the mechanical property results from these studies for comparison. These tables can be found in the appendix at the end of this thesis.

Small boron additions to titanium have demonstrated significant refinement in grain size. Tamirisakandala et al. [40] investigated this mechanism and proposed it was due to TiB precipitating at beta grain boundaries during solidification of titanium, pinning them and forcing the initiation of new grains rather than the growth of existing ones. This formed the structures seen in as-cast material where TiB particles were observed at the prior beta grain boundaries.

This grain refining effect is seen with very low additions of boron. In cast Ti64, low additions of boron (0.1 wt%) were seen to reduce the average grain size from 1700 µm to less than 200 µm as presented in Figure 1.4. Above 0.1 wt% boron, little further effect on reducing grain size was observed [40].

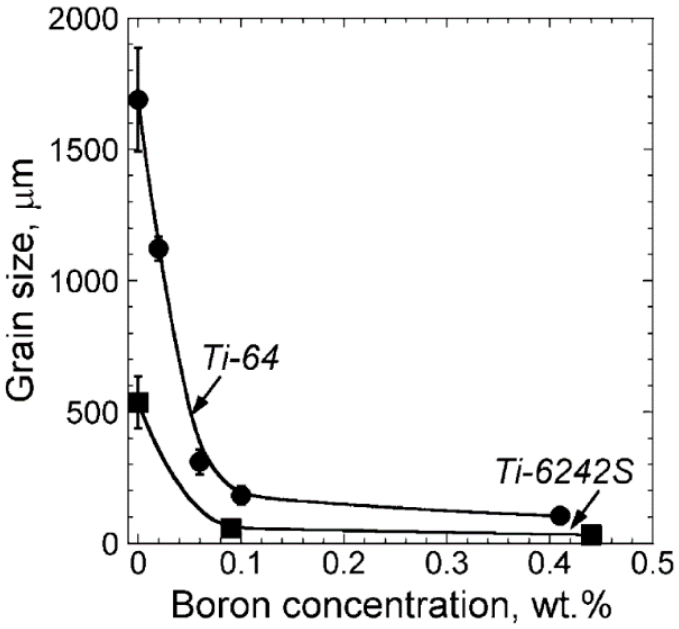

Figure 1.4: Grain refinement in titanium alloys with small boron additions [40][5].

The influence of low percentage boron additions on various properties have been studied. Additions of boron to cast titanium alloys have been explored between the ranges of 0.01 wt% and 2.5 wt% by Bilous et al. [41]. Below 0.05 wt% the plasticity of the material was improved. Higher boron additions, up to 2.5 wt%, resulted in hardness and yield strength increases, up to two times higher than the

[5] Republished with permission of Elsevier Science & Technology Journals, from Scripta Materialia, "Grain refinement of cast titanium alloys via trace boron addition", S. Tamirisakandala, R.B. Bhat, J.S. Tiley, D.B. Miracle, Copyright © 2005 Acta Materialia Inc. (2005); permission conveyed through Copyright Clearance Centre, Inc.

unmodified alloy. Sen et al. [42] investigated additions of boron up to 0.55 wt% in cast Ti64 with increases in tensile strength observed. This increase in strength corresponded with reduction in ductility, which presented when more than 0.1 wt% boron was added.

The fatigue properties of boron modified Ti64 were investigated by Chen and Boehlert [43] as well as Sen et al. [44]. High cycle fatigue strength was improved by up to 50% with boron additions of 0.55 wt%. It was expected that a finer grain structure would improve the fatigue properties, however the enhancement in fatigue was attributed more to the presence of TiB particles. It was concluded that the strong interface between the titanium matrix and TiB could hinder crack initiation for improved fatigue performance.

One of the major driving factors for adding TiB to titanium alloys is to try and improve the poor tribological properties of titanium. Investment casting of CP Ti and B_4C has been used to fabricate TiB+TiC composites for investigation of wear properties. Additions of B_4C (between 1 and 4 wt%) were made to Grade 2 CP titanium with in-situ synthesis of the TiB and TiC occurring during the casting process, following which the wear characteristics were investigated. Wear damage was reduced by the reinforcement addition which was attributed to the overall material hardness increase resulting from reinforcement particles. Reduced crack propagation was also suggested as a mechanism for improved wear resistance in the reinforced material as this would reduce debris generation [45].

Alman and Hawk [46] investigated the abrasive wear (pin on garnet abrasive drum) properties of sintered TMC's reinforced with: carbides, borides, and silicon nitride. All materials had an improvement in wear resistance, also attributed to an increase in hardness and the strength of the interface between the matrix and reinforcing phases.

1.2.2 Interstitial and Diffusion Hardening of Titanium

Another process investigated for modifying the properties of titanium is interstitial and diffusion hardening. This is employed using elements that have increased solubility in titanium where the role of the added elements is not to precipitate as particulates but to form a solid solution. The solute element interacts with the

metallic crystal lattice disrupting dislocation slip [47, 48]. Oxygen and nitrogen are two such elements employed for interstitial hardening and strengthening of titanium.

This process can also be called diffusion hardening as interstitial elements with high solubility are intentionally diffused within titanium during processing. Diffusion hardening can be employed as a coating process by thermal treatment of titanium with a high concentration of the solute present at the surface of the material. For example, heat treating titanium in a nitrogen atmosphere. Diffusion coatings produce a graded hardness profile into the substrate that is dependent on the concentration of solute. Where concentrations of the solute are greater than the elements' solubility, such as the surface of titanium in the nitrogen diffusion coating example, compounds of the solute and titanium form [49]. Continuing through this review, the specific influence of oxygen on titanium will be explored as it is a subject of this work.

The maximum solubility for oxygen in alpha-titanium is approximately 33 at%, the highest of any metal. This is seen in the titanium-oxygen phase diagram Figure 1.5. In beta-titanium phase the solubility of oxygen drops to a maximum of about 8 at%[50]. It can also be determined from the phase diagram that oxygen is an alpha stabiliser as the alpha to beta transition is eliminated at higher oxygen levels. Being alpha stabilising also adds to the strengthening effect oxygen has in α+β titanium alloys such as Ti64. Increased oxygen will increase the proportion of alpha phase present [51]. As alpha phase is the stronger titanium phase this typically presents as an increase in material strength.

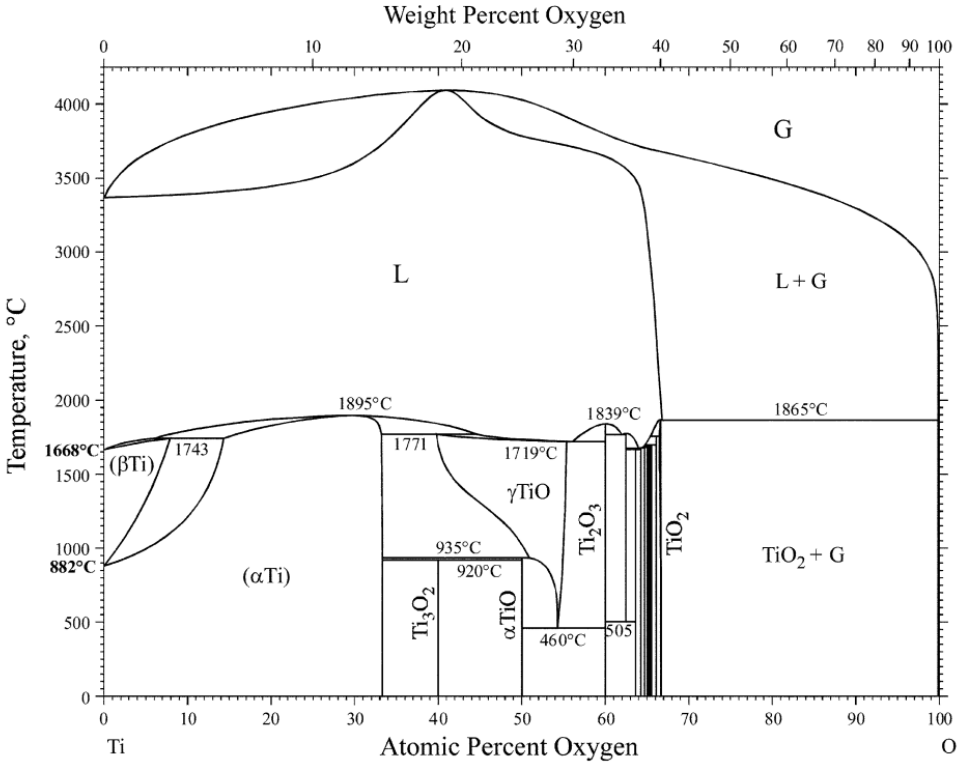

Figure 1.5: Titanium-Oxygen phase diagram [50][6].

An increase in strength and hardness with corresponding drop in ductility is typical with increasing oxygen content up to a threshold of approximately 0.4 wt% depending on material processing. Petunina [52] found that an oxygen content of 0.41 wt% increased the tensile strength of rolled, forged, titanium rods to the same degree as only 0.105 wt% nitrogen. Greater than these amounts caused a sharp decline in tensile strength and elongation. Simbi and Scully [53] also found that up to 0.4 wt% oxygen could improve the strength of CP titanium.

When working with Ti64 alloy it has been noted that the influence of alloying elements can have significant effects on interstitial hardening. Forged and annealed titanium alloys with aluminium content greater than 3-4 wt% require oxygen content less than 0.35 wt% to maintain some ductility. This is due to the solubility of aluminium being reduced in titanium alloys with increased oxygen and the influence of oxygen and aluminium both being alpha stabilising elements [54]. Again, this is dependent on specific processing of the material.

[6] Reprinted by permission from Springer Nature: Journal of Phase Equilibria (and diffusion), "O-Ti (Oxygen-Titanium)", H. Okamoto, Copyright © 2011, ASM International (2011); permission conveyed through Copyright Clearance Centre, Inc.

Jones et al. [55] made small additions of TiO_2 up to 1.5 wt% to Ti64 alloy using spark plasma sintering and extrusion. Differences in mechanical properties were studied along with ballistic performance, as compared with Ti64 rolled plate. A notable increase in UTS and yield strength was observed while elongation was reduced. These differences were attributed to a combination of grain refinement and the additional oxygen content, with oxygen increase being the more significant factor. An 8% improvement in ballistic performance over rolled Ti64 plate was also reported.

As with the discontinuous reinforcement, interstitial hardening through the increase in oxygen content impacts the wear performance of titanium materials. As wear performance is primarily a surface property, investigation of surface oxygen diffusion coatings have been studied to identify differences in wear behaviour. These coatings have been identified as causing a reduction in the wear rate of titanium with less adhesive wear taking place. The effect of oxygen content on the tribological characteristics of titanium after isothermal surface oxidation were investigated by Aniołek et al. [56]. This treatment increased resistance to dry sliding wear of grade 2 titanium, reducing volumetric wear by up to 61%. While this is beneficial, any breakdown of the hardened oxygen diffusion layer quickly propagates and degrades wear performance to that of the original titanium alloy [57, 58].

Kümmel et al. [59] investigated the wear performance of Ti64, coated with an oxygen diffusion layer. By grinding away specific amounts of the diffusion coated surface prior to testing, the effect different oxygen concentrations had on wear performance could be identified. Hardness and oxygen content decreased exponentially, approaching bulk material levels at a depth of 30μm. The wear rate was reduced close to the surface (10μm depth) where oxygen content was high. Beyond 10μm below the surface there was a step change in wear behaviour with the wear rate approaching that of the bulk Ti64. This indicates there may be a threshold level of oxygen content, below which wear properties are not significantly impacted.

When seeking to strengthen titanium alloys by incorporating additives both particulate inclusion and interstation/diffusion strengthening have been shown to be effective. Specific manufacturing conditions can change how these modifications can perform and many different processes can be used for generation of these modified materials. Additionally, titanium wear behaviour can be modified through particulate and interstitial modification, which is the subject of an expanding amount of research. Wear performance is also highly sensitive to the material condition and specific wearing application. In particular, the counterbody, loading, system dynamics, and environment can all have significant impact on a materials wearing behaviour [60].

Metal additive manufacturing (AM) is one such method that provides some valuable benefits including net shape production. In-situ processing of blended powder feedstocks can also be used for development of particulates as well as diffusion strengthening. The impact of this processing on wear performance of the modified materials requires characterisation. Details on additive manufacturing technologies and the application to producing modified titanium alloys are covered in the following section.

1.3 Metal Additive Manufacturing

All current commercial technologies for the additive manufacture of metals use a similar process of fabricating parts layer by layer to achieve the full 3D part. These processes start with a 3D digital model of the part to be manufactured. This is then post processed into layer/slice information for the additive manufacturing machine. This slice information provides the machine with the processing paths required to generate the surfaces and solid sections of the part. An energy source, often a laser or electron beam, is used to melt and consolidate a metal feedstock such as a powder, in accordance with the processing paths to build 3D parts. A number of different technologies have been commercialised, the most common being directed energy deposition (DED) and powder bed fusion (PBF) processes

1.3.1 Directed Energy Deposition (DED) Technologies

DED processes are typically defined by the simultaneous application of heat and feedstock material alongside one another. The metal feedstock materials can be

in the form of wire, powder, or both which are fed or directed into a melt pool established by the energy source. This energy source can be a plasma arc, laser, or electron beam. The energy source and material feed system are typically combined in a deposition head which is moved over the printing surface. They are characterised by high build rates (kg/hour) targeted at producing large near net shape parts that require additional post processing for finishing.

1.3.2 Powder Bed Fusion (PBF) Technologies

PBF uses a metal powder as feedstock material and electron beam or laser as the heat input. The energy beam is used to melt consecutive layers of metal powder in accordance with part slice data. Powder is spread evenly on the build platform via a sweeping recoating mechanism. The heat source is then scanned over the powder layer to selectively melt and consolidate it to build up the part. After each layer exposure is complete the build platform lowers in accordance with the programmed layer thickness and a new powder layer is deposited. The process repeats until the part is completed. As the name suggests, electron beam melting (EBM) uses an electron beam as the energy input. A high vacuum is required in the build chamber as electrons are refracted and deflected by atoms in the atmosphere, which reduces the focus of the beam. Selective laser melting (SLM) uses lasers as the energy source and can operate within a chamber of inert gas.

The SLM process is the focus of this research and is the ongoing subject of this review. Similar ideas and concepts can be applied to the other AM technologies described previously but are not specified.

1.3.3 Selective Laser Melting (SLM)

1.3.3.1 SLM Process Properties

Figure 1.6 demonstrates the build process and chamber layout in SLM. Typically, layers between 20 µm to 100 µm are used depending on the material and powder particle size. SLM is capable of fabricating parts to tolerances of 30-50 µm depending on part geometry. Maximum part sizes are limited by the build chamber. Current machines on the market such as the SLM280HL have build volumes of 280x280x350 mm^3 [61]. Developments are on-going to increase the build volumes to allow larger parts and greater production volumes. SLM is often

mistakenly called selective laser sintering (SLS) or laser sintering (LS). Historically laser technology did not enable full melting of metal powders. The process of SLS partially melted and consolidated the powder (hence sintering) which requires post processing to achieve full density and strength. The development of high-powered fibre lasers allowed full melting of the powder which is capable of producing fully dense, full functionality parts.

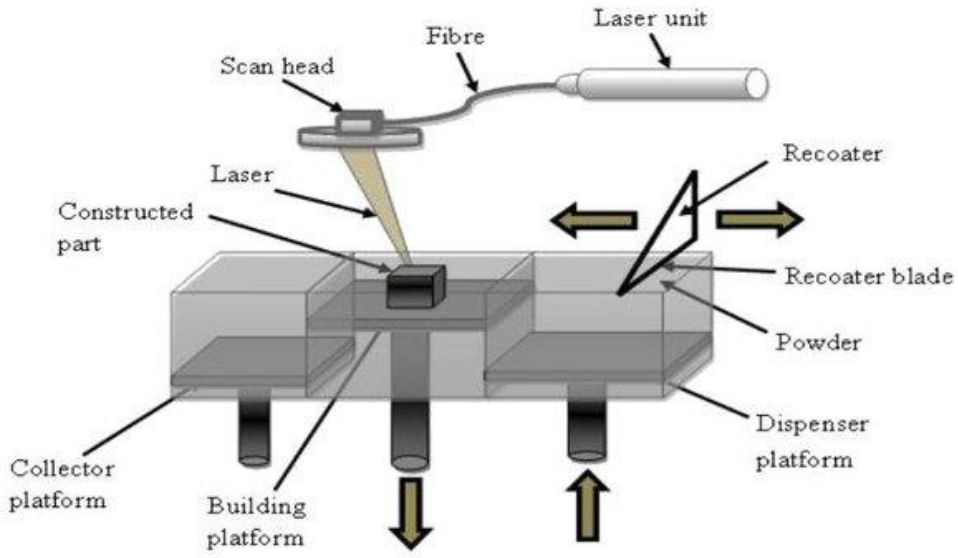

Figure 1.6: SLM build process schematic identifying mechanism of powder recoating and laser scanning of a part [62][7].

SLM's capability to form highly complex, functional metal products has resulted in an increased popularity for this manufacturing process. This growing interest and the need to classify and improve the technology has resulted in a significant amount of research effort aimed at characterising the physical phenomena of the SLM process.

Variation in processing parameters of SLM have a huge impact upon the final product performance. Rehme and Emmelmann [63] state there are over 130 processing parameters that are suggested to influence the quality of a part produced via SLM in terms of density, material properties and surface finish. Approximately 13 of these parameters are critical to achieving fully dense parts with few defects, good surface finish, and good mechanical properties. Without

[7] Republished from MATEC Web of Conferences, "Investigation into Effects of Scanning Speed on in Vitro Biocompatibility of Selective Laser Melted 316L Stainless Steel Parts", Y. Shang, Y. Yuan, Y. Zhang, D. Li, Y. li, (2017); use permitted under the Creative Commons Attribution License CC BY 4.0

careful consideration of the energy input and consolidation pathways, the part density and mechanical properties can be greatly affected. The parameters associated with SLM can be broadly categorized into two sections: processing parameters and material parameters.

Processing parameters include all those associated with the build of parts in the machine and the process environment. This includes energy imparted to the powder bed, the layout of scan patterns and laser pathways, and build chamber atmosphere. Material parameters are those relating to the powder feedstock including powder morphology, size and distribution, as well as powder material properties.

Different properties of SLM produced parts can be investigated to identify suitable process operating parameters. One of the most important attributes of manufactured parts is density, as this is a measure of porosity and defects within the SLM manufactured part [63]. Porosity defects form through a number of mechanisms that relate to incorrect processing parameters [64, 65]. Lack of fusion (LOF) porosity is a form of defect that typically results from insufficient energy input during SLM. A new layer of powder may not be fully melted with low energy or may not form a melt pool overlap with neighbouring laser scan paths. This results in large, irregular defects, within which partially melted powder particles can often be observed [66].

One mechanism in forming LOF pores is the phenomena of balling. Balling is a complex process that occurs due to thermal and surface tension gradients in the melt pool [67]. This results in molten metal forming into solidified spheres larger than the powder size. Gu and Shen [68] identified two different balling mechanisms in SLM. Low laser power produced large, coarsened metal particles, developed by reduced liquid formation and capillary forces. Of lesser concern was the formation of laser induced melt splash balls. These were formed by capillary instability in the melt and formed spheres on the surface no greater than those of the powder feedstock. Shen et al. [69] also highlighted that high energy input could cause melt pool instability, resulting in discontinuous track formation, due to large melt pools of low viscosity. The formation of large spheres through the

balling process is detrimental to the quality of parts as it introduces inconsistencies into the consolidated material along laser paths and can result in LOF pores forming. The large ball particles produced also promote porosity by interrupting the recoating of consecutive layers of powder. These studies have determined balling can be eliminated through increasing the energy input to the melt pool.

Further porosity defects can be formed when SLM energy input is too high. A form of pore that can form under these conditions is gas entrapment porosity [64, 70]. With higher energy input a larger, deeper, melt pool can form under the laser. This can become very unstable due to the rate of temperature change, gas forces and other physical effects. Gas bubbles can become trapped within the unstable pool as it solidifies, creating a defect. This can also be referred to as keyhole porosity where the higher laser power forms a pit in the melt pool, further increasing the laser energy absorbed due to internal reflection. The subsequent collaps of this pit results in trapped gas pockets [71, 72]. Gas entrapment pores are identified by their more regular spherical shape. A balance needs to be achieved between low energy input causing LOF defects, and gas entrapment from melt instability at high energy densities [73].

The impact of build parameters on part density and porosity has been the focus of many investigations into SLM [74]. Regression analysis of process parameters and their effect on part density are often used to establish processing parameters empirically [75-77]. Other studies by Childs and Hauser [78] and Wright et al. [79] target the optimisation of processing conditions in single track formation through controlling melt pool stability to achieve high density products. Surface roughness and material hardness of fabricated parts are also properties that researchers have focused on for optimising SLM parameters [74, 80-82]. These are also easily measurable with suitable equipment and can identify the effect different parameters have on part characteristics. Henceforth in this review these variables will be referred to as ***part quality***. High quality parts are defined as having high density (>98%), low surface roughness, and hardness comparable to that of billet material.

For parameter development, key process parameters are often combined into the energy density factor, *E* in J/mm^3. This represents the amount of energy imparted to a volume of new powder and is calculated by Equation 1.4. This factor is a representation of the energy input for the melting/consolidation process which impacts the densification of parts and microstructural development [83]. Energy density is useful for parameter development and optimisation, enabling comparison between different parameter sets and the resultant properties of the SLM manufacture material [77, 84]

$$E = \frac{P}{v \cdot h \cdot t} \qquad \textbf{Equation 1.4}$$

E – energy density (J/mm^3)
P – laser power (W)
v – laser scanning speed (mm/s)
h – hatch distance or spacing between laser scans (mm)
t – layer thickness (mm)

The use of the energy density equation in selecting/optimising parameters is somewhat limited. A range of different parameters can be selected to give the same value of energy density. Investigation has shown that the properties of consolidated material can vary greatly despite identical energy density calculated using Equation 1.4 [85]. Material parameters such as powder morphology also have a significant influence on consolidation and are not accounted for within energy density. When comparing different SLM systems the energy density factor can be used for approximate comparisons however different SLM systems operate with different hardware such as pulsed vs. continuous lasers. The large number of parameters that have an influence on material consolidation make it difficult to accurately compare different systems without extensive characterisation relating the parameters used in each process.

In addition to energy density parameters, processing features such as the laser scan pattern can have an impact on SLM part quality. Figure 1.7 presents a typical laser scan pattern for SLM processing, comprising contour or border scans around the periphery of the part and an internal hatch pattern of scan lines. These parameters are set to ensure overlap of the melt pool under the laser and consolidated material of adjacent paths to produce fully dense, high quality parts.

To improve the homogeneity of the parts and eliminate any directional effects that may occur due to the scan pattern. a rotation of the scan pattern is normally performed. Thijs et al. [86] reported an increase in density of parts fabricated with a layer rotating scan strategy compared to unidirectional scanning. A more equiaxed grain structure was also observed with reduced directional effects.

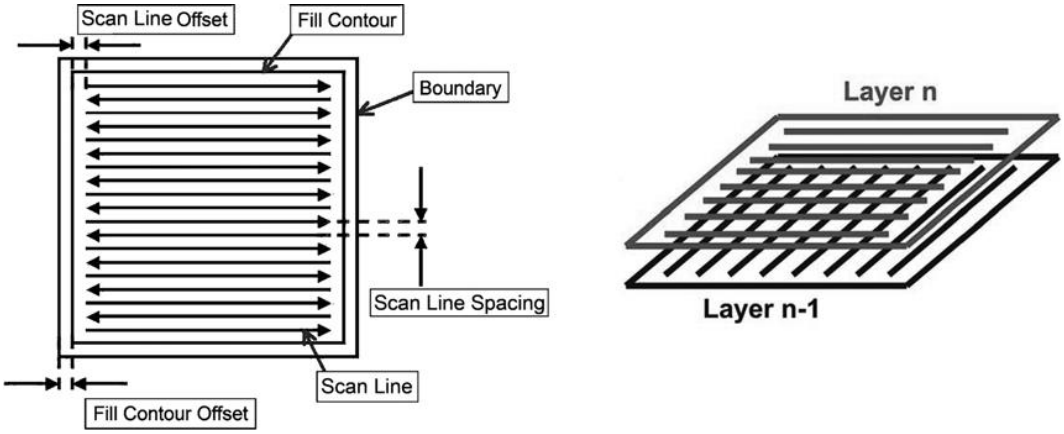

Figure 1.7: Example of a SLM scan pattern and 90° rotation of the scan pattern in sequential layers of the process [87][8].

To achieve optimal processing conditions, the build chamber in the SLM process is purged with argon to reduce the oxygen concentration below 0.2%. This eliminates flammability issues with powdered materials and prevents oxidation of the metal at the high processing temperatures. An inert gas flow across the build platform is maintained to remove bi-products of the laser processing which include vaporised powder (condensate). This helps maintain a clean atmosphere for the laser which is important for beam quality. The condensate is filtered from the argon and recycled in a continuous loop. Studies by Dadbakhsh, et al. [87] and Ferrar et al. [88] have identified that this gas flow can have an effect on the quality of parts produced by SLM. Dadbakhsh, et al. [87] identified that part layout and cooling rates created by the gas flow influenced the mechanical properties of stainless steel parts. Ferrar, et al. [88] determined that gas flow uniformity had an effect on the porosity of parts. With uneven gas flow across the powder bed the porosity was found to vary and resulted in difficulty creating repeatable results,

[8] Republished with permission of Emerald Publishing Limited, from Rapid Prototyping Journal, "Effect of selective laser melting layout on the quality of stainless steel parts", S. Dadbakhsh, L. Hao, N. Sewell, Copyright © 2012, Emerald Group Publishing Limited (2021); permission conveyed through Copyright Clearance Centre, Inc.

both within a single build at different part positions and between different builds. Design improvements to the gas delivery system were implemented that reduced the observed variation.

Thermal modelling has been especially helpful in the development of SLM. Das and Chung [89] developed an early 1D model in treating the rapid melting and solidification under laser processing as a Stefan problem. This enabled the determination of the melt and solidification times along with melt penetration with varying scan speed, spot size, and laser spot profile. This was a highly simplified model and has since been improved upon. Tolochko et al. [90] produced an in-depth study on the theory behind laser processing which identifies the ability of laser processing to fabricate fully dense parts through the full melting of metal powders.

Although analytical models have been developed these involve assumptions and simplifications of boundary conditions. Numerical methods such as FEA have proven capable of simulating the laser melting process despite the systems' complexity. Simulation of the laser power and scan speed by Chen and Zhang [91] gave an improved understanding of the melt pool development and penetration into the powder bed. A number of other studies have been performed using various techniques to develop the understanding of the SLM process and improve the technology and its application [92-94].

SLM processing maps have been produced for various materials however given the large number of variables that have an impact on the process these are not standardised. These maps can identify general effects that process parameters have on material properties and indicate the range within which parameters can fail to produce high quality products. Gong et al. [95] developed the process map in Figure 1.8 for titanium alloy Ti64 based on parameters in the volumetric energy density formula. Laser power and scanning speed were varied to identify different "zones" of behaviour with respect to part density. Zone I is classified as producing fully dense parts. Features of over-melting and incomplete melting are represented by Zone II and Zone III respectively.

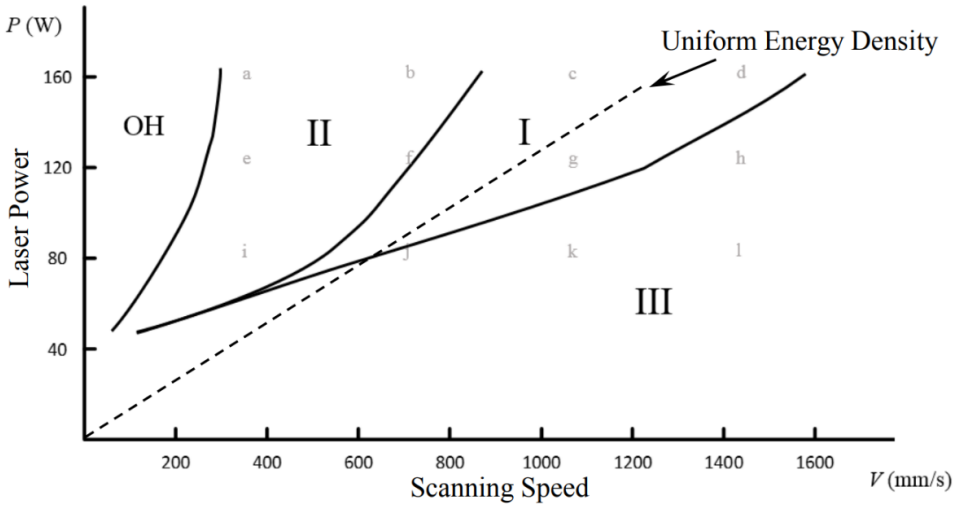

Figure 1.8: Process map for SLM of Raymore Ti64 powder [95][9].

Song, et al. [81] also optimised parameters for Ti64 based on the investigation of forming single tracks on Ti64 plate. A laser power of 110 W and speed of 400 mm/s were identified as optimal for producing the best quality parts. When compared to the work of Gong, et al. [95] in Figure 1.8, these parameters are identified as over melted (Zone 2).

This highlights the fact that there are additional factors influencing part quality within these studies leading to considerable variability between optimised parameters used by researchers. Further, using the energy density factor for optimisation does not account for additional process variables and is somewhat limited, as claimed by Lu, et al. [85]. Process maps may only be applicable to the study within which they are performed as the number of other unreported variables that have an influence on part quality is high. Other investigations that do not reproduce the same conditions on similar equipment will have difficulty reproducing results. This is made obvious in literature by the significant range of energy density values reported for SLM processing of a material. For SLM of Ti64, energy density values between 40 J/mm^3 and 120 J/mm^3 [74, 96-98] are reported as optimum. While the large number of influential process parameters add complexity to optimisation of SLM processes, trends such as those identified in Figure 1.8 by Gong, et al. [95] should still apply.

[9] Reproduced from Solid Freeform Fabrication Symposium Proceedings, "The effects of processing parameters on defect regularity in Ti-6Al-4V parts fabricated by selective laser melting and electron beam melting", H. Gong, K. Rafi, T. Starr, B. Stucker (2013); with permission within Solid Freeform Fabrication (SFF) Symposium guidelines, https://www.sffsymposium.org/

When considering commercialisation of SLM it is important that the parameters used follow the most efficient method. Part turnover is one of the greatest requirements in industry, alongside part quality. As such the time to manufacture should be minimised. Sun et al. [99] identified SLM parameters of 80 W laser power and 200 mm/s scanning speed as optimal for Ti64. While providing insight into the mechanisms behind SLM, the speed of this process is fairly slow and does not prove to be commercially viable. Vrancken et al. [100] identify a more commercially applicable set of process parameters with laser power of 250 W and speed of 1600 mm/s. Depending on other parameters, these parameters would reduce laser time by a factor of eight. This is especially significant when building larger volume components with fabrication times greater than 48 hours.

The temperature gradients and rapid phase changes in SLM cause some unique challenges to the process. Cooling rates in laser processing range have been identified as being in the range of 1-40 K/μs [101, 102]. These cooling rates give rise to some unique microstructures. A significant challenge that is also introduced by this rapid cooling is the residual stress induced in the built components. These stresses are caused by the rapid solidification and associated solidification shrinkage as the material transitions from liquid to solid. The largest stress has been identified as occurring at the top surface of the parts [74]. These thermal stresses can cause parts to break away from the substrate plate or crack if the residual stress becomes great enough. Large overhangs also demonstrate a tendency to curl upwards due to these thermal stresses.

Shiomi et al. [103] experimented with chrome molybdenum steel to determine an effective means of reducing residual stresses. Build chamber heating, layer re-scanning, and post fabrication heat treatment all served to reduce residual stress in the products by greater than 40%. In the case of heat treatment, the reduction in residual stress was up to 70%.

Modelling of track formation and stress development has also led to identification of stress reducing parameters. Matsumoto et al. [104] used FEA to determine that scanning strategy and pattern could be used to greatly reduce the internal stress. They identified the stress and deflection is a function of scan vector length. By

reducing scan vector lengths and using a random checkerboard pattern the residual stress and likelihood of parts failing due to stress cracking in the fabrication process could be minimised.

1.3.3.2 SLM Powder Properties

SLM has specific requirements with respect to the quality of metal powder that can be processed successfully to produce high quality parts. The morphology and size of the powder can have a number of effects on the recoating and consolidation. Spherical metal powders are required for SLM due to the flowability and attainable packing density. Recoating of the powder during SLM processing requires a thin layer, between 20 µm and 100 µm, to be deposited. This is done by sweeping new powder over the build platform after the platform has been lowered to allow a thin layer of new powder to be left behind. Non-spherical powder is more prone to clumping and results in uneven recoating which in turn can lead to defects in the build and makes reproducibility of parts very difficult. Suggestions have been made that powder of more irregular shape can be used in the SLM process if greater layer thicknesses are used as this reduces the variation in the powder layer [105].

Powders used in SLM are not of uniform size and often follow a Gaussian distribution due to manufacturing conditions and sieving capabilities. Bourell et al. [106] identified that powder distribution affected the part mechanical properties. Larger proportions of smaller particles resulted in better melt pool development and greater part densities with lower energy input. Larger mean particle distributions were found to develop greater elongation properties while higher strength parts were obtained from smaller powders. It is proposed that to achieve high quality parts the powder distribution should be smaller than the layer thickness and contain a high proportion of small particles.

The packing density of the powder is another important property that can improve part quality. The density of the powder bed in SLM has been identified to affect the final part density by Liu et al. [107]. A greater bed density is capable of better laser energy absorption and results in a more stable melt pool. For SLM, the packing density is estimated as being equivalent to the loose poured density

(apparent density) of the powder. Measurement and simulation for the packing density of spherical particles in a have determined the maximum apparent density of SLM metals powders is approximately 60% [108, 109].

1.3.3.3 SLM Materials - Titanium Properties

Market development of SLM has seen the expansion of the technology into a number of materials. Current reported materials that have progressed to commercial use through additive manufacturing are listed in Table 1.8.

Table 1.8: Selected materials commonly used in SLM for commercial purposes.

Titanium	Aluminium	Tool Steels	Super alloys	Stainless steel	Refractory
Ti64	Al-Si-Mg	H13	IN625	316/316L	MoRe
ELI Ti	6061	Cermets	IN718	420	Ta-W
CP TI			Stellite	347	CoCr
γ-TiAl				PH 17-4	Alumina

One of the most investigated alloys for additive manufacturing is titanium alloy Ti64 due to the advantageous economics of producing net shape, complex geometry, for batches of low production volume parts.

The nature of rapid melting and solidification in SLM results in the development of microstructures that are very process specific. Thijs, et al. [86] has extensively classified the microstructure that develops from SLM processing of Ti64. The rapid cooling rates develop a fully martensitic alpha prime structure. The grain structure of the material is very dependent on processing, exhibiting features that align within the material. Figure 1.9 presents the typical microstructure of SLM fabricated Ti64 as characterised by Rafi et al. [110]. The overall structure consists of fine alpha prime martensite lathes. These are arranged in colonies/prior-beta grains, displaying alignment specific to the build direction. Long columnar grains in vertical cross sections, (a) and (b), extend in the build direction. The horizontal section in plane with the build layers, (c) and (d), presents an equiaxed grain appearance. It has been noted that the equiaxed grains are approximately the size of the laser spot (70-100 μm) [100]

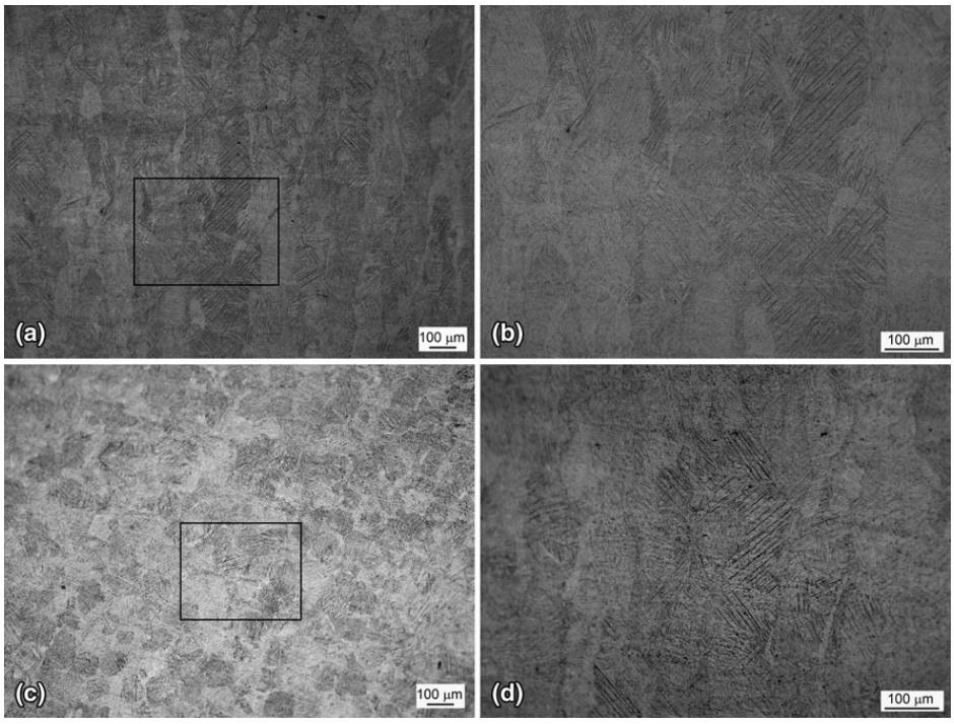

Figure 1.9: Microstructure of Ti64 fabricated by SLM. (a,b) Vertical section showing columnar grains extending in the build direction. (c,d) horizontal section in plan with build layers showing equiaxed cross section of columnar grains. [110][10].

This grain structure is developed due to the directional solidification that takes place as the laser processes consecutive layers. As a new layer is added, the previous layer is also partially melted. A single point in the material may experience remelting and subsequent directional solidification a number of times as further layers are added [111]. This process allows the growth of the columnar grains. Solidification occurs from the bottom of the melt pool aided by pre-existing grain boundaries. This causes these grains to elongate in the build direction.

Murr et al. [112] classified the anisotropic nature of Ti64 parts fabricated through SLM. The fully martensitic structure develops high strength material however this is at the expense of ductility. The nature of the microstructure and processing was seen to develop directional effects in the mechanical properties. Table 1.9 lists some properties observed, showing these anisotropic properties for Ti64 products fabricated at different orientations [96, 110]. Cecchel et al. [113] also investigated

[10] Reprinted by permission from Springer Nature: Journal of Materials Engineering and Performance, "Microstructures and Mechanical Properties of Ti6Al4V Parts Fabricated by Selective Laser Melting and Electron Beam Melting", H.K. Rafi, N.V. Karthik, H. Gong, T.L. Starr, B.E. Stucker, Copyright © 2013, ASM International (2013); permission conveyed through Copyright Clearance Centre, Inc.

these anisotropic effects of microstructure on mechanical properties. In the direction of columnar grains (vertical) the as-built strength properties were marginally higher than in the horizontal direction, in contrast to those of Table 1.9. This can be explained due to the solid-state transformation that takes place as Ti64 cools. The resultant phase and fine lamella structure of the material forms within the columnar grains in coordination with the grain crystallographic arraignment, which is not necessarily dependent on the overall columnar appearance. Thijs, et al. [86] determined that aligning the laser scanning direction throughout a part did result in preferential alignment within columnar grains and as such anisotropic properties were observed. The variation in anisotropic properties presented through literature highlights the influence individual processing conditions have on SLM manufactured material.

Table 1.9: Orientation effects on mechanical properties of SLM Ti64.

Orientation	0.2% Yield Stress (MPa)	Ultimate Tensile Stress (MPa)	Young's Modulus (GPa)	Elongation (%)	Ref.
Vertical	1143	1219	-	4.9	[110]
Horizontal	1195	1269	-	5.0	[110]
Vertical	978	1143	115	11.8	[96]
Horizontal	1075	1199	113	7.6	[96]

1.3.3.4 SLM Titanium Heat Treatments

Heat treatments are commonly performed on Ti64 to modify various properties through altering the microstructure. The condition of the material prior to heat treatment influences the resultant properties as any changes are developed from the initial microstructure [9]. SLM Ti64 parts have a fine martensitic microstructure with some anisotropic features as described previously and presented in Figure 1.9. The effect of heat treatments on this material have been studied to identify differences compared to heat treating Ti64 produced through traditional manufacturing methods.

Stress relieving treatments are seen as important to reduce residual stress and distortion that is a characteristic of the SLM process. These treatments are designed to minimise the transformation of the original fine martensite lamella

and are typically performed around 600°C to 700°C for a few hours [1, 9]. Kruth, et al. [74] noted in a review that hardness (369 HV) and toughness of SLM printed Ti64 were not altered after stress relief treatment at 595°C for 3 hours. In a further investigated treatment of 730°C for 2 hours, toughness decreased slightly, and hardness was increased to 386 HV. Eshawish et al. [114] noted that the martensitic structure of as-built SLM printed Ti64 was maintained after treatment at 702°C for 2 hours, resulting in a hardness of 408 HV.

Annealing treatments on SLM Ti64 parts are performed at temperatures above that of stress relieving to transform the alpha prime martensitic structure to an alpha+beta structure. Sub beta-transus annealing (below approx. 980°C for Ti64 [1]) does not change the lath colony (prior-beta grain) size but coarsens the lathes within them as they transform from martensite to alpha phase, interspaced by beta phase [115]. The coarsening of the lathes of alpha and beta is dependent on the duration the material is held at elevated temperature [100, 116]. The columnar colonies in the build direction, with equiaxed cross section are preserved [100]. Mechanical properties developed in sub-beta annealed Ti64 are typically reduced yield and ultimate tensile strengths (UTS), with improved elongation to fracture. Cecchel, et al. [113] investigated the directional properties of SLM produced Ti64, annealed at 800°C for 4 hours. Differences were identified, with the vertical orientation having increased tensile strength and elongation compared to horizontal samples.

Heat treating above the beta-transus transforms the columnar martensite lath colonies completely to beta phase at this elevated temperature. Again, the duration of the heat treatment above the beta-transus will cause growth/coarsening of these already large columnar beta grains. Different cooling rates for this treatment will alter the room temperature microstructure. Rapid quenching at a cooling rate greater than martensite critical cooling rate (410 K/s) will again result in a martensitic structure forming [117, 118]. Slower controlled cooling will develop alpha+beta phases. These are typically in a coarser lathe structure however more globular alpha phase grains have been observed [100, 113, 116]. An alpha phase boundary can also be formed around prior-beta grains

[100]. The yield strength and UTS of beta annealed material is further reduced compared to sub-beta annealing with little change in elongation to fracture.

Through these heat treatments and combinations of them, a range of different properties can be developed. A feature that remains is that of aligned columnar prior-beta grains. Through heat treatment alone it is difficult to eliminate this feature of SLM produced Ti64, and often coarsening of these anisotropic features can occur to the detriment of material properties. Other options exist alongside heat treatments that can alter the materials performance, including particulate inclusion and interstitial strengthening, as discussed previously in this chapter. Heat treatments can be applied in conjunction with these modifications and may result in new options for adjusting the materials microstructure and properties.

1.4 In-Situ Modification of Titanium using Oxygen and Boron

The traditional manufacturing processes of producing TMC's reinforced with in-situ TiB whiskers include powder compaction and sintering methods, extrusion and some casting capability as outlined by Tjong and Ma [15]. All of these processes are limited in terms of product shape with post processing required to generate more complex components. The nature of titanium makes machining difficult with the reinforcement adding to these difficulties. This makes this material more expensive to process and therefore limits application in fields where it is highly suited. As a result, net shape fabrication of these composites through additive manufacturing has received attention.

DED processes with powder feedstock have been used to produce titanium composites containing TiC particles and TiB whisker reinforcement. Banerjee et al. [119] successfully synthesised TiB whisker reinforcement in-situ within a Ti64 matrix through a powder fed DED process using a laser as the energy source. Elemental boron powder was included within the feed material and reacted with titanium during solidification of the melt. A homogeneous distribution of TiB whiskers was produced with lengths between 1-5 µm. Characterisation of the microstructure was performed through SEM imaging and TEM. The microstructure of the matrix was found to be refined slightly from that of unreinforced DED fabricated Ti64.

Zhang et al. [120] also investigated the development of Ti64 matrix TiB/TiC composites fabricated through laser and powder DED fabrication. In-situ reactions between the matrix alloy and B_4C reactant powder were induced in the melt. A volume fraction of 25% TiB and TiC reinforcement was produced. TiB existed as whisker-like particulates while TiC formed a granular morphology. Some of the B_4C was identified as unreacted due to reaction products forming at the surface of the added B_4C particles, forming a barrier that prevented a complete reaction from taking place during the rapid solidification and cooling of the material.

Wang et al. [121] also used laser and powder DED for the fabrication of Ti64 with 1.55 wt% and 3.1 wt% boron added. The focus of their work was to establish the tribological properties of the composite in dry sliding pin on disk experiments. The wear rate was reduced through the addition of boron into the material although this was attributed to the increase in hardness of the material rather than any direct effect of the TiB particulates. In unmodified Ti64 wear began as two body abrasion and progressed to three body abrasion and adhesive wear due to the interaction between titanium and the iron counterbody. With boron added, the wear process was dominated by micro-grooving, attributed to three body abrasion between TiB particles pulled from the surface.

Trace boron additions (less than 0.13 wt%) in Ti64, processed using wire fed DED with an arc energy source, have been found to control unfavourable microstructures that are established through the manufacturing process. Grain boundary-alpha and colony-alpha microstructure features were found to be eliminated by the boron addition. Grain refinement of alpha-lathes were also observed. After heat treatment a strength increase of 10% and up to 40% improvement in ductility were achieved for the boron modified alloy [122].

Research by Attar, et al. [77] has seen the application of SLM to the fabrication of TiB in a CP titanium matrix from the reaction of 5 wt% TiB_2. Mechanical milling of initial feedstock was used to initially blend the titanium with TiB_2 resulting in irregular shaped feedstock powder. Fully dense parts were still achieved with fully developed TiB whiskers. Processing parameters of the SLM system were investigated with an energy density of 120 J/mm^3 established as suitable for

processing this material. Compressive mechanical properties developed from this material included hardness of 402 HV, yield strength 1103 MPa and compressive strength 1421 MPa compared to 261 HV, 560 MPa and 1136 MPa in SLM fabricated CP titanium. Refinement of the titanium grains was also observed as a result of the boron addition. Further work by Attar et al. [123] looked at wear performance of SLM manufactured CP titanium with 5 wt% TiB_2 added. An improvement in wear properties was observed in the boron modified material. This presented as reduced delamination which was determined as consistent with the increased hardness and grain refinement.

Minor additions of B_4C up to 1 wt% have been made to Ti64 parts through SLM manufacture by Li et al. [124]. This was found to develop nanoscale TiB whiskers and TiC particulates via in-situ reactions during manufacture. The particulates formed a network like structure with concentrations of particulates forming between lamella grains and contributing to a finer grain structure overall. An increase in hardness and compressive strength were observed as a result of grain refinement and solid solution strengthening. Ultimate compressive true strength in material with 1 wt% B_4C improved by more than 350 MPa, to 1747 MPa.

Along with the boron addition to titanium for modified properties, oxygen content in titanium alloys fabricated through SLM has also received some attention. Quintana and Tong [125] studied changes in tensile properties and fatigue performance of Ti64 with respect to oxygen content (ranging between 0.110 wt% and 0.164 wt%.) The higher oxygen content material had higher yield strength, ultimate tensile strength, and elongation properties after hot isostatic pressing. It also demonstrated a higher fatigue limit. The strengthening effect of low levels of oxygen serves to improve several properties of titanium so may offer a route to tailor the mechanical properties in-situ during AM for specific applications.

1.5 Summary

The current studies performed into SLM of modified titanium alloys provide a foundation for further research in this area. Low percentage additions of boron or oxygen provide different mechanisms for achieving hardness and strength improvements. Current work on AM titanium composites have explored the modification of material properties with these low element additions however comprehensive studies on as-built material and heat treatment effects is limited.

Wear performance is one of the key areas identified as poor in titanium alloys. Through these modified alloys this may be improved however little information on the AM processing routes and resultant tribological properties with low levels of boron and oxygen enhancement exist.

1.6 Objectives

The aim of this work is to develop understanding around the influence of manufacturing parameters on the consolidation of Ti64, modified in-situ with boron and oxygen. Specifically, the effect of process parameters, laser power and scanning speed, will be evaluated with respect to part density, microstructure, and hardness. Compressive properties and wear resistance are also investigated with regards to the additives and the influence they have.

1.6.1 Objective 1:

Analytically compare sample properties using different process parameters to generate processing windows for the in-situ modified material.

An energy density formula is commonly used to combine the effects of different process parameters into one metric of energy input per unit volume. This is often used as a point of comparison between different processing conditions. Different combinations of the same parameters can give the same value of energy density, so comparisons using this formula can demonstrate variation. Comparisons between sample properties and parameters are made through the energy density formula to test its sensitivity and its applicability as a single metric for process comparisons.

1.6.2 Objective 2:

To investigate how processing may influence the distribution and homogeneity of the modified material.

Using a blended powder approach to fabricating Ti64 modified by adding boron and TiO_2 powders may result in segregation of different phases and uneven distribution of the added material. A standard stress relief heat treatment was compared to the as-built material to see how this may result in changes in distribution of the added elements. An annealing treatment was investigated to identify further influence of thermal treatments on the additives. In particular to test higher temperature effects on the precipitation of titanium-boron compounds.

1.6.3 Objective 3:

Characterise the effect the additives have on the mechanical and wear properties of the resultant materials.

Changes in compressive properties were related to change in hardness, modified microstructure, and any different phases or compounds that were formed from the oxygen and boron modifiers. These properties were again related through heat treatments to understand the nature of these materials and determine if they may be applied in practical applications. The reciprocating wear behaviour of these materials was evaluated for the paring against a silicon nitride counterbody in a salt water environment.

1.7 Thesis Structure

This thesis is structured in the following way to explore the results of experiments that investigate the listed objectives.

Chapter 2 – Materials and Methodology

The methodology chapter presents the procedures and experimental design employed in undertaking investigation of processing parameters and material properties of the modified titanium materials. It covers the parameters of material consolidation using SLM and presents details of data collection and analysis.

Chapter 3 – Process Development and Optimisation of SLM

This chapter investigates the effect process parameters have on the consolidation of these in-situ modified titanium materials. Density and hardness are explored along with microstructure investigation relating to the effective incorporation of the boron and oxygen additives. This chapter addresses Objective 1 and also presents results relevant to Objective 2 for the incorporation of additives for modification of Ti64.

Chapter 4 – Microstructure and Mechanical Properties

This chapter presents an investigation into microstructures, compressive properties, and hardness of the modified materials. The influence of heat treatments are also explored in regards to these properties with discussion of the observed trends relating to the manufacturing method and in-situ modification. Objective 2 is explored further in this chapter with regards to heat treatment effects on the material additives. Mechanical properties are also investigated in pursuit of Objective 3.

Chapter 5 – Wear Performance

The wear performance of the modified titanium materials pared against silicon nitride in salt water are investigated in this chapter. Discussions of wear rate and wearing observations are made relating performance with current titanium wear knowledge and other investigated properties in this work. This relates further to Objective 3 in the understanding of properties to determine applicability of these materials.

Chapter 6 – Conclusions and Recommendations

A summary of the conclusions of this work are made regarding the SLM manufacture of in-situ modified Ti64 and subsequent material properties. Recommendations for future work are proposed from the findings of this study to further explore the field of material enhancement through metal additive manufacturing

Chapter 2

Materials and Methodology

2.1 Materials

Ti-6Al-4V (Ti64) gas atomised powder was sourced from FalconTech Co. Ltd., China. The composition of this powder meets the ASTM B348 standard for grade 23 Titanium [11]. Grade 23 is an extra low interstitial (ELI) grade of the most common titanium alloy, Grade 5. In the ELI form, the oxygen content of the Ti64 alloys is more carefully controlled to below 0.13 wt%. The composition of the powder used in this study alongside ASTM specification for grade 23 and grade 5 titanium are included in Table 2.1.

Table 2.1: Ti64 powder composition reported by supplier and compared to ASTM specification.

	Ti	Al	V	O	Fe	N	C	H
FalconTech Ti64 - Batch 150129-002	Bal.	6.05	4.10	0.096	0.03	0.0157	0.007	0.001
Grade 23 Titanium [11]	Bal.	5.5-6.5	3.5-4.5	0.13	0.25	0.03	0.08	0.0125
Grade 5 Titanium [11]	Bal.	5.5-6.75	3.5-4.5	0.2	0.4	0.05	0.08	0.015

The powder batch was kept consistent throughout the study to control composition variability as well as ensuring the powder size and shape were equivalent. The morphology of the powder used was spherical as presented in Figure 2.1 with a specified particle size distribution (D_{10}-D_{90}) of 15-45 µm diameter. In commercial SLM processes, spherical powder with this size distribution is commonly used as it is shown to meet flowability and packing density requirements for SLM printing of layer thicknesses between 30 and 60 µm, resulting in high quality parts [126].

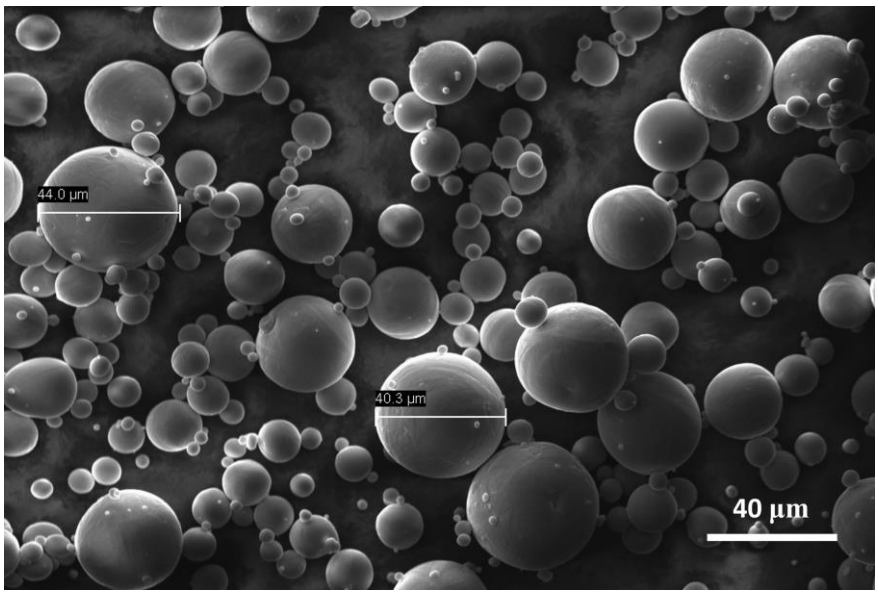

Figure 2.1: SEM image of a sample of gas atomised Ti64 powder used for SLM.

In this study blended powders were used to investigate the effect of small additions of boron and oxygen on the resultant properties of the manufactured material. Amorphous boron powder, 95% pure, was sourced from Sigma Aldrich Inc. with a particle size less than 1 µm. Commercial titanium dioxide (TiO_2) powder used in titanium powder metallurgy and reduction processes was supplied by a local company, Titanox Ltd., particle size was less than 1 µm.

These powders were mixed with Ti64 powder by simply adding measured amounts to an aluminium container that could be sealed. This container was large enough to contain the entire batch (approx. 5kg) of mixed powder for SLM printing, with 20% free space to ensure powder was able to be agitated inside. The Ti64 and boron or TiO_2 powders were blended by rolling/tumbling the container followed by sieving through a 73 µm sieve to prevent any large agglomerations of the added powders. This powder was then tumbled again for approximately 1 hour and sieved once again to ensure homogenous mixing. The blends manufactured are detailed in Table 2.2.

Table 2.2: Powder blends that are investigated in this study.

	Additive			Intended Composition
	Weight %	Atomic %	Mass of additive/kg Ti64	
Ti64	-	-	-	-
Ti64+B	0.27 wt% Boron	0.012 at% Boron	2.7 g/kg (boron)	1.5wt% TiB
Ti64+O	0.21 wt% Oxygen	0.006 at% Oxygen	5.1 g/kg (TiO_2)	0.2wt% O

The material blends were selected to compare the result of low levels of boron addition with that of additional oxygen. Boron is predicted to produce TiB particulates within the titanium alloy and has low solubility while oxygen is soluble as an interstitial. The oxygen addition is comparable to that of boron on a mass basis. From literature an oxygen content above 0.4 wt% can cause significant embrittlement of Ti64 [52-54]. The oxygen addition made in this study was selected to ensure a total oxygen content in the final Ti64 alloy of less than 0.4 wt%, considering the oxygen content present in the supplied Ti64 powder.

2.2 Sample Manufacture and Conditioning

2.2.1 Additive Manufacturing (SLM)

An EOSINT M270 SLM machine with a 200W NdYAG laser was used for producing samples from the powder blends. The fabrication parameters for these materials were investigated to identify a suitable operating point for making high density parts. Key parameters that have an influence on the quality of samples are those in the volumetric energy density equation (Equation 2.1), as discussed in the literature review (Section 6.3.1).

$$E = \frac{P}{v \cdot h \cdot t} \qquad \textbf{Equation 2.1}$$

E – Energy density (J/mm^3)
P – laser power (W)
v – laser scanning speed (mm/s)
h – hatch distance or spacing between laser scans (mm)
t – layer thickness (mm)

The focus of this work was an investigation into the variables of scanning speed (v) and laser power (P). Hatch spacing and layer thickness (h and t) were kept

constant throughout this study. This was in part due to limitations of the SLM machine used for manufacture which did not allow fine adjustment of the layer thickness. A hatch spacing of 0.1 mm and layer thickness of 30 µm were used, which are in line with standard processing parameters of Ti64 on the EOSINT M270 machine. Figure 2.2 presents a set of samples manufactured for this work by SLM.

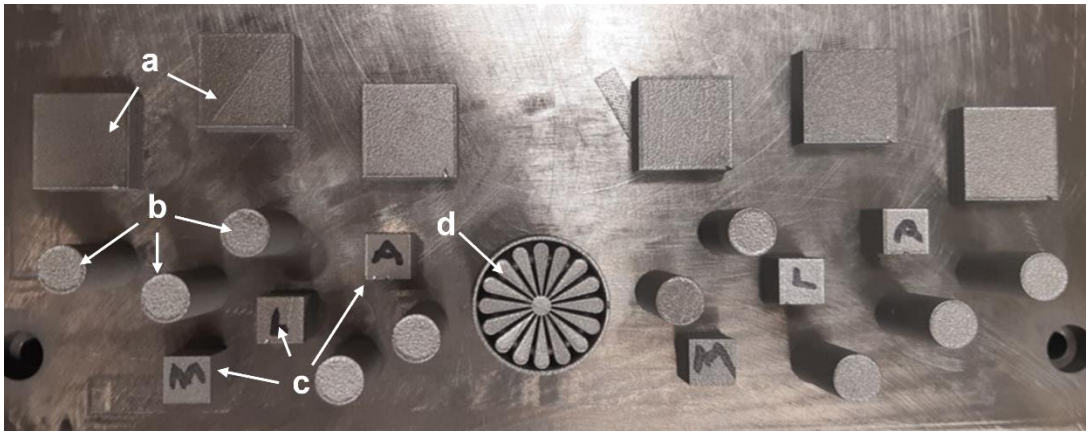

Figure 2.2: Various SLM manufactured samples for this work including wear plates (a), compression cylinders (b), density cubes (c), and segmented disk parameter experiment samples (d).

2.2.2 Heat Treatment

Heat treatments were performed on the different materials to investigate how properties could be influenced with regards to their condition. These treatments were completed using a vacuum furnace capable of maintaining vacuum to less than 1 Pa with the treatments carried out under a small flow of argon (approx. 5 L/min). Two treatments were selected to compare to the material in the as-built condition. These were:

- Stress relief treatment which is common for metal products made by additive manufacturing. This is due to high internal stress developed by the layer-wise deposition and highly localised heat application.
- Annealing treatment at a higher temperature but below the β-transus for Ti64. This was selected to represent another common treatment applied to commercial production of SLM Ti64 parts. This is also a similar thermal treatment cycle to that used in hot isostatic pressing [1].

The parameters of these heat treatments are outlined in Table 2.3 with the furnace temperature log for the different processes presented in Figure 2.3.

Table 2.3: Heat treatment parameters for thermal treatments of SLM samples in this study.

Treatment	Heating Ramp	Atmosphere	Hold Temperature	Hold Time	Cooling
Stress Relief	10 °C/min	Low pressure with Ar flow. approx. 200 Pa approx. 5 L/min Ar	700°C	2 hours	Natural furnace cooling
Annealing			920°C	2 hours	

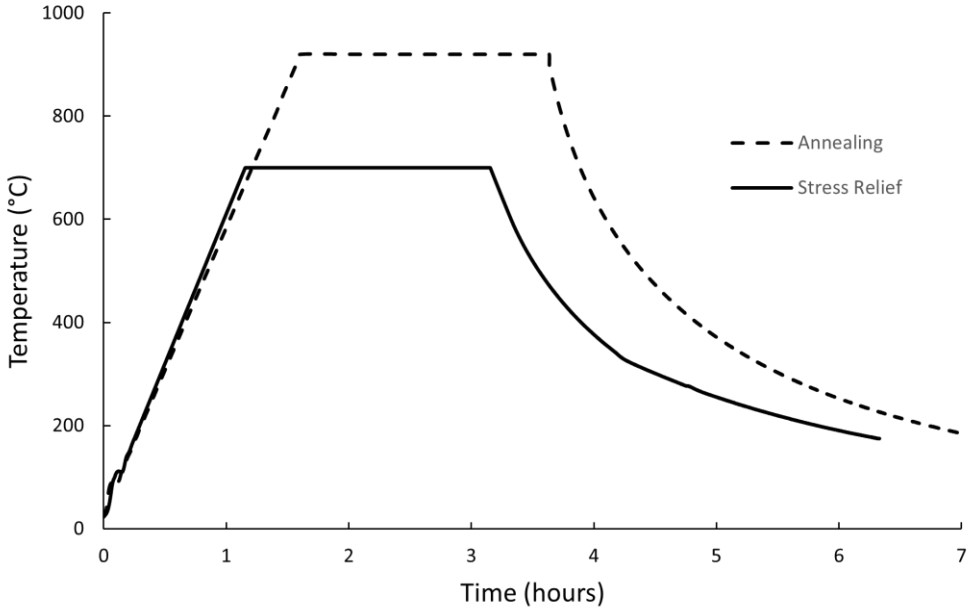

Figure 2.3: Furnace temperature for stress relief and annealing treatments performed on the different modified Ti64 materials (actual furnace logged data).

2.3 Experimental Techniques

2.3.1 Material Investigations

A number of different techniques were used to investigate the properties and behaviour of the materials.

Laser Ablation Inductively Coupled Plasma Mass Spectrometry (LA ICP-MS) was used to measure the composition of the manufactured materials. Oxygen and nitrogen contents were further measured by Inert Gas Fusion (IGF) using a LECO 628 Series machine. The LA ICP-MS system is unable to measure oxygen content accurately for these materials, so IGF was used for the oxygen measurements.

Density of the fabricated parts was measured using Archimedes' Principle. A balance accurate to five decimal places was used for making measurements of dry mass and the buoyancy force in deionised water. Density was calculated using Equation 2.2. Density of water is dependent on temperature, which was monitored during measurements to ensure an accurate density of water was used in calculations. At 25°C water density is 0.99705 kg/m^3.

$$\rho_{part} = \frac{M_{dry} \times \rho_{water}}{M_{dry} - M_{submerged}} \qquad \textbf{Equation 2.2}$$

ρ – Density (kg/m^3)
M – Mass (kg)

2.3.2 Microstructure Techniques

Polishing of samples was performed using a Buhler automatic polishing system. Samples were coarse ground using silicon carbide abrasive papers to a depth of at least 0.2 mm (6 SLM layers = 0.18mm) to expose the bulk material and remove direct surface effects. For hardness measurements, samples were prepared to at least a 9 µm diamond polish. In preparation for etching, samples were polished using a 20% H_2O_2 colloidal silica suspension. Care was taken to ensure the polishing steps did not introduce smearing of the surface which is typical of titanium samples when polishing loads are high or the cutting media is degraded.

Etching was performed using Kroll's reagent, 2% Hydrofluoric acid, 6% Nitric acid, balance water. Highly polished samples were submerged in the etchant for up to 20 seconds to expose the microstructure. Imaging and analysis of the microstructures were performed using both optical (Buehler) and scanning electron (Zeiss) microscopy (SEM).

SEM was performed using a Zeiss EVO MA25 SEM. Secondary electron (SE) and back scatter diffraction (BSD) imaging were used to investigate fine details and microstructures that were not able to be resolved with optical microscopy.

The SEM was also equipped with Energy-dispersive X-ray Spectroscopy (EDS – Oxford Instruments) for performing elemental composition investigations. EDS is limited regarding the quantitative measurement of light elements, boron and oxygen included, as well as having a relatively high minimum detection threshold

of 0.2wt%. EDS was therefore able to report bulk composition of the alloy and for spot analysis of specific features but not for measuring the amount of the additives used. The other techniques (LA ICP-MS and IGF) described previously were used for this purpose.

2.3.3 Phase Identification

Material phases formed through the SLM process and subsequent heat treatments are identified using X-ray diffraction (XRD). Investigations were performed using a Bruker D8 XRD machine with CoK_{α} X-ray source. Samples, 2 mm thick, were cut from printed material and analysed, with XRD patterns produced between 10 and 120 degrees (2θ angle). These XRD patterns were compared with crystallographic reference patterns to identify the phases present.

2.3.4 Mechanical Properties

2.3.4.1 Hardness Measurement

Hardness measurements of polished samples were performed using a Buhler microhardness tester fitted with calibrated optical indent measurement system. Hardness tests were performed in accordance with ASTM E384 [127]. Indents were made using a diamond tipped indenter with a load of 500 gf (4.9 N) and hold time of 5 seconds. Typically, five acceptable indents such as the one shown in Figure 2.4 were recorded from each sample. Vickers hardness results reported throughout this work and will have units of $HV_{0.5}$

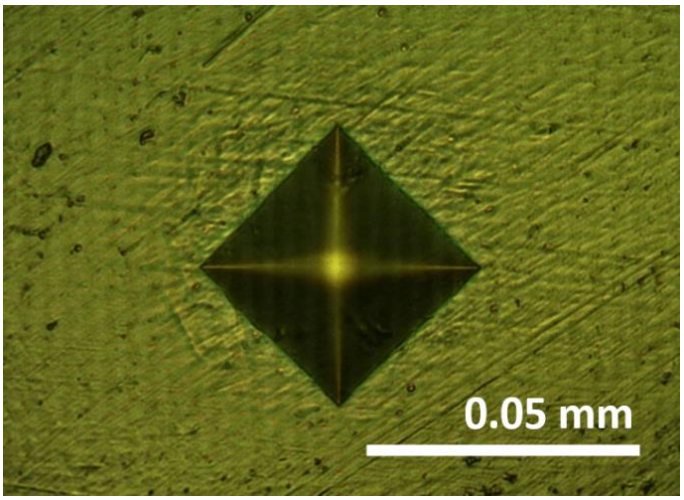

Figure 2.4: Example of diamond Vickers hardness indent in additively manufactured Ti64.

Automation of this process was performed to speed up data collection by installing a CMOS microscope camera (iCube NS1500CU) and imaging each of the indent sites. The microscope images were calibrated using a microscope calibration scale with increments as fine as 0.02 mm. Semi-automatic processing of the hardness indent images were performed using ImageJ with a custom macro [128]. This macro allowed the manual selection and alignment of the vertices of the indentation diamond and automatically calculated the resultant Vickers hardness. The semi-automatic image processing method was initially compared to the original manual hardness measurement method to verify it performed accurately. Both methods produced equivalent results with the semiautomatic method appearing to have reduced error/scatter due to more accurate and repeatable identification of the indent vertices.

2.3.4.2 Compression Testing

Compression testing was performed using an Instron 5985 Universal testing machine equipped with a 250 kN load cell. Cylinders approximately 10 mm in diameter were manufacture for compression testing. These cylinders had the ends machined flat in preparation for testing. The machined length of the samples was approximately 20 mm. Accurate dimensions of each sample were recorded before each test. Compression properties were only tested on samples manufactured in a vertical build orientation on the build plate, where the axis of the cylindrical sample aligned with the build direction (stacking of layers). The surface of the compression samples was in the as-printed state, aside from the machined ends (Figure 2.5).

Figure 2.5: Compression sample with machined ends. Approx. 10 mm diameter, 20 mm long.

Compression tests were performed in accordance with ASTM E9 standard for compression of metallic samples [129]. The compression testing setup was initially tested against aluminium compression samples, as per the mentioned standard, with repeatable results for yield and elastic modulus achieved. A constant cross head speed of 0.06 mm/min was used up to 8% strain for all samples. Yield was reported at 0.2% strain offset from the linear elastic region.

In determining compressive elastic modulus, direct strain measurement was not available. The elastic modulus of compression samples was determined by applying a correction factor that accounted for the stiffness and deflection of the universal testing machine and testing hardware. To achieve this, tensile samples of Ti64 material in the stress relieved condition, equivalent to the stress relieved compression samples, were tested in accordance with ASTM E8/E8M standard [130]. A tensile extensometer (Instron axial clip-on extensometer 2630-100 series, 25 mm gauge length) was used for these tensile samples enabling the strain under tenson to be measured accurately in the elastic region. From this, the elastic modulus of the SLM printed Ti64 material in the stress relieved condition was accurately reported as 119.2 GPa.

Compression testing data for stress relieved Ti64 was then calibrated to match the accurate tensile stiffness. The stress strain curves for tensile and compression calibration are presented in Figure 2.6. This resulted in a calibration value for the combined machine and compression fixture stiffness which could be applied to the raw compression data for the different materials in this study. This calibration process enabled the comparison between the elastic moduli of the materials in as-built and heat treated conditions. It is not expected to be as accurate as extensometers or strain gauge measurement however does standardise the processing of compression data for comparative discussion.

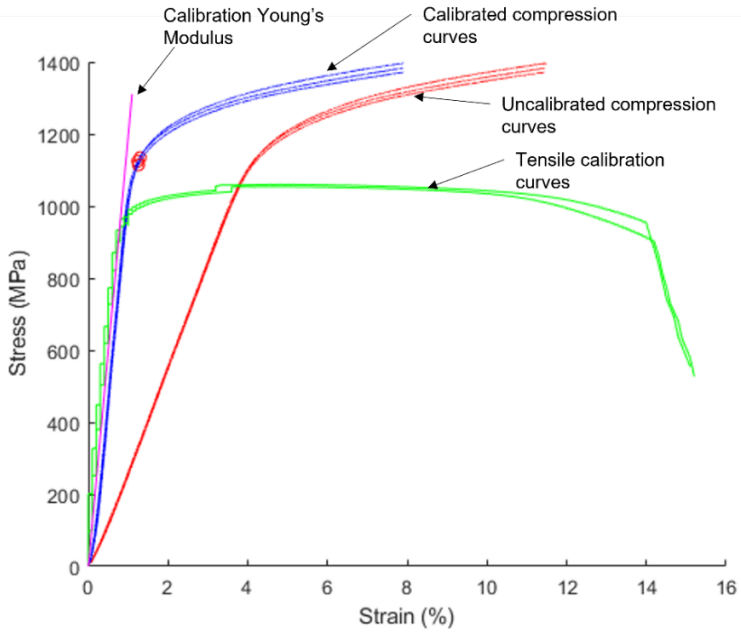

Figure 2.6: Stress-strain curves showing the calibration of compression data using tensile modulus.

For further comparison between the SLM printed Ti64 and modified Ti64 materials a method of deriving a comparative stain energy under compression was developed. This method calculated the area beneath the stress strain curve up to a fixed value of strain (4%) to enable comparison between the different materials. The start of the stress strain curve (<100MPa) was also clipped to remove any variation upon initial loading. Calculating the area beneath the stress strain curve between these limits resulted in a strain energy value (J/mm^3) that could be compared across all Ti64 materials and heat treatments of this study. This comparative strain energy value could be compared with yield strength to determine if the different additives and heat treatments had an influence on plastic deformation behaviour.

2.3.4.3 Reciprocating Wear

Wear performance of the materials was investigated by reciprocating pin on plate testing in saline solution (37g NaCl/L). Plates, 20x20x6 mm^3 were produced by SLM for the different titanium materials in this study. The surface of these plates was ground down by 0.3 mm to remove any surface effects of the manufacturing process. The pin counter-body was a silicon nitride ball bearing (8 mm diameter) applied at a load of 23.79 N. A stroke length of 5 mm, oscillating at a frequency of 5 Hz, was used. Wear track cross-sections were measured using a Bruker Dektak stylus profiler.

2.4 Experimental Design

2.4.1 Manufacturing Optimisation Experimental Method

Initial scoping work investigated the relationship between density and the manufacturing variables of laser power and scanning speed. 8 mm diameter cylinders 10 mm high were fabricated with various combinations of the parameters. Triplicates of each sample were fabricated in a grid pattern on the build platform with positions randomised to reduce systematic error.

A full factorial experiment was designed with six levels of each variable as displayed in Table 2.4. This resulted in a range of energy density levels between 30.30 J/mm^3 and 70.37 J/mm^3.

These parameters were used to produce samples from Ti64 and Ti64+B. Archimedes principle (see section 2.3.1) was used to measure sample densities which were investigated against manufacturing parameters. Comparison of density with respect to sample location during fabrication was also carried out to check manufacturing was not introducing systematic errors.

Table 2.4: Energy density values (J/mm^3) for different levels of power and speed variables in initial scoping experiment.

		Scanning Speed (mm/s)					
Laser power (W)		*900*	*1050*	*1200*	*1350*	*1500*	*1650*
	150	55.56	47.62	41.67	37.04	33.33	30.30
	158	58.52	50.16	43.89	39.01	35.11	31.92
	166	61.48	52.70	46.11	40.99	36.89	33.54
	174	64.44	55.24	48.33	42.96	38.67	35.15
	182	67.41	57.78	50.56	44.94	40.44	36.77
	190	70.37	60.32	52.78	46.91	42.22	38.38
		Energy Density (J/mm^3)					

Further investigation of density was performed with regards to constant energy density. Different combinations of laser power and scanning speed can result in the same energy density. This experiment was performed to help determine the

separate effects of laser power and energy, on density. The parameters for this experiment were a subset of the initial trial in Table 2.4 and are presented in Table 2.5.

Table 2.5: Constant energy density manufacturing parameters. Scanning speed was calculated using the Equation 2.1.

		Energy Density (J/mm³)		
		50	55	60
Laser power (W)	*170*	1133	1030	944
	175	1166	1060	972
	180	1200	1090	1000
	185	1233	1121	1028
		Scanning Speed (mm/s)		

The addition of boron to Ti64 is intended to modify the hardness of the material. To define parameters for further work, the relationship between hardness and processing parameters needed to be investigated. The sample in Figure 2.7 was developed to enable hardness investigation of various parameters. The sample consisted of a 30 mm diameter cylinder split into 16 segments, each connected to the centre and an outer ring. Each segment could be manufactured with different parameters in a single SLM build. The gap between segments minimised the effect any segment could have on neighbouring pieces. This sample fitted polishing equipment and allowed faster sample preparation for microhardness measurement and microstructure investigation. With 16 segments, each sample could contain a two-factor, four level, full factorial experiment. Furthermore, without the need of mounting resin for polishing, the samples could be investigated in the as-built condition and subsequently heat treated and prepared again for investigation of a second condition.

Figure 2.7: Segmented disk for microstructure and hardness investigation.

The range of manufacturing parameters for the segmented disk samples was informed by the preliminary density studies carried out using the parameters in Table 2.4. Following these initial experiments, lower levels of power and scanning speed were explored to investigate consolidation in these regions. Initial trials printed the disk samples with scanning speed of 600 mm/s and laser power greater than 130 W, resulted in those segments failing to build. The energy input appeared to be too great for the material which resulted in those segments deforming and causing damage to the rest of the disk. Following this, those segments were printed with lower laser power to expand the process map. Parameters used to fabricate segmented disks are presented in Table 2.6.

Table 2.6: Table of processing parameters for manufacture of segmented disks for hardness testing. Values are the parameter set energy density in J/mm³.

		Scanning Speed (mm/s)			
Laser Power (W)		*600*	*900*	*1200*	*1500*
	70	38.89	x	x	x
	90	50.00	x	x	x
	110	61.11	x	x	x
	130	72.22	48.15	36.11	28.89
	150	x	55.56	41.67	33.33
	170	x	62.96	47.22	37.78
	190	x	70.37	52.78	42.22
		Energy Density (J/mm³)			

The segmented disks were produced in all materials, Ti64, Ti64+B, and Ti64+O. Density cylinders were also produced with the Table 2.6 parameters to further compare with the original density data from Table 2.4 parameters. Parameter assignment was randomised around the disks along with the printing order. Replicate prints were performed to account for print-to-print variability.

To confirm that boron and oxygen had become incorporated into the material through the SLM process, LA ICP-MS and IGF were used (section 2.3.1). A number of measurements (>5) were taken from different fabricated samples of Ti64, Ti64+B and Ti64+O to confirm the material composition and the proportion of additive that had been incorporated following powder blending and SLM consolidation. A sample of commercial Ti64 plate was used as comparison with the additive manufactured material to act as a reference.

2.4.2 Material Properties Experimental Method

Manufacturing parameters, defined by the results of the Manufacturing Optimisation Method, were used to fabricate all samples for investigation of mechanical properties. These parameters were a laser power of 180 W and scanning speed of 1100 mm/s, with the standard hatch spacing of 0.1 mm and layer thickness of 30 µm.

Samples were manufactured in two builds for each material: Ti64, Ti64+B, and Ti64+O, to account for any build-to-build variability. 8 mm cube samples were also produced for microstructure analysis with regards to build orientation.

Sets of compression samples and cubes were heat treated using the stress relief and annealing procedures outlined in section 2.2.2. Tensile samples were fabricated from Ti64 for calibrating the compression data as detailed in section 2.3.4. Microstructures were investigated, using techniques described in section 2.3.2, for the horizontal and vertical cross sections relative to the sample build direction for all material blends in all heat treatment conditions.

2.4.3 Wear Performance Experimental Method

Following from the mechanical properties and microstructure experiments wear tests were carried out on the as-built and stress relieved samples for the Ti64,

boron, and oxygen modified samples. Commercial Grade 5 titanium plate (Ti64) was also investigated to provide a commercially relevant comparison within the results.

Plate samples were fabricated and heat treated to the same conditions as those of the mechanical properties experiments. Reciprocating pin on disk wear testing was carried out following the procedure described in section 2.3.4.3.

Wear tests were conducted on three plates of material in the same condition at the same time. The plates were randomly aligned in the test to reduce systematic variability with regards to the laser hatch pattern. This replication, random alignment, and non-specific surface grinding depth ensured minimisation of systematic effects in the results.

The simultaneous triplicate tests were performed for 1.5, 3, and 6 hours for each material. Each time interval represents an independent wear track on each plate, tested under the same conditions. The wear track cross sections were measured using profilometry in accordance with ASTM G133 [131]. Images of the wear tracks and the corresponding counterbody were recorded for each time period to identify visual features of wear and how these may change over the duration of testing.

Material loss from the wear track was measured using profilometry across the wear path and reported in mm^2 so is representative of the cross section increase rather than the mass removal. As this is reciprocating wear the profile of the track is not equal along its length. Three wear track profile measurements were taken through the middle of each wear track to reduce measurement error.

2.5 Summary

Figure 2.8 presents the connection between the experimental plan and thesis objectives. The experimental was adaptive and depended on the outcomes of previous investigations as the study progressed. The objectives of this work were completed throughout the different stages of investigation.

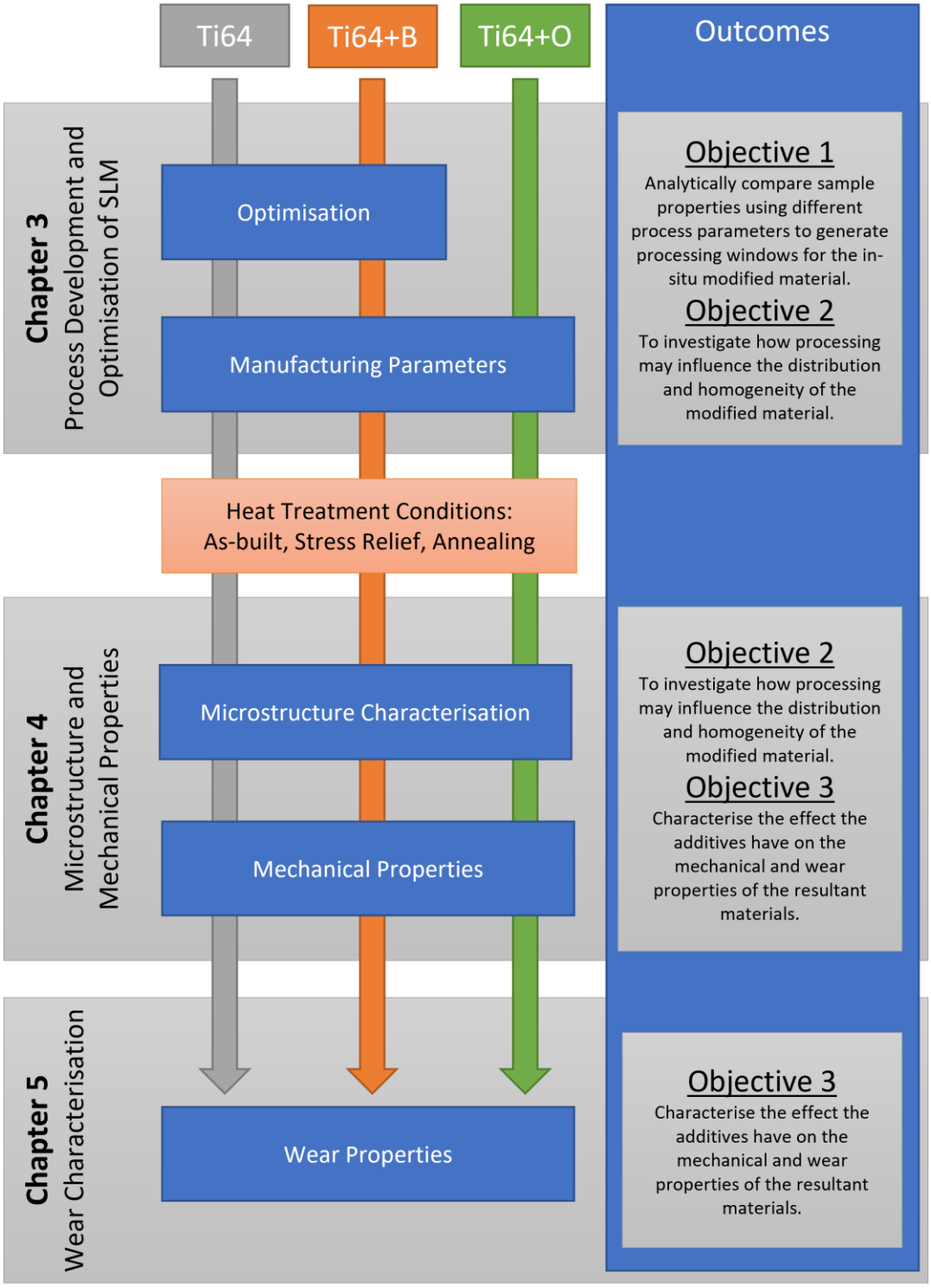

Figure 2.8: Overview of experimental and the connection between different investigations and the thesis objectives.

Chapter 3

Process Development and Optimisation of SLM

3.1 Overview

This chapter presents the optimisation of manufacturing parameters for the modified Ti64 alloys that are the subject of this study. The tuning of these manufacturing parameters is required to produce successful parts which are fully dense.

This optimisation was carried out in two parts. The first part was a preliminary study into the relationship between manufacturing parameters and density for Ti64 and Ti64+B. This information was used in conjunction with statistical analysis (ANOVA) to guide further study of all material blends (including Ti64+B, Ti64+O and Ti64). In the case of the modified Ti64 materials, manufacturing parameters must also incorporate the elemental additives uniformly into the material. Therefore, hardness variation and microstructure appearance were also considered during the second part of parameter optimisation. The resultant compositions of the modified Ti64, manufactured using the selected SLM parameters, are measured to determine the effectiveness of this processing technique for generating these modified alloys

From these combined results a single set of operating parameters was selected that were suitable for all materials. These parameters were carried through to the manufacture of samples for subsequent work in this thesis.

3.2 Effect of Process Parameters on Relative Density

Additive manufacturing for any material using SLM requires the development and optimisation of process parameters to achieve well consolidated parts. This is because the process of laser melting is complex with multi-phase interactions occurring in very short time scales as the powder melts, flows, and solidifies [132]. The material properties, specifically: emissivity, melting point, thermal conductivity, melt viscosity, and powder particle size all influence how the material behaves under laser melting [74]. High density, or the reduction in

porosity, is a primary measure for establishing suitable operating parameters. Without high density, the material properties of the product are compromised by pores that introduce stress concentrations and lead to reduced material performance in additively manufactured parts [65]. Therefore, this study aims to compare the resulting density of manufactured parts to their process parameters.

3.2.1 Correlation between relative density and energy density

An array of initial investigation parameters (laser power and scanning speed) was used to fabricate samples for density investigation (Table 2.4 in section 2.4.1). These parameters were combined into the variable of energy density for comparison with relative part density as outlined in method section 2.4.1. The results of this first investigation are presented in Figure 3.1 for Ti64 and Figure 3.2 for Ti64+B. These identify changes in relative density of the fabricated parts when compared to energy density.

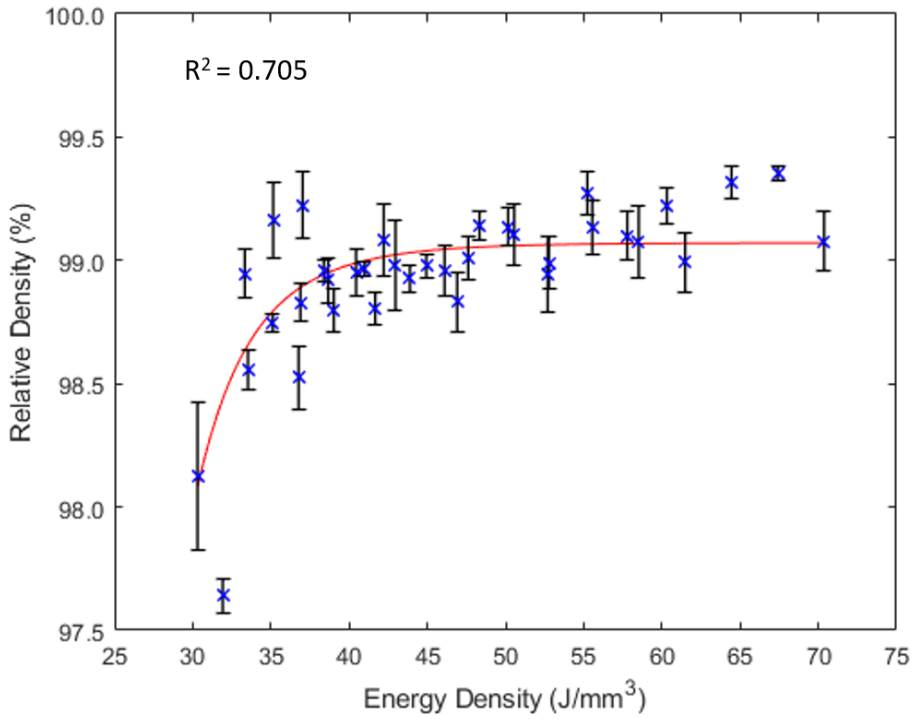

Figure 3.1: Ti64 relative density compared to manufacturing parameter energy density. Error bars present the 95% confidence intervals for the data to show sample variation. A power law curve is fitted to the data with R^2 value indicated.

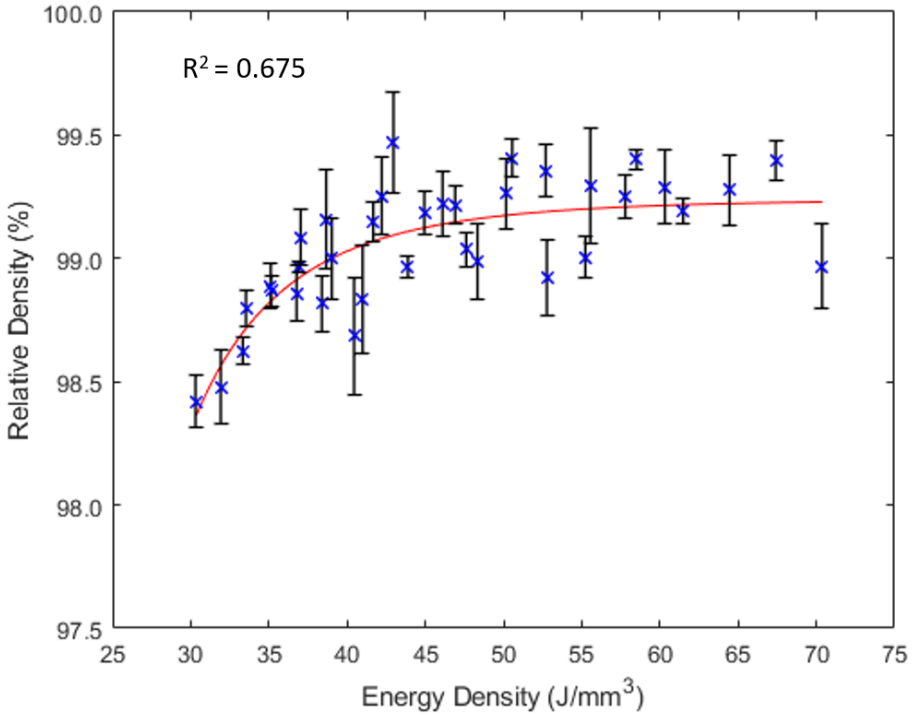

Figure 3.2: Ti64+B relative density compared to manufacturing parameter energy density. Error bars present the 95% confidence intervals for the data to show sample variation. A power law curve is fitted to the data with R^2 value indicated.

At low energy density (below 35 J/mm^3) there is a significant reduction in relative density for both the Ti64 and the boron modified material. There is little difference between the two materials, Ti64 and Ti64+B, regarding density changes with respect to energy density. Both showing a reduction in density at below 35 J/mm^3. Above 40 J/mm^3 relative density plateaus at an average of 99%. There is significant variation about this average 99% density plateau where relative densities between 98.5% and 99.5% are achieved. For both materials it was possible to produce parts with density greater than 99% across a range of different parameters.

The observed trends are consistent with phenomena observed by Thijs, et al. [86] who determined that low energy input was insufficient to fully melt and consolidate the material in each layer, leading to increased porosity. This porosity is known as lack of fusion (LOF) porosity and is a well-established phenomenon in SLM processes [65, 68, 86, 133]. While it is necessary to discuss porosity with regards to manufacturing parameters, this is combined with the examination of material cross sections later in this chapter. The nature of variation between

relative density, energy density, and individual process parameters is first investigated.

Variability in relative density was low for an individual sample condition, as represented by the 95% confidence intervals in Figure 3.1 and 3.2. The difference in relative density between samples manufactured with similar energy densities appears high with no clear explanation. For example, between 50 and 55 J/mm^3 in Figure 3.1 and 3.2, there are different sample conditions where the 95% confidence intervals do not intersect. Meaning these conditions are expected to produce relative density results that are significantly different. Power law curves fitted to the Ti64 and Ti64+B density data in Figure 3.1 and 3.2 have low R^2 values of 0.705 and 0.675 respectively, which identifies this as a poor fit and that presenting the comparison of relative density against the combined variable of energy density may not be the best method of investigating these process parameters.

Energy density is a combined function of the process variables laser power and scanning speed. The variation in part density may therefore be better correlated with the underlying parameters of speed and power. Also, different combinations of power and scanning speed can result in the same energy density value but may not result in the same part density. This is not resolved in Figure 3.1 and 3.2. To separate out the variables and establish a processing window for the materials, contour plots of relative density with respect to scanning speed and laser power were generated.

3.2.2 Relative density as a function of scanning speed and laser power

Contour plots (Figure 3.3 and 3.4) display the interaction between laser power and scanning speed with regards to relative density. These plots only show the average relative density and therefore only represent the mean of each sample condition, not the variation presented by the error bars of Figure 3.1 and 3.2. Both materials show a significant reduction in relative density in the upper left of the plots at low power and high scanning speed. This is a low energy density combination that maps to the values at energy densities less than 35 J/mm^3 in Figure 3.1 and 3.2.

Across the parameter range, excluding the low energy density values, the average relative density is high at around 99% for both materials.

There is little difference between the Ti64 and Ti64+B contour plots. The boron modified material appears to have a larger region where higher density (>99.1%) was achieved however this is only marginally larger than the Ti64 material which presented at least 98.9% over the same region.

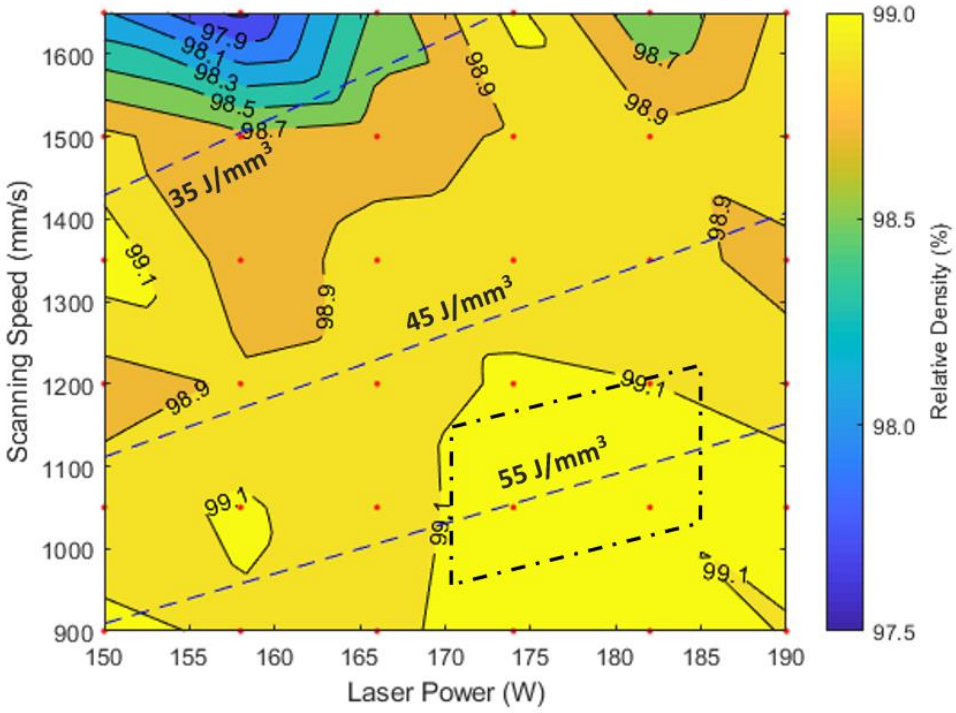

Figure 3.3: Ti64 average density contour plot mapped against laser power and scanning speed. The straight dashed lines represent lines of constant energy density. The region surrounded by dot-dash line in the bottom right is the parameter region investigated further in Figure 3.5.

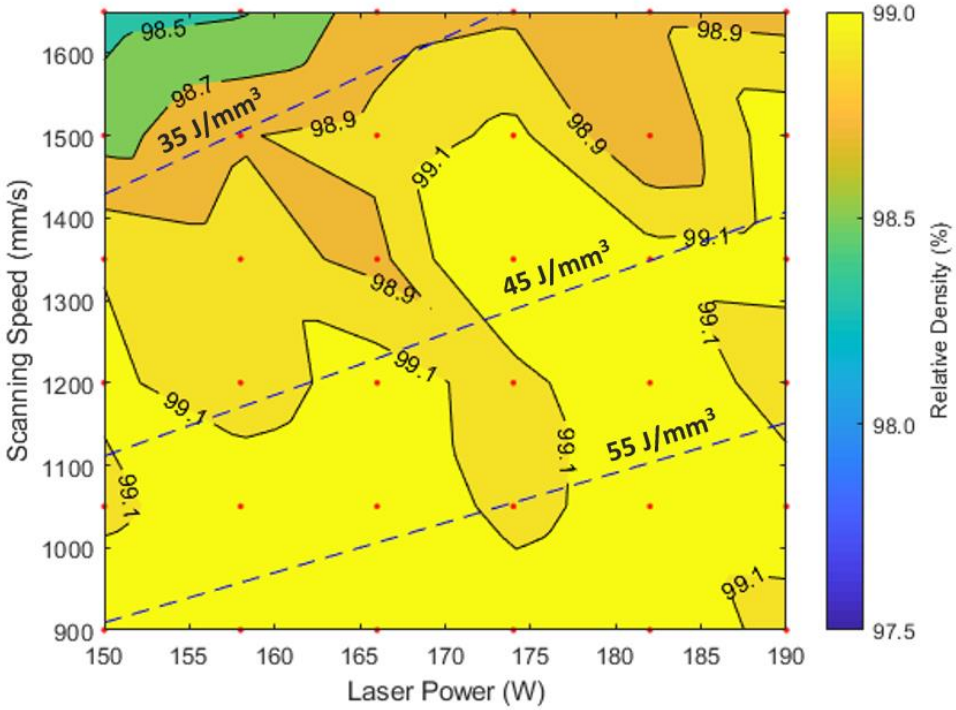

Figure 3.4: Ti64+B average density contour plot mapped against laser power and scanning speed. The straight dashed lines represent lines of constant energy density.

The different combinations of power and speed which result in the same energy density are indicated by the dashed lines overlaid on the contour plots. An observation made from these contour plots is that in regions of higher relative density (>98.9) there is only a small amount of density change along constant energy density lines. It is also apparent that relative density increases with increasing energy density.

Statistical analysis can provide further evidence and quantify the effect different process variables have on the variation in mean density. To explore this, a density experiment was performed with Ti64 samples manufactured using different combinations of power and scanning speed (Table 2.5 in method section 2.4.1), resulting in three levels of constant energy density calculated as per the energy density formula for SLM in section 2.2.1.

The contour plot of relative density from this experiment is presented in Figure 3.5. The range of these variables was selected to be a subset of parameters investigated in Figure 3.3 (indicated by the dot-dash line) and use parameters not tested in this previous experiment which still overlap with this region based on

energy density (parameter details given in Table 2.5 in methods section 2.4.1). A small difference in relative density is expected between the Figure 3.3 region and Figure 3.5 due to the different manufacturing parameters. This difference is relatively small with high relative density above 98.9% achieved in both regions.

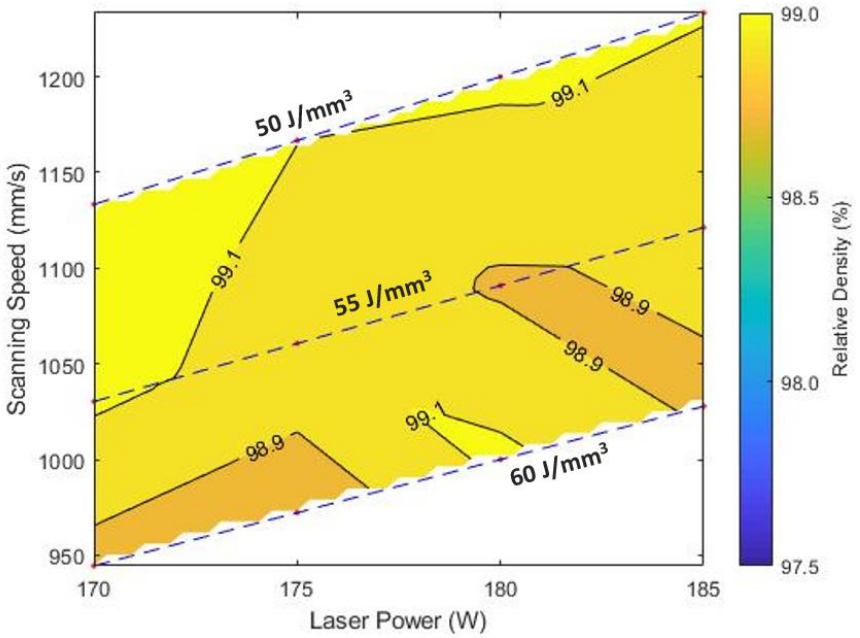

Figure 3.5: Ti64 average relative density with respect to different manufacturing parameters of scanning speed and laser power where these variables combine to give three levels of energy density (50, 55, and 60 J/mm³).

When investigating causes of variance in data and determining statistically significant variables, an analysis of variance (ANOVA) can be performed. Constant levels of energy density were chosen to enable statistical analysis of the relative densities with respect to this variable. Therefore, this analysis has two independent variables (laser power and energy density) with one dependent variable (relative density). An ANOVA for this data is presented in Table 1.

Table 3.1: ANOVA of density data presented in Figure 3.5.

Source of Variation	*SS*	*df*	*MS*	*F*	*P-value*	*F crit*
Energy Density	1.7029	2	0.8514	6.1057	0.0029	3.0648
Laser Power	0.1822	3	0.0607	0.4355	0.728	2.6732
Interaction	1.7294	6	0.2882	2.0669	0.0613	2.168
Within	18.408	132	0.1395			

The ANOVA showed (P-value >0.05) that a change in laser power does not reject the null hypothesis that there is no variation in the mean of relative density for

the tested power levels. However, the energy density parameter does reject this hypothesis (P-value <0.05) suggesting that for changes in energy density there are changes in part density. The interaction effects have a P-value close to 0.05 suggesting that variation could be caused due to some interaction variable.

Scanning speed is a known variable that is dependent on laser power and energy density, as presented through the energy density formula. Therefore, it should have its effect on mean variation included in the interaction variable. Its effect could not be directly measured in an ANOVA as it was not a variable with set levels in this study, a requirement for this statistical test. Other unknown/unmeasured factors may also be included in the interaction category so this effect cannot be attributed to scanning speed alone.

Overall, this ANOVA presents that relative density can be characterised by changes in energy density. This is perhaps not the only contributory factor in relative density as some combined effect between energy density and laser power also appears to have some significance.

3.2.3 Reproducibility of results

The data presented in Figure 5 can also be used to assess reproducibility across a region of different parameters. A difference map was calculated by subtracting the mean densities of Figure 3.5 with the corresponding region of Figure 3.3. This results in a map that represents the variation between manufacturing runs (Figure 3.6).

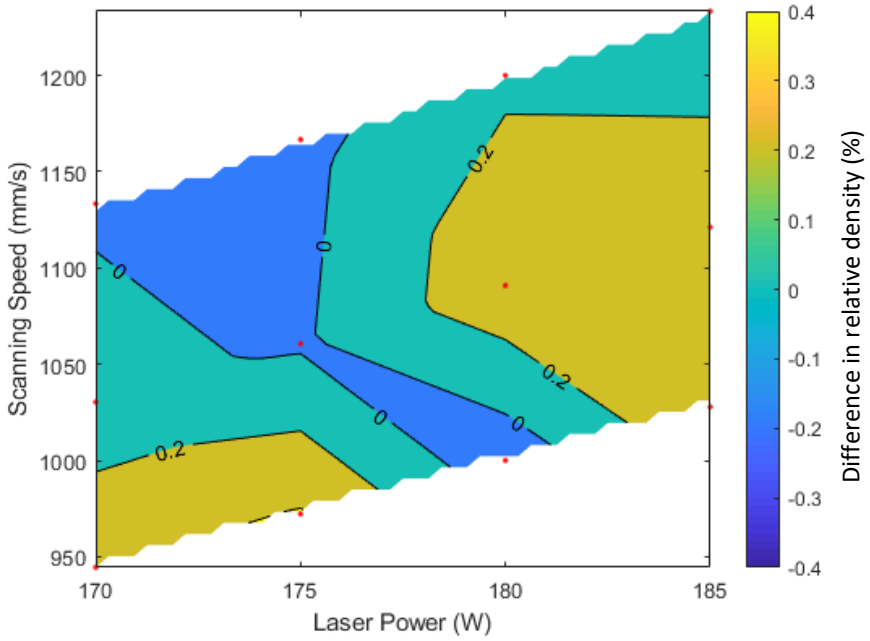

Figure 3.6: Ti64 density difference map for contour plot region that is overlapped by Figure 3.3 and 3.5.

The variation between these maps is a maximum of ±0.2%. This is less than the variation seen between samples in the equivalent energy density range in Figure 3.1 and 3.2. Also, there is no obvious relationship in this variation with respect to the parameters as represented by the irregular contour map indicating low run to run variation.

3.2.4 Variability introduced by part location during manufacture

Variability introduced by part location on the plate was also considered to ensure that the manufacturing process was not introducing systematic error into results. Density samples were manufactured in a grid pattern in the build area corresponding to manufacturing coordinates X and Y. X is in the direction of sweep of the powder recoating and Y is perpendicular to this in plane with the build plate surface. To determine process variability across the build area, density samples were produced in Ti64 with single build parameters of 175 W power and 1060 mm/s speed (energy density 55 J/mm^3). A surface plot relating average part densities to its location in the build area is presented for Ti64 in Figure 3.7.

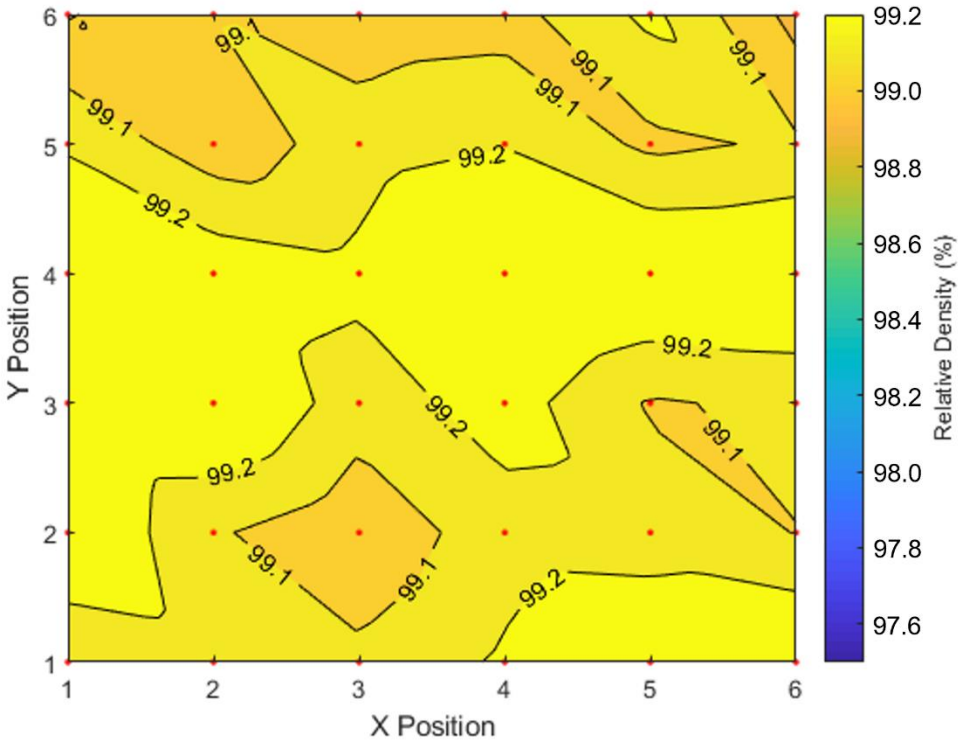

Figure 3.7: Ti64 relative density contour plot with regards to sample build location.

The mean relative density for these parameters is 99.17% and the maximum difference in relative density across the build platform is ±0.21%. This variation is equivalent to the variation seen in the previous reproducibility experiment (Figure 3.6). Therefore, plate build location cannot be concluded to be a significant source of systematic error as this variation is explained by inherent build and sample variations.

In this section, process parameters have been investigated for their effect on relative density. Combining process parameters into the variable of energy density appears to be a suitable method of investigating effects on relative density. While energy density does not account for all variation seen in part density it does provide an effective means of estimating how density may change with selected manufacturing parameters.

Variability of the process has been characterised to investigate sources of systematic error with a small amount of variation between builds and no significant systematic variation inherent to plate location. As variability between plates is low this is unlikely to be a problem in further analyses.

Overall, sources of systematic variation are relatively small compared to gross variation caused by process parameters, however it does reduce the effectiveness of establishing optimum parameters based on relative density alone. In general, high density parts can be produced for Ti64 and Ti64+B using parameters with an energy density greater than 40 J/mm^3. Further investigation of the cause of density variation is required to narrow the process window along with other optimisation criteria, including homogeneous incorporation of the additives.

3.3 Effect of Process Parameters on Microstructures and Porosity

In developing a suitable set of operating parameters for the materials of this study, observation of material cross sections can help in identifying an operating point and causes for density variation. The addition of boron and oxygen into the feedstock powder, and reliance on the SLM process to incorporate them into the resultant material, makes the process parameters an integral part in the blending process. For investigation of blending and incorporation of the additives the third material, Ti64 with added oxygen (Ti64+O), was now introduced to the study alongside Ti64 and Ti64+B. Different parameters may vary how the additives are incorporated into the materials as well as potentially altering how process parameters effect the overall consolidation of the final material. Cross sections of the three material blends (Ti64, Ti64+B, and Ti64+O) were investigated with respect to process parameters in order to identify differences in porosity and microstructural features. This may further inform the selection of suitable operating parameters beyond what can be identified through relative density alone. This section is only a characterisation of differences in microstructural appearance with respect to parameters. Further detailed inspection of microstructures and phase identification is carried out on the optimised material in the following chapter on material properties.

Previously, density was investigated as a measure of porosity and compared to processing parameters (parameter details in Table 2.6 in methods section 2.4.1) to identify a suitable region of operation where high density material was produced. By directly observing porosity in material cross sections and characterising this with respect to known pore forming mechanisms in literature [64-66, 68], a better understanding of the effect process parameters have on

material consolidation can be achieved. This may provide additional insight to help identify suitable operating parameters. Figure 3.8 (Ti64), Figure 3.9 (Ti64+B), and Figure 3.10 (Ti64+O) show etched cross-sections of material with respect to manufacturing parameters. In these images there are clear regions of porosity. The first, labelled ‘1’, is at low energy density where laser power is low and speed is high. A second region of porosity is also identified at high energy density, labelled ‘2’.This is most apparent in Figure 3.8 for Ti64 and Figure 3.10 for Ti64+O.

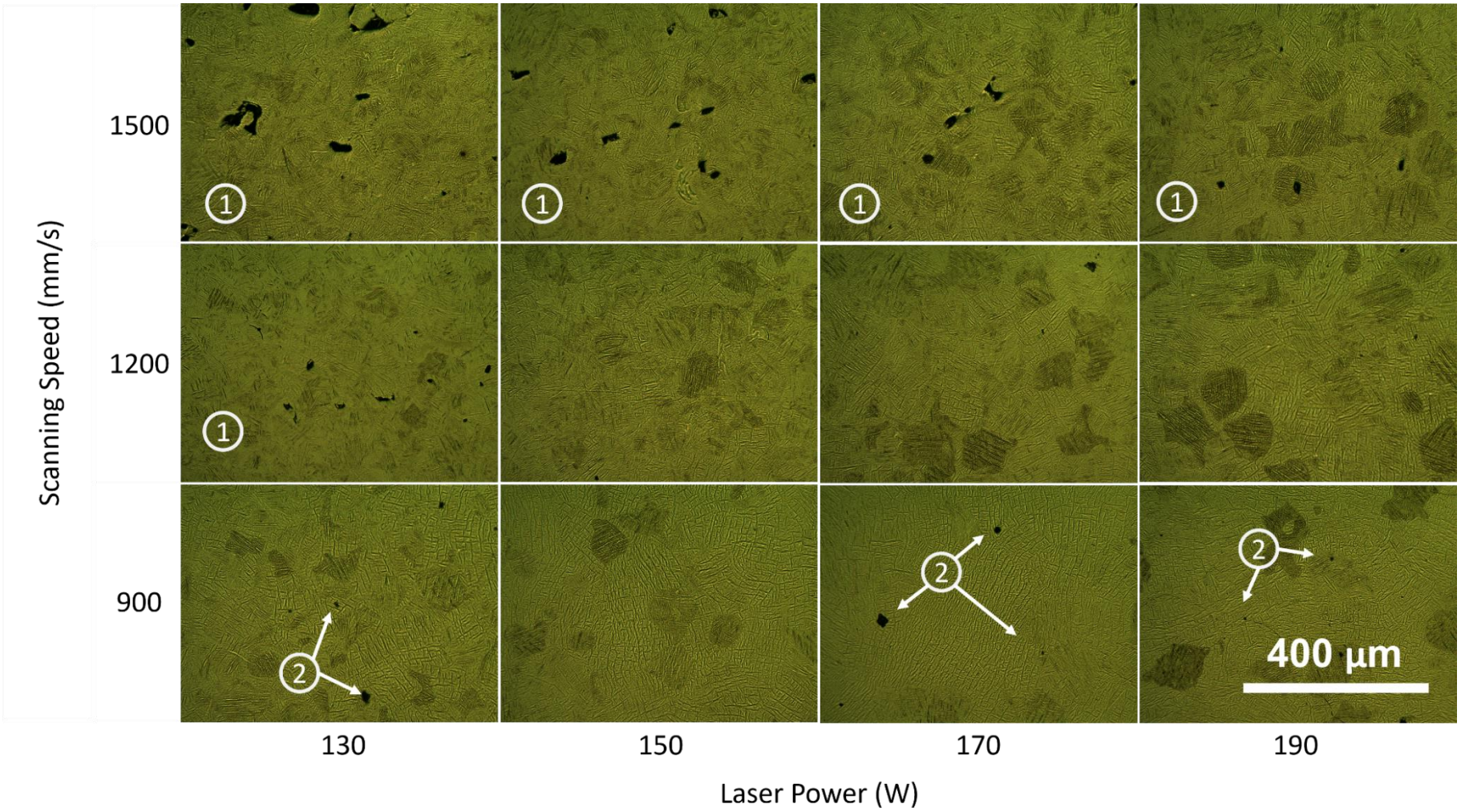

Figure 3.8: Ti64 etched cross-sections presented with respect to build parameters of laser power and scanning speed. Section is in the horizontal plane, perpendicular to build direction.

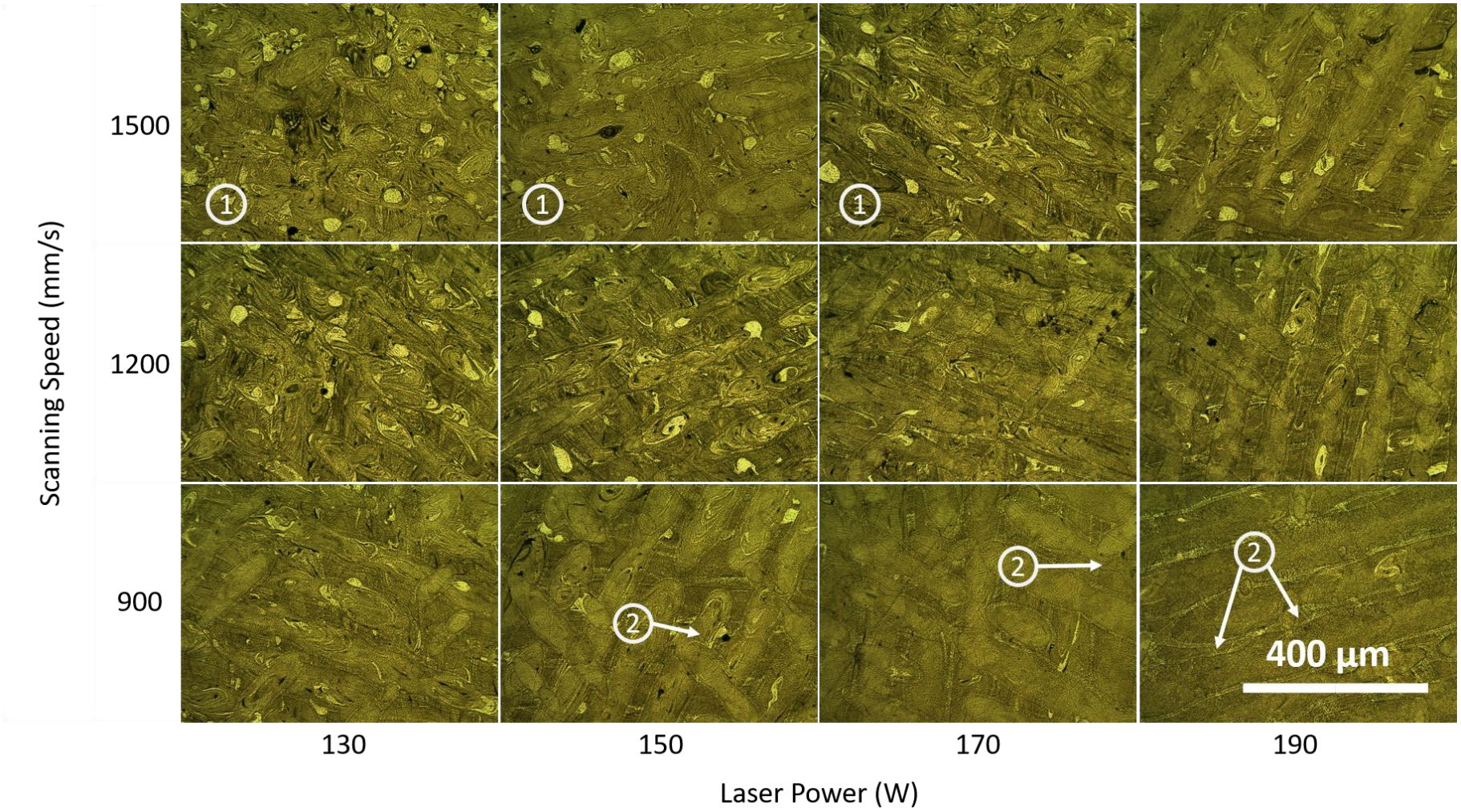

Figure 3.9: Ti64+B etched cross-sections presented with respect to build parameters of laser power and scanning speed. Section is in the horizontal plane, perpendicular to build direction.

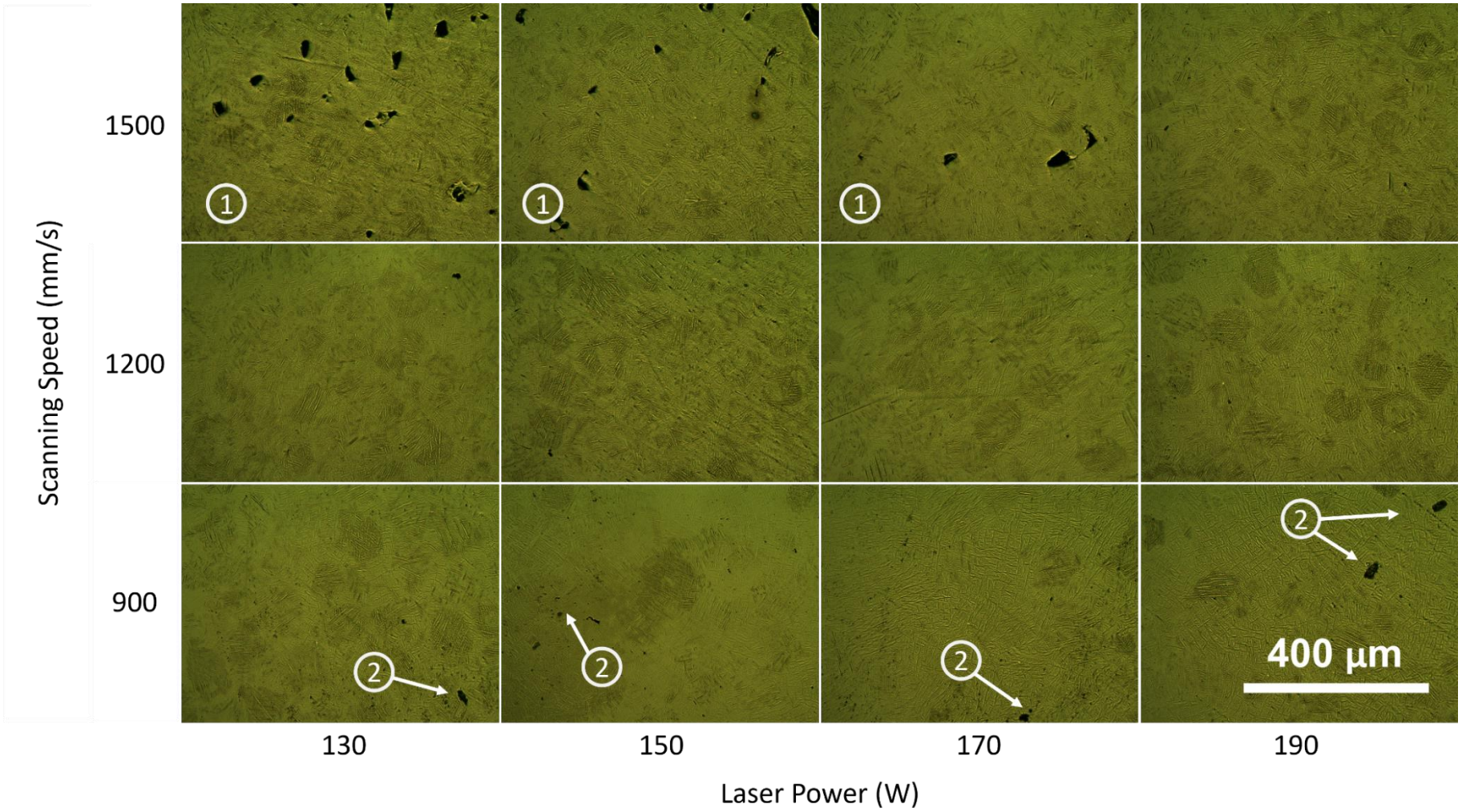

Figure 3.10: Ti64+O etched cross-sections presented with respect to build parameters of laser power and scanning speed. Section is in the horizontal plane, perpendicular to build direction.

The porosity in the low energy density region (‘1’) of the material cross-sections is typical of lack of fusion (LOF) porosity. This type of porosity is identified by its irregular shape and large size [86]. The mechanism behind forming these pores is due to insufficient energy input to melt all the material under the laser. Solidification occurs too rapidly for the liquid to flow, fill, and wet any irregularities in underlaying layers and as such pores are formed [64, 66]. LOF porosity and its mechanism have been studied extensively and related to numerous parameters of the SLM process including energy input and powder feedstock properties (size, gas entrapment, morphology) [134, 135].

The second area where pores are observed is also an expected feature when high energy density parameters are used for SLM parts. The type of porosity known to occur with higher energy input is gas entrapment porosity [70]. In SLM processing the high rate of temperature change, application of very intense energy, and gas forces, result in a highly dynamic melt pool. This can cause a process that results in gas bubbles forming or being trapped in the molten metal leading to more regular, spherical shaped pores. A form of gas entrapment is through a mechanism known as keyhole porosity, which occurs with too much energy input to the melt pool [71]. When this happens the melt pool becomes larger and deeper with the incident laser forming a “keyhole” or pit within the molten metal. This further increases the laser energy absorbed due to internal reflection within the keyhole pit [136]. These keyholes can collapse, entrapping gas [72]. Pores that are characteristic of keyhole porosity are typically quite large spherical pores (up to 50 μm diameter). These occur with regularity throughout the material due to high energy processing parameters enabling this keyhole mechanism to continue to take place [137].

No distinctive keyhole pores are observed in Figure 3.8, 3.9, and 3.10 indicating that porosity at increased energy density levels was not due to this mechanism. However, other methods of gas entrapment can occur at increased energy input through: melt pool instability, pores in the feedstock powder, gas absorption of the melt, and localised vaporisation [65, 138]. Gas entrapment porosity is recognisable by the spherical, more regular, pores it forms. The pores in the lower right of Figure 3.8, 3.9, and 3.10 (‘2’) appear to have this more regular shape

identifying them as likely gas entrapment pores. The formation of this porosity indicates that the energy input in this region is causing instability within the melt to entrap some gas however it is not so high as to cause the keyhole mechanism to take place which results in more significant porosity as described previously. .

The microstructures of Ti64 (Figure 3.8) and Ti64+O (Figure 3.10) appear very similar across the range of manufacturing parameters. Both materials show the same difference in appearance with respect to processing parameters. LOF pores occur in both materials at low energy density (‘1’) and there is some evidence of gas entrapment pores with higher energy input parameters (‘2’). Identifying parameter regions with porosity provides an explanation for some of the changes in density observed previously and helps to support the selection of parameters from regions of high density for the Ti64 and material with additional oxygen.

In comparison, Ti64+B (Figure 3.9) presents a very different microstructure. In Ti64+B samples there are clear parallel lines running through each micrograph with some images displaying overlapping sets of parallel paths at angles to each other. The angle between these overlapped features is a constant 67° through all micrographs of this sample. This angle has a clear explanation as these cross-sections are all in plane with the build layers. The laser scanning hatch pattern is rotated by 67° every layer so clearly these features align with the scanning pattern. The rotation of the pattern is a feature of the standard operating parameters on the EOS system to reduce porosity by preventing alignment of scan paths between layers. Clearly the addition of boron is influencing the material and causing it to retain some feature of the laser scanning paths as this is not clearly present in other materials of this study.

In the boron modified material it is possible to identify material segregation features. At low energy density there is a clear distinction between some light and dark areas. Figure 3.11 presents a closer inspection of these regions of different contrast.

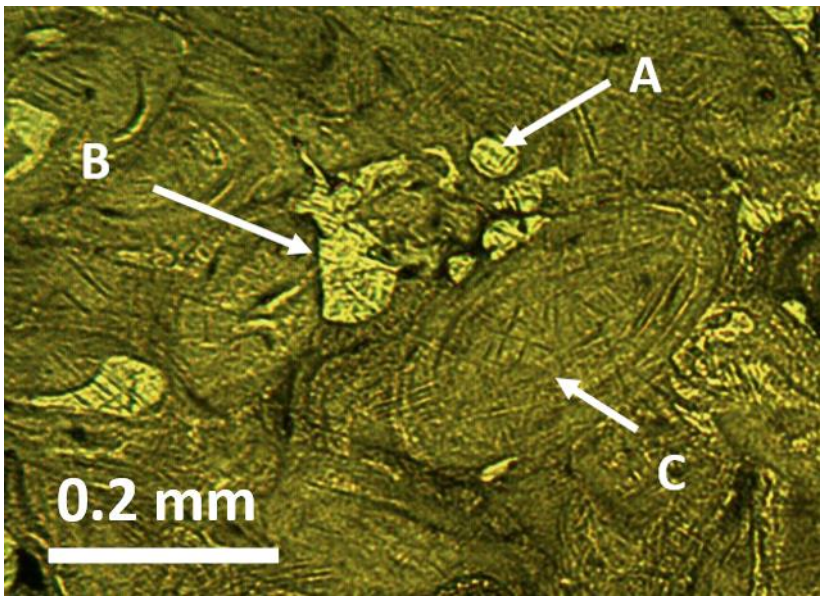

Figure 3.11: Ti64+B cross section detail image presenting incomplete melting and segregation of phases. 'A' indicates a circular, light feature that is indicative of an unmelted powder particle. 'B' indicates a light region of material that has not incorporated the boron additive. 'C' indicates a darker region of material that indicates it has blended well with the boron.

Some of these light areas appear circular in nature (Figure 3.11 'A'). From this shape it can be concluded that these are metal powder particles that are not fully melted by the process, as is evident from their scale matching that of the feedstock powder (15-45 µm). These particles are unmelted in the process and appear with light shading. This appearance must be indicative of material where no boron has been incorporated, therefore having an appearance of only Ti64. Further, the differing contrast regions in the Ti64+B etched cross sections can only be the result of the added boron as the other materials (Ti64 and Ti64+O) do not display this feature despite all other manufacturing conditions being equivalent.

Other areas in the micrograph of Figure 3.11 and some micrographs of Figure 3.9 present highly swirled patterns that have the appearance similar to partially mixed paints or liquids. These swirled regions comprise of light ('B') and dark ('C') contrast regions. The light regions share contrast with the unmelted particles. This identifies them as regions that have not blended well with the boron during solidification. Where the microstructure is darker it indicates that boron has mixed into the material, altering its appearance in the etched cross-sections.

From the micrographs of the boron modified material in Figure 3.9 it can be seen that the more severe regions of incomplete mixing occur in regions with LOF porosity seen in the Ti64 and Ti64+O microstructures (Figure 3.8 and 3.10). This corresponds to lower energy densities where not all the material is melted under the laser and so cannot blend and incorporate the additives. Reduced energy density would also suggest reduced solidification time of the melt pool due to lower overheat of liquid metal in the melt pool. This would reduce the time where material in the melt pool is able to flow, resulting in poor mixing.

At higher energy density (bottom right of Figure 3.9) there appears to be a reduction in these segregated regions, indicating better mixing with the boron as the overall contrast appearance is more homogeneous.

From identifying pores and their relation to parameters a more informed decision can be made about an operating point for further investigation of mechanical properties. The region of parameters that produce low porosity and appear to incorporate the added materials, as identified by microstructures, have an energy density between 47 and 55 J/mm^3. In literature an operating point for processing Ti64 materials has been identified as being around 65 J/mm^3 [139] which corresponds well with the observations of this investigation.

3.4 Effect of Process Parameters on Material Hardness

Another aspect of this work is to investigate the effect the different additives have on the hardness of Ti64. The additives to Ti64 are expected to result in changes in hardness through different mechanisms, including: particulate reinforcement, grain refinement, and interstitial hardening. To help identify a suitable operating point for processing parameters their relation to hardness needs to be characterised. This will help in selecting parameters for further study that take any changes in hardness into account. The parameters and procedure for this data is presented in methods section 2.4.1.

Microhardness was investigated for Ti64, Ti64+B, and Ti64+O. Presenting average microhardness of the different materials shows clear increase in average hardness with the addition of both additives (Figure 3.12). This section will only focus on any relation between hardness and manufacturing parameters. Further investigation

into the difference in hardness between materials will be explored in the following chapter on material properties.

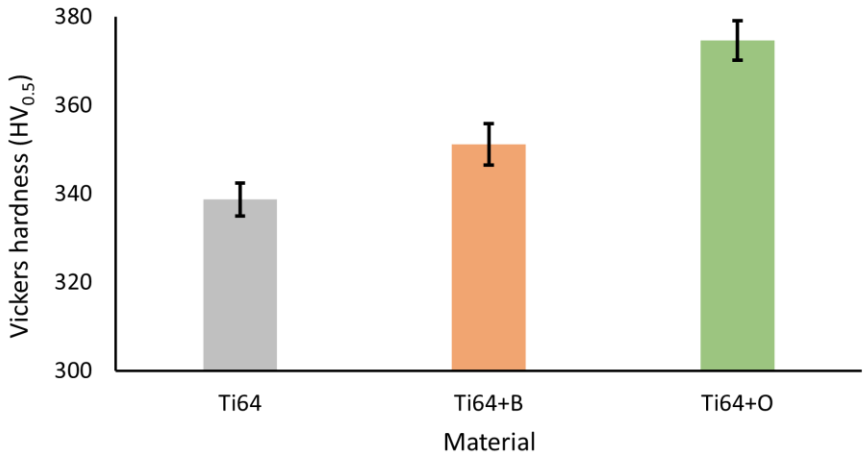

Figure 3.12: Average hardness of SLM printed Ti64, Ti64+B, and Ti64+O.

To determine trends in hardness with respect to fabrication parameters the hardness data across the range of build parameters was normalised with respect to the average hardness for each material from Figure 3.12. These normalised hardness results are presented in Figure 3.13.

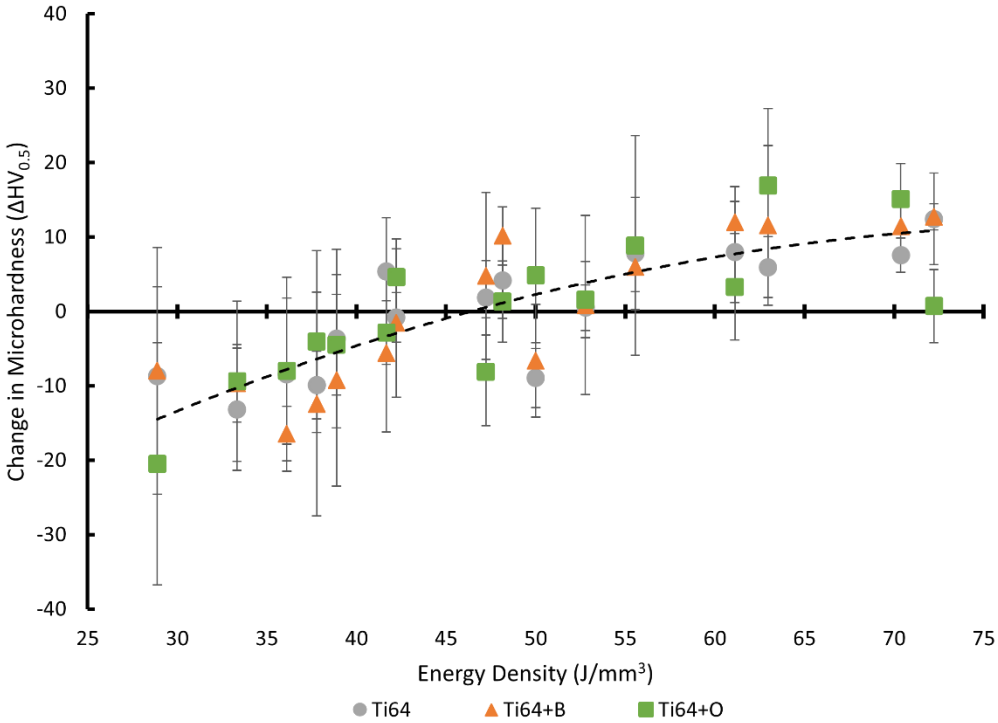

Figure 3.13: Normalised Vickers hardness ($HV_{0.5}$) with respect to fabrication energy density for Ti64, Ti64+B, and Ti64+O.

Comparing the normalised hardness of the materials with energy density in Figure 3.13 there is an increase in hardness with increased energy density. There is also

a decrease in hardness variability with increasing energy density as presented in Figure 3.14 showing size of the confidence intervals for hardness data. Comparing these trends in hardness with features presented in the micrographs of Figure 3.8, 3.9, and 3.10 presents some explanation for the features seen.

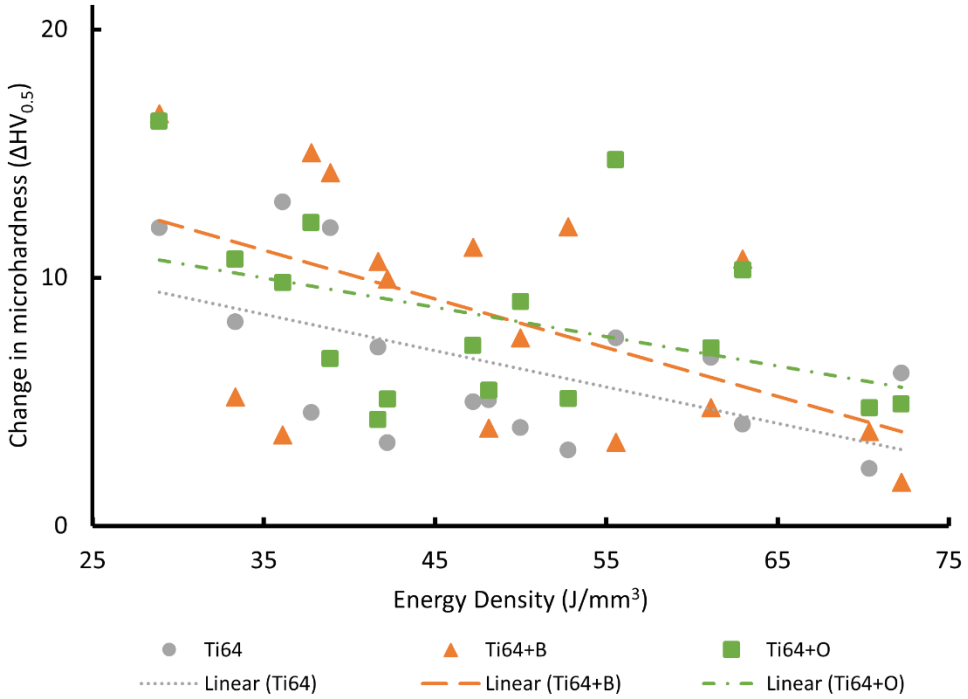

Figure 3.14: Size of 95% confidence intervals (CI max–CI min) from Vickers hardness measurements in Figure 3.13 with respect to energy density for Ti64, Ti64+B, and Ti64+O.

At low energy densities hardness is more variable, which corresponds well with incomplete particle melting and segregation of different phases, most clearly seen in the Ti64+B (Figure 3.9). The measurements made are microhardness indents on polished samples without etching where no visual distinction can be made between different phases and as such was a randomisation of measurement locations. Measurements of Ti64+B would likely be taken in locations that incorporated boron as well as in areas unmelted or unmixed which would have resulted in the greater hardness variation seen in Figure 3.14.

As a similar trend of large hardness variation at low energy density is seen across all materials in Figure 3.14, this provides evidence that there is incomplete mixing of the different added materials and incomplete melting of the starting powders. Incomplete mixing and melting would generate regions of differing hardness and

present as large hardness variation. This effect could also be true for the Ti64 as unmelted powder particles may have a different hardness to the resolidified SLM melt material (Figure 3.8). At higher energy density the Ti64+B appeared more homogeneously mixed in the earlier micrographs and correspondingly there is a reduction in hardness variation.

The apparent increase in hardness of the materials with increasing energy input can also be explained through the more homogeneous distribution of the additives in the material. When evenly distributed, the additives would increase the average hardness with reduce variability. With incomplete mixing, the comparatively less hard, unmodified, Ti64 that is present due to unmelted powder, would appear as regions of lower hardness in these materials, increasing variability. Regions of high hardness where the added materials are incorporated appear alongside the unmelted Ti64 regions. This is evident in the hardness results presented by Figure 3.13 as the upper bound of the 95% confidence intervals at low energy density almost encompasses the mean hardness of samples at higher energy input.

The material hardness and variability in hardness can serve to inform selection of process parameters for manufacturing the modified Ti64 materials. Low variation in material hardness can be used as a representation of material homogeneity and incorporation of the boron and oxygen additives. Parameters resulting in energy density above approximately 55 J/mm^3 result in high hardness with reduced variation.

3.5 Composition Qualification

Consolidation of blended feedstock powders by SLM has the potential to change the composition of the resultant material. Figure 3.15 present SEM images of Ti64 powder that has been blended with the amorphous boron and TiO_2 additives. The particulates of different additives are clearly seen on the surface of the titanium powder particles as small white flakes which appear distributed throughout the sample. As the additives are simply blended the resulting powders are still two separate materials that may become selectively separated through different mechanisms.

The process of SLM is very volatile at the melt pool due to the intense and highly localised heat input. As the boron and oxygen have been simply incorporated by mixing the two powder feedstocks they appear as particulates on the surface of the Ti64 powder (Figure 3.15). These surface particulates may become detached and ejected by laser-induced gas/vapour jets [140]. The intense local heat can also cause the selective evaporation of different alloying elements under the laser [141]. These effects may result in the consolidated material having a different composition than expected.

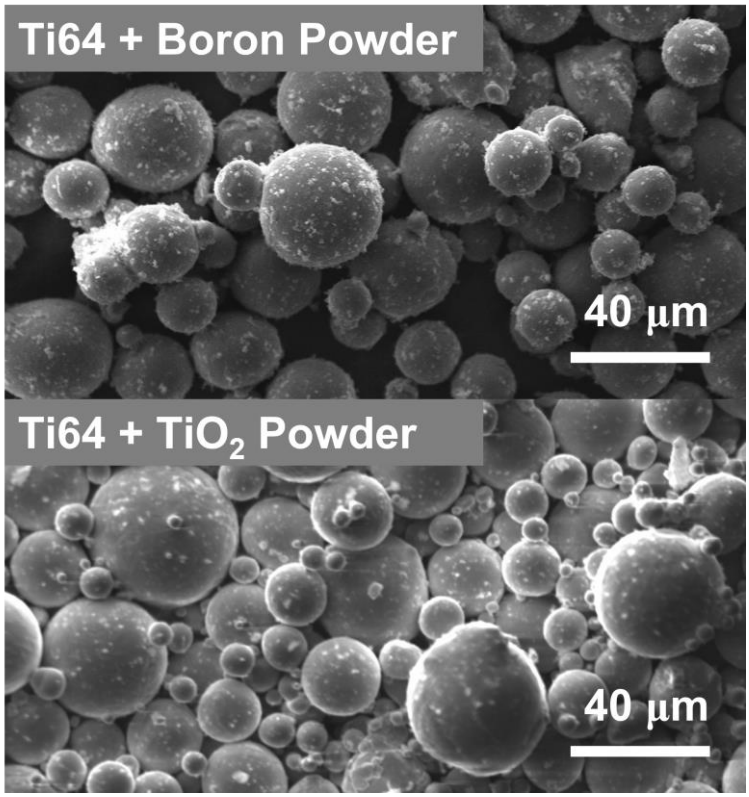

Figure 3.15: Ti64 powder blended with amorphous boron and TiO_2 powder.

To confirm the composition of the final materials, energy dispersive X-ray spectroscopy (EDS) was used. This technique has a detection threshold of 0.2wt%, it is also inherently difficult to detect light elements like boron due to the elemental emission peak overlapping with heavy elements and low fluorescence yield [142]. Due to these challenges, EDS results were limited to verifying the bulk composition of the Ti64 with regards to ASTM-B348 specifications [11]. The results in Table 3.2 identify that the bulk Ti64 alloy falls within ASTM limits for concentrations of elements within detectible limits. The samples were prepared for EDS by polishing using silicon carbide and colloidal silica so there is likely to be

some silicon residue detected. The large variation in the silicon content (95% confidence interval values) support this case as there is variation as large or larger than the amount detected and as such the silicon measurements presented by EDS are likely not representative of any silicon contamination in the material itself.

Table 3.2: Results of Energy Dispersive X-ray Spectroscopy (EDS) for SLM manufactured Ti64 and SLM Ti64 with added boron and oxygen. The ASTM standard composition for Grade 5 Ti64 is also presented. Results are in wt%. Boron and oxygen are below detectible limits of EDS.

Material		B and O	Ti	Al	V	Fe	Si
SLM Ti64	Average	-	89.48	5.99	3.88	0.22	0.07
	95% CI	-	1.16	0.08	0.33	0.35	0.05
SLM Ti64+B	Average	-	89.98	5.99	3.94	0.06	0.04
	95% CI	-	0.18	0.19	0.15	0.08	0.05
SLM Ti64+0	Average	-	90.21	5.87	3.74	0.12	0.07
	95% CI	-	0.13	0.05	0.11	0.17	0.10
ASTM-B348 Grade 5 [11]		-	Balance	5.5-6.5	3.5-4.5	<0.4	<0.1

As EDS was unable to provide an accurate quantitative measure of boron in the final material, Laser Ablation Inductively Coupled Plasma Mass Spectrometry (LA ICP-MS) was used. Table 3.3 presents the summation of LA ICP-MS results from different samples of Ti64 and Ti64+B.

Table 3.3: Results of Laser Ablation Inductively Coupled Plasma Mass Spectroscopy (LA ICP-MS) for SLM manufactured Ti64 and SLM Ti64 with added boron. A sample of Grade 5 Ti64 plate has been included as a comparison. The results are presented in wt%.

Material		B	Al	V	Fe	Si
SLM Ti64	Average	0.00	6.93	4.03	0.13	0.17
	95% CI	0.00	0.29	0.12	0.004	0.03
SLM Ti64+B	Average	0.25	6.67	4.06	0.04	0.37
	95% CI	0.015	0.24	0.11	0.002	0.11
Ti64 Plate Reference	Average	0.00	7.36	4.12	0.16	0.42
	95% CI	0.00	0.25	0.17	0.01	0.20

The results in Table 3.3 showed that boron was successfully retained and incorporated into Ti64 through blending and subsequent SLM processing. The amount of boron detected in a manufactured sample, 0.25wt%, was only slightly lower than the amount added to the powder during simple blending, 0.27wt%. This indicates that almost all the added boron powder was successfully incorporated into the samples when the blended powder was processed by SLM. The small discrepancy between the boron powder added to the SLM feedstock powder and the measured amount in the samples may have been lost from the system during powder handling, or during manufacture through interaction with the laser as described earlier.

Any loss of a small amount of boron within the fabricated samples has little impact on this work as it is consistent between samples, as indicated by the narrow 95% confidence interval. This work investigates the potential of incorporating a small amount of boron via this simple powder mixing approach so this small variation in composition is evidence that the boron is being incorporated effectively with little difference between samples. Further work could pursue any influence of the process on the loss of boron where a specific added amount is more critical.

Some variation is to be expected from the boron composition results as the Ti64 and boron are simply mixed and rely on the SLM process to incorporate them into the material. This might give rise to different local concentrations within the samples, however, the observed low variation in boron concentration gives confidence that the boron distribution in the materials is quite consistent. There is high confidence in the boron content reported by LA ICP-MS results as a NIST SRM610 calibration sample was run alongside the titanium materials. This standard has levels of boron (1 wt%) comparable to that used in the boron modified material of this study and provided a quantitative reference.

The LA ICP-MS experiment identified that aluminium was present at higher amounts than the given specification for both Ti64 materials while vanadium and iron levels were within ASTM B348 limits [11], Table 3.2. This result is consistent through the Ti64 plate reference too with no indication as to the cause. Silicon was also reported at levels above those given in the ASTM standard however this could

be caused by the sample preparation technique as described earlier when discussing EDS results.

The laser ablation process may cause a selective evaporation of aluminium and so report slightly higher detection. This has been observed with metal samples [143] and it is through this process that the high concentration of aluminium may be attributed. Laser ablation equipment for sampling material composition draws parallels to the SLM process in this respect. The selective evaporation of elements has been observed in the SLM process itself when very high energy input is used [141, 144]. Under these conditions, aluminium was shown to be susceptible to preferential ablation. If this was to have occurred in the fabrication of these samples the aluminium level would appear lower in the results of Table 3.2 and 3.3, which is not the case so the fabrication of samples can be ruled out from causing significant change to the composition.

Oxygen has a significant influence on the properties of titanium and the level of additional oxygen incorporated into the modified material required measurement to determine the final compositions. EDS and LA ICP-MS were both unable to measure oxygen contents of the materials due to low concentration, low atomic mass, and reactivity. For this purpose, the oxygen content was measured using Inert Gas Fusion analysis. The manufacturers report for the base Ti64 powder reported an oxygen content of less than 0.16 wt%. Samples of each of the manufactured materials were tested to confirm the base oxygen level and additional oxygen added. The results are reported in Table 3.4 and confirm that there is little change from the original oxygen content for the materials with no added oxygen. Nitrogen and hydrogen are also reported from this testing and are well below the allowable limit for grade 5 titanium.

Table 3.4: Inert gas fusion composition results from different titanium samples.

Material	Oxygen (wt%)	Nitrogen (wt%)	Hydrogen (wt%)
Ti64	0.153 ± 0.003	0.03 ± 0.001	0.002 ± 0.001
Ti64+B	0.134 ± 0.004	0.02 ± 0.003	0.004 ± 0.001
Ti64+O	0.337 ± 0.004	0.03 ± 0.000	0.004 ± 0.001

These results confirm the material with additional oxygen did incorporate the additive during manufacture. An addition of 0.2wt% oxygen in the form of TiO_2 was made to this material. The difference between the oxygen enriched material and the base Ti64 powder is 0.184 wt%. This is very close to the amount added and it can be concluded that the simple blending approach is effective at incorporating additional oxygen during the SLM process. There is an indication that some of the added oxygen was lost during processing. It is expected that this could occur through similar mechanisms as the boron, including during powder handling, selective evaporation under the laser, or removal by gas forces during SLM. As with the boron addition, the true balance of oxygen is not the significant focus of this work. The study focuses on the process of incorporating oxygen using TiO_2 powder and comparison with boron addition by a similar method.

Taking account of limitations of the various composition measurement techniques used and the low variability in their results there can be confidence that the material meets ASTM grade 5 alloy specification. The amount of boron added is accurately reported by LA ICP-MS and clearly being entrained in the solid material after SLM processing of the simply blended powders. The oxygen measured in the Ti64+O sample also closely matches the amount added to the feedstock Ti64 powder before SLM processing. Both modified materials had low variability in concentration of the respective additives. From this it can be concluded that the SLM process effectively incorporated these materials into the consolidated samples.

3.6 Summary

Following the SLM parameter density study, a region of high density above 99% can be identified for Ti64 and Ti64+B above 40 J/mm^3. Further investigation of porosity and microstructures narrow this range to between energy densities of 44 J/mm^3 and 55 J/mm^3. Variation in relative density was shown to be fairly represented by the combined parameter of energy density, despite different power and speed levels having an effect. Increased porosity is the cause of low density at low energy density. Here, there was insufficient energy to fully melt and fuse the feedstock powder. Much smaller gas entrapment pores were also observed in the materials in samples made with higher energy input.

Hardness was found to increase with higher energy density, while variation in hardness was seen to reduce. This is attributed to reduced porosity and the more uniform distribution of hardening additives when processed with higher energy parameters. Energy density parameters with greater than approximately 55 J/mm^3 result in relatively low variation in hardness, indicating more homogeneous blending of the Ti64 and additives.

Operating parameters of 180 W laser power and 1100 mm/s scanning speed were selected for manufacturing samples for further testing. These parameters give an energy density of 54.5 J/mm^3 and fall within the region of density above 99% with low porosity. This parameter region has uniform distribution and incorporation of additives as identified by microstructures of the Ti64+B material and reduced hardness variability. A summary of relative density and hardness at these selected parameters is presented in Table 3.5.

Table 3.5: Relative density and hardness properties of Ti64 and modified Ti64 materials at the selected parameters of 1100 mm/s and 180 W.

Material	Relative Density	Vickers Hardness $HV_{0.5}$
Ti64	99.1%	356.2 ± 6.1
TI64+B	99.2%	391.0 ± 14.0
Ti64+O	99.2%	395.9 ± 7.4

While SLM has proven capable of fabricating these boron and oxygen modified Ti64 materials, further investigation is required to determine how the additives change the materials mechanical performance to identify new potential applications. Furthermore, post manufacturing heat treatment is common for SLM manufactured Ti64, for stress relief and to adjust other materials properties. The impact of heat treatments on these modified materials requires investigation as the effect further thermal processing has on the additives is unknown and could enhance or reduce any effects that they offer.

Chapter 4
Microstructure and Mechanical Properties

4.1 Overview

This chapter investigates the properties of SLM manufactured Ti64, Ti64+B, and Ti64+O parts, produced using a common set of SLM operating parameters, identified in the previous chapter. The impact of different commercially relevant heat treatment conditions (as-built, stress relieved and annealed) are also evaluated for their impact regarding the additives of boron and oxygen that are incorporated into the Ti64. This builds upon work in Chapter 3 which demonstrated the successful incorporation of boron and oxygen into Ti64 through the SLM process.

This study was carried out in two parts. The first investigates the microstructural changes for each of these three materials in three conditions by observing etched cross sections through the materials. The observations from this analysis are supported using X-ray diffraction (XRD) to identify phases present and the formation of new compounds e.g. TiB.

The second part examines the relationship between microstructure, and material properties of hardness and compressive strength. While this is well-known for Ti64, the behaviour of these modified materials and the effect of heat treatments on them are understudied.

The experimental method for this chapter is covered in method section 2.4.2. Specific experimental techniques in this chapter include: microstructural analysis, hardness, XRD, and compression testing.

4.2 Microstructure of SLM Ti64 and Modified Materials with Different Post Process Heat Treatments

Microstructures of the different materials are examined in different heat treatment conditions. These conditions are:

- As-built condition. This is relevant for the application of SLM parts direct from manufacturing.
- Stress relief treated at 700°C for 2 hours. This treatment is commonly applied to SLM manufactured Ti64 to remove any internal stresses that result from the thermal cycling and layer based build up of parts in this manufacturing process.
- Annealed at 920°C for 2 hours. Annealing can be performed to modify the microstructure of Ti64 to achieve different mechanical properties. The annealing process used in this study is also similar to a common hot isostatic pressing (HIP) thermal treatment. HIP is commonly used for medical and high-performance parts as it can reduce porosity. This treatment could help identify if these modified materials may be suitable for HIP processing.

Cross-sections of each material are examined in plane with deposited layers (horizontal X-Y plane) and sectioned through the deposited layers (vertical section).

4.2.1 As-built microstructure

Microstructures for the as-built condition of Ti64, Ti64+O and Ti64+B are presented in Figure 4.1, 4.4 and 4.7 respectively. Observed features are described and combined with XRD phase analysis enabling discussion of the mechanisms involved. Any differences in the as-built condition are also highlighted.

The as-built Ti64 material presents with a somewhat crosshatched lamellar structure throughout the material as shown in Figure 4.1. This is formed into colonies that have a relatively equiaxed shape in the horizontal section (size of about 100 µm), and long columnar shape in the vertical section of the material. Figure 4.2 identifies the scale of these long columnar grains within a range of 1-3 mm in length.

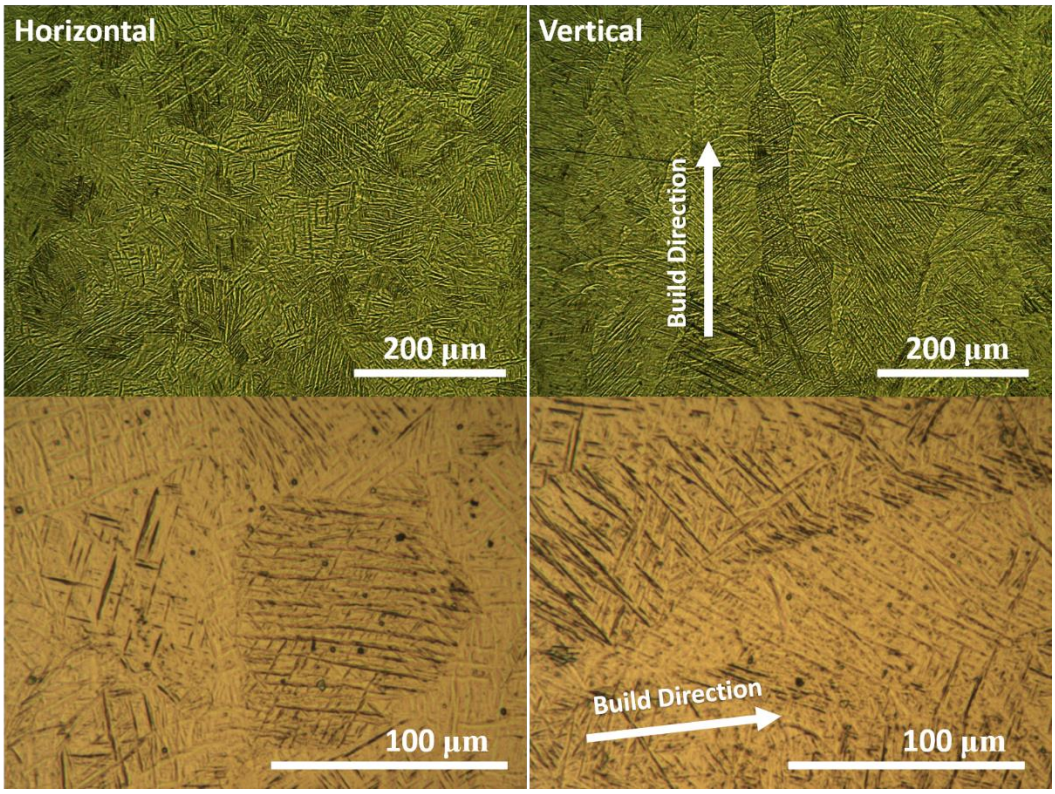

Figure 4.1: Ti64 microstructures for SLM as-built condition material. Horizontal and vertical cross-section micrographs are presented for different magnifications to show different scale features of the microstructures.

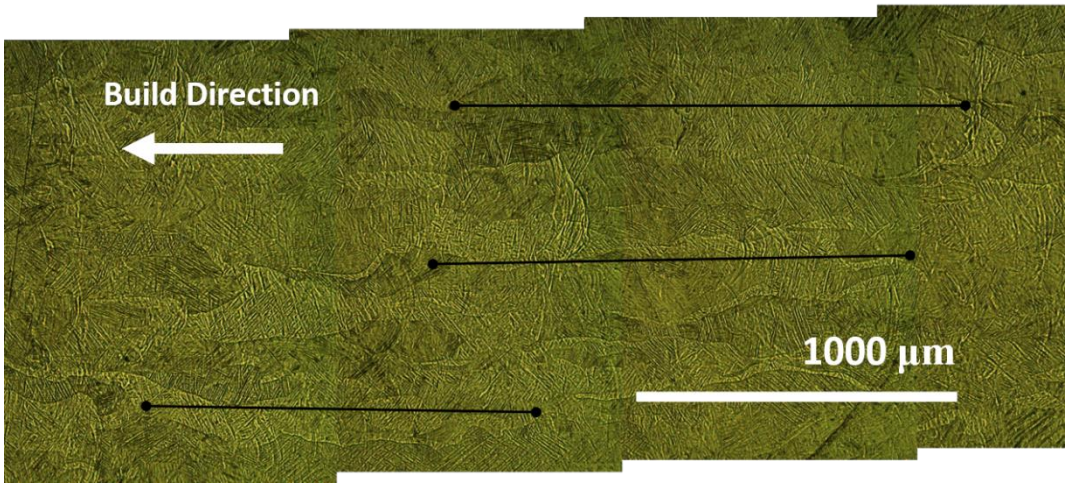

Figure 4.2: Combined micrographs of a vertical cross section of Ti64 in the as-built condition. This demonstrates the scale of columnar grains extending in the build direction (feature lengths highlighted by black lines).

Ti64 microstructures that result during SLM processing are well characterised in literature [10, 145-149]. The lamellar colonies observed in as-built Ti64 have been identified as α' martensite with the mechanism of formation well established by Yang, et al. [146]. The formation of α' martensite is due to high cooling rates (10^3

– 10^6 K/s [117, 118]) during the rapid quenching of material in SLM manufacture and reheating/cooling cycles of subsequent layers. These high cooling rates are greater than the critical cooling rate of 410 K/s [117, 150] allowing the diffusionless transformation of β phase (body centred cubic high temperature phase) into hexagonal α' martensite [146, 149].

The transformation process of β phase into α' martensite is responsible for the arrangement of the martensite lamellae into the colonies observed in Figure 4.1. α' martensite lamellae form with respect to the β phase via classical Burgers orientation relationship of $\langle 1\ 1\ 1\rangle_{\beta} \parallel \langle 1\ 1\ \bar{2}\ 0\rangle_{\alpha'}$[117, 146, 151]. The martensite primarily nucleates and grows from the parent β grain boundary. This mechanism will result in colonies of α' martensite lamellae of equivalent size to the β grain within which they form. These colonies are termed prior-β grains [150].

A further feature identified in Figure 4.1 is the distinct difference in colony alignment presented by horizontal and vertical sections through the materials samples. This is also an established phenomena of as-built SLM Ti64 where equiaxed lamellar colonies/prior-β grains present in horizontal sections while in vertical sections they display long columnar prior-β grains extending in the build direction (Figure 4.1 and 4.2) [10, 86]. Researchers have investigated and characterised these anisotropic microstructures of SLM Ti64 and their mechanisms of formation [86, 96, 100, 152]. The epitaxial grain growth through the layers is the result of directional solidification of the transient melt pool, driven by the net direction of heat conduction into prior layers [74]. This results in grain growth through the build layers. These grains span multiple layers due to remelting and directional solidification.

XRD results presented for the as-built SLM manufactured Ti64 in Figure 4.3 match well with the reference peaks of α titanium, although there is a slight right shift in the peak positions. No obvious β phase signal is present.

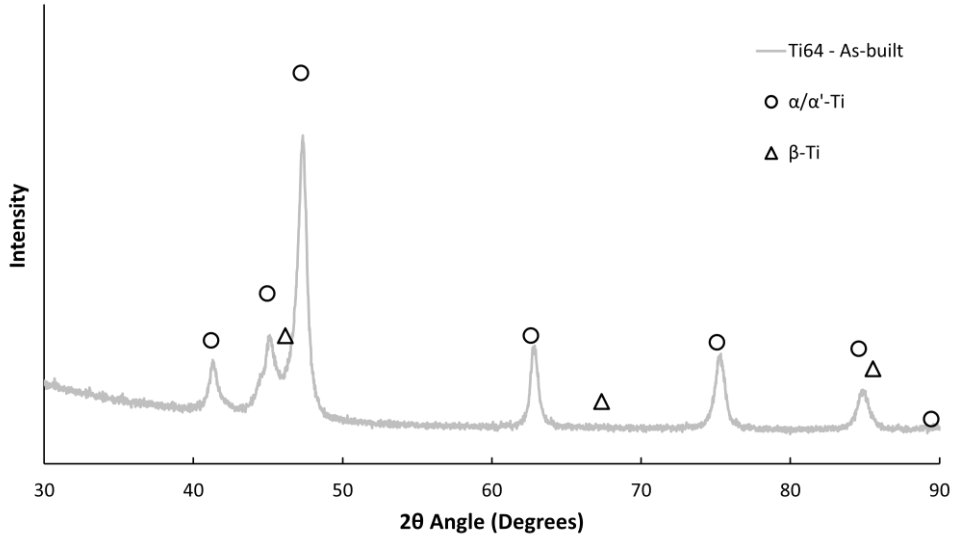

Figure 4.3: XRD pattern for SLM manufactured Ti64 in the as-built condition. Positions of titanium α/α' and β phase reference peaks are indicated for phase identification of the measured pattern.

α' martensite and α phase share a very similar hexagonal close packed (HCP) crystal structure [147]. A small difference can be observed between these phases under optimal conditions with the α' martensite having a small shift to slightly higher diffraction angles in XRD pattens due to the substitution of alloying elements (Al and V) [146]. A shift in the XRD pattern can also be exhibited by residual stress [153] so the distinction between α and α' phases is not conclusive for these SLM samples. α and α' phases can present together as reported by other researchers for Ti64 XRD [10, 154, 155]. Due to these influences the results of Figure 4.3 only identify α/α' and differentiation between these phases is made through other observations. If β phase had been present this would have indicated that α phase is present as α' martensite will decompose into α+β phase when subject to the correct conditions. Therefore, the absence of β provides evidence for the retention of α'. There is no identification of β phase in the as-built Ti64 of Figure 4.3 so the structure can be concluded to be fully α' martensite, in line with literature and microstructure observations [10, 86, 100, 146].

Ti64+O material in the as-built condition presented in Figure 4.4 has a very similar microstructure to that of the as-built Ti64 (Figure 4.1). Again, there is a lamellar structure throughout the material, formed into equiaxed colonies in the horizontal plane and columnar colonies in the vertical plane. There appears to be a distinct boundary region that surrounds the equiaxed lamellar colonies of the horizontal cross section. At higher magnification (bottom micrographs of Figure 4.4) there does not appear to be a discernible difference between the lamellar structure in the boundary region and that of the equiaxed colonies. Apart from the presence of the boundary region, there is no size difference between the colonies presented by the as-built Ti64 and the Ti64+O. These are 100 µm equiaxed in the horizontal section and 1-3 mm columns vertically through the samples as presented in Figure 4.5.

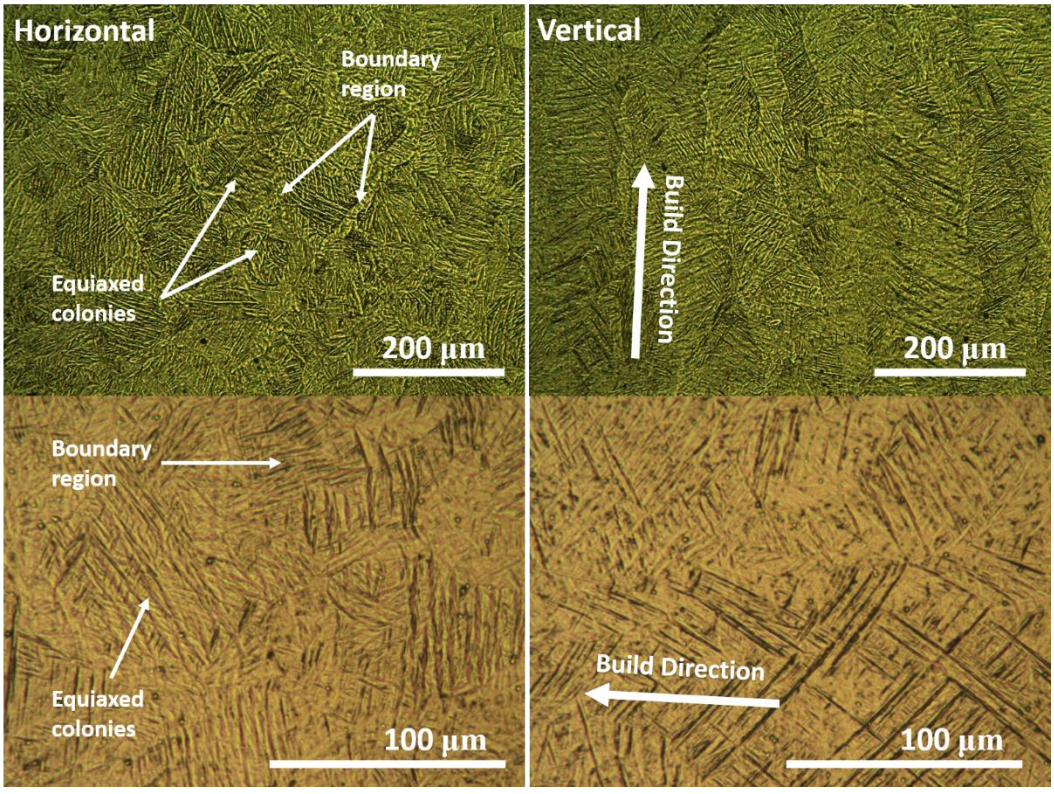

Figure 4.4: Ti64+O microstructures for as-built condition material. Horizontal and vertical cross-section micrographs are presented for different magnifications to show different scale features of the microstructures.

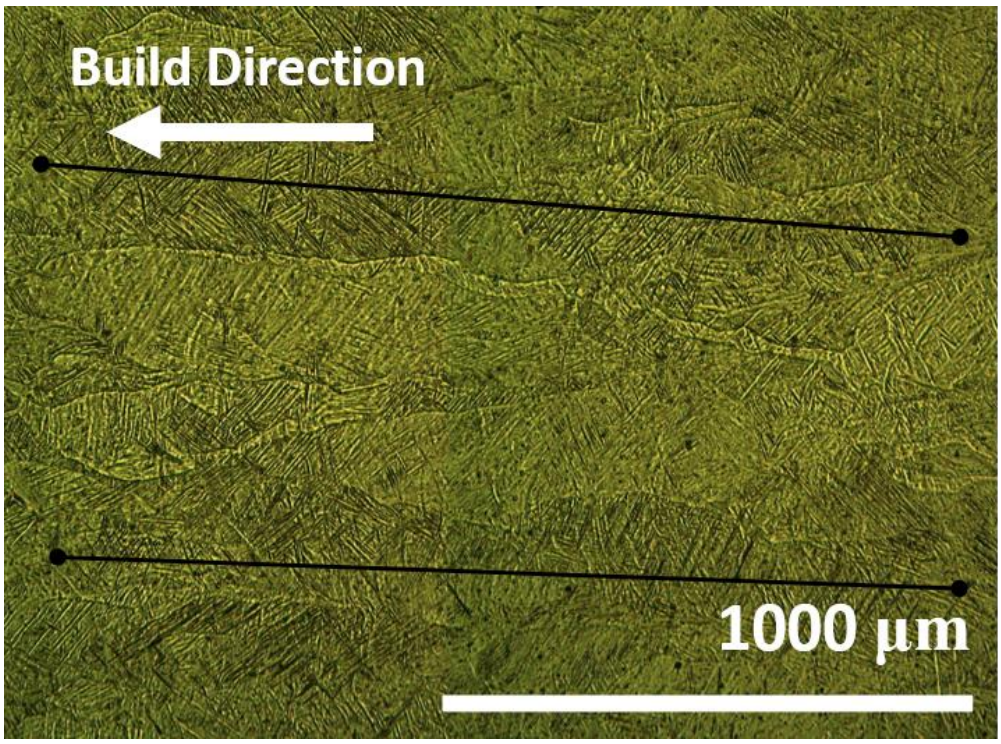

Figure 4.5: Combined micrographs of a vertical cross section of Ti64+O in the as-built condition. This demonstrates the scale of columnar grains extending in the build direction (lengths highlighted by black lines).

Oxygen is an α stabilising element in titanium alloys and also induces martensite transformation by increasing the β-transus and martensite transformation temperature [1, 156]. The overall phase of the as-built Ti64+O is therefore most likely to be α' martensite with the possibility of some α phase forming depending on the thermal history of the local region within the part [157].

Again, the columnar prior-β grains form as a result of remelting and directional solidification inherent in layer based additive manufacturing [86, 96, 100, 152]. The higher oxygen content has not served to change this phenomenon to any extent.

The boundary region around the equiaxed colonies has been observed before in SLM manufactured Ti64. Yang, et al. [146] identified this boundary region and attributed it to thermal history of the local area as adjacent laser tracks and subsequent layers overlap and remelt material in the manufacturing process. They identified the structure in this boundary as slightly coarser α' phase. This remelted/heat effected zone at the edge of laser tracks/prior-β grain boundaries may also transform some α' into α phase with increased oxygen content [158].

XRD analysis of the as-built Ti64+O in Figure 4.6 presents very similar peak positions when compared to as-built Ti64 under the same conditions. A subtle difference between the two materials is that the Ti64+O peaks are slightly left of those of the Ti64. As descried earlier, the difference between α and α' martensite phases are subtle however α peaks present at slightly lower angles compared to α' [146] and this peak shift may be evidence that more α phase is present with the addition of oxygen. The α stabilising effect of added oxygen would support this observation and a greater proportion of fine α lamella are likely to exist alongside α' martensite. This is not the only contributor as other factors such as stress can influence peak positions. Interstitial elements cause a stressing of the lattice, so the presence of additional interstitial oxygen could cause this result. The SLM manufacturing process results in residual stress within parts due to thermal cycling and sequential build-up of material, which would also contribute to this effect.

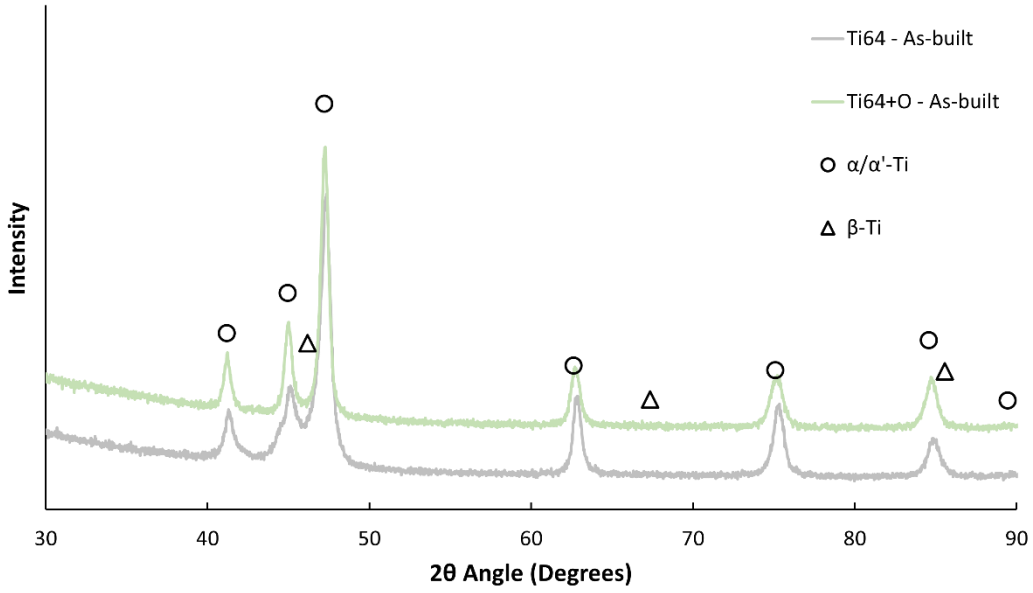

Figure 4.6: XRD pattern for as-built SLM Ti64+O compared to Ti64 in the same condition. Positions of titanium α/α' and β phase reference peaks are indicated for phase identification of the measured patterns.

The microstructure of the as-built Ti64+B material in Figure 4.7 is significantly different to that of Ti64. The horizontal section through the material presents a coarse pattern of parallel features overlayed at an angle upon other sets of parallel features. The centre distance between each parallel stripe is 100 µm, equal to the distance between each laser track. The angle between the overlayed parallel

features is 67°, the same as the amount of rotation made to the laser hatch pattern between every layer during deposition. These features therefore are related to the laser tracks of subsequent layers.

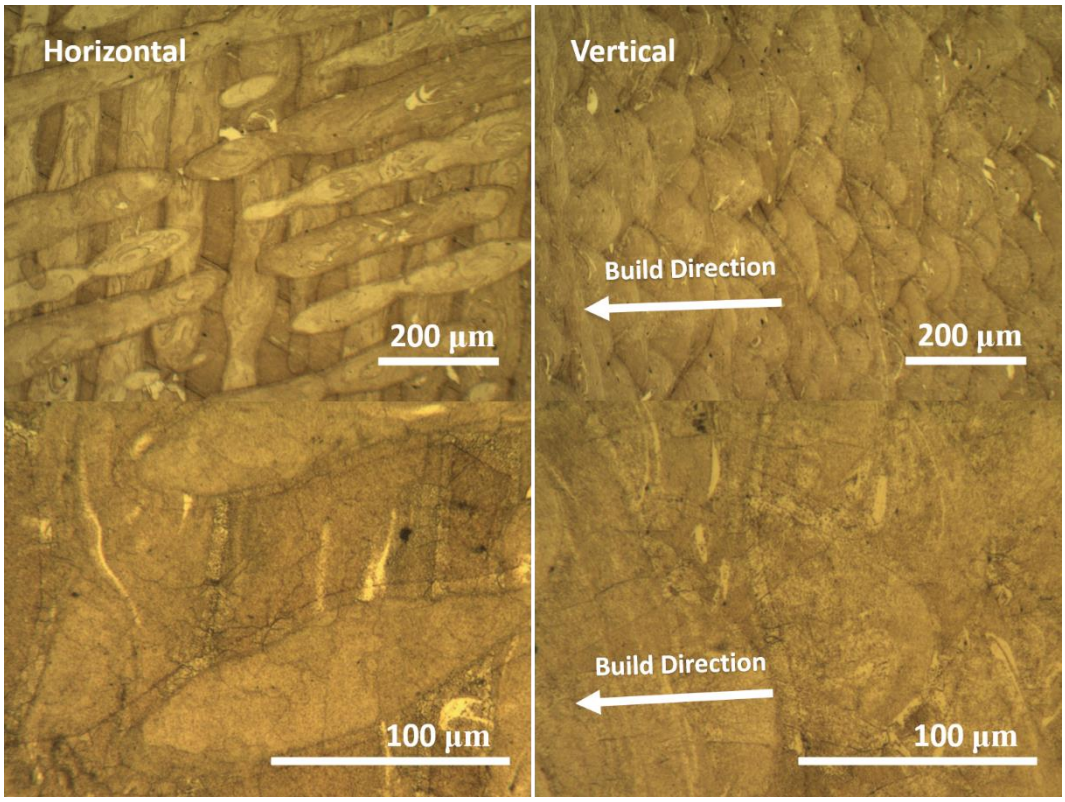

Figure 4.7: Ti64+B microstructures for as-built condition material. Horizontal and vertical cross-section micrographs are presented for different magnifications to show different scale features of the microstructures.

A further observation is that there is a thin band around the edge of each laser track, about 10 µm thick, with the edges of this band clearly distinct as darker lines giving the laser track features a skin and core type appearance. This is apparent around the edge of the tracks in the horizontal section and the edge of the scallop features in the vertical section. This boundary region is likely a heat affected zone of solid material surrounding the melt pool beneath the laser. Evidence for this can be seen in the higher magnification images of Figure 4.7. Different shaded regions of the material surrounding a laser track are seen to extend into the boundary region but do not continue into the laser track itself. This suggests that the boundary region was not melted by the track and its appearance is due to solid state mechanisms.

The vertical section has a somewhat scalloped or scaled appearance with overlapping semi-circular features that are all arranged in the same direction. These must also be features caused by the laser scan paths. These features are at least 50 µm deep in the build direction and appear to fully overlap with subsequent layers. The layer height was set at 30 µm in the build process so this clearly demonstrates that during manufacture the selected parameters are such that they partially remelt previously deposited material. The appearance of the scan pattern in the vertical section would result in the striped pattern observed in the horizontal section where the semi-circular features are representative of the depth of the melt pool along each track.

It is difficult to ascertain the underlying structure and prior-β grains in the optical micrographs of Figure 4.7 due to the coarse laser pattern features. Using SEM back scatter diffraction imaging it was possible to identify, in Figure 4.8, that the material did consist of lamellae. These are much finer than those of the Ti64 material without boron of Figure 4.1. The prior-β colonies also appear significantly reduced, being below 50 µm. There is no clear evidence of a difference in lamellar colonies between vertical and horizontal cross sections.

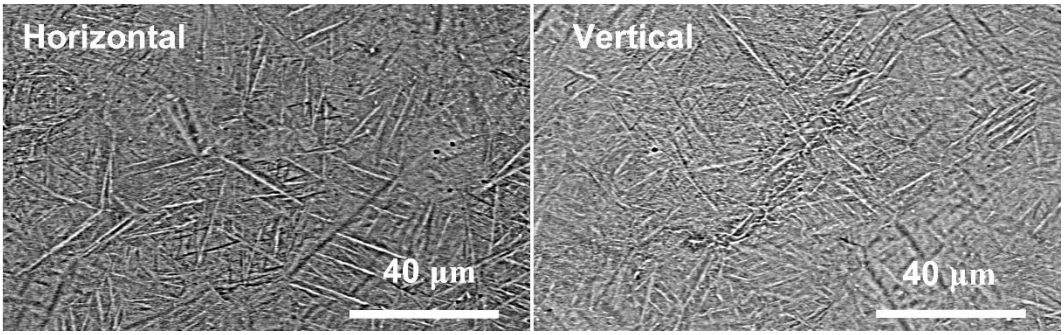

Figure 4.8: BSD image of Ti64+B in the as-built condition presenting a lamellar texture within colonies in the microstructure. Vertical and horizontal cross sections present almost identical lamellar and colony structure.

The lamellar structure and high cooling rates suggest the material primarily consists of α' phase within prior-β colonies. Literature also supports this as the negligible solubility of boron has no effect on the alloy phase transformations and α' martensite is still expected to form, as in the Ti64 sample [77, 159]. While boron is not soluble in titanium, it is highly reactive with titanium at the elevated temperatures of SLM processing and it is expected that all boron present in the

material will exist as reacted compounds of Ti_xB_y, such as TiB or TiB_2 [28]. Under SLM processing, TiB phase has been seen to form where boron has been introduced in the form of B_4C and TiB_2 [77, 123, 159]. This is attributed to TiB having the lowest free energy (ΔG) for reaction pathways with boron in excess titanium. TiB_2 has a more negative free energy of formation for titanium and boron, however in excess titanium, the formation of TiB from TiB_2 also has negative free energy and as such TiB is expected to form under SLM conditions [28, 160]. Any boron containing compounds would be expected to present as very dark features in BSD imaging however this is not evident in Figure 4.8 and is most likely due to the low levels of boron in the material and size of any boron compounds that form under rapid solidification in SLM.

XRD was used to further investigate phases formed under SLM processing of boron modified Ti64 (Figure 4.9. There is a very close peak match between the Ti64+B and the unmodified Ti64 in the as-built condition. The peaks observed correspond with the α/α' phase with no significant β phase detected. The boron modified material presented no additional XRD peaks, compared to the Ti64, that would be associated with the expected boron related phases.

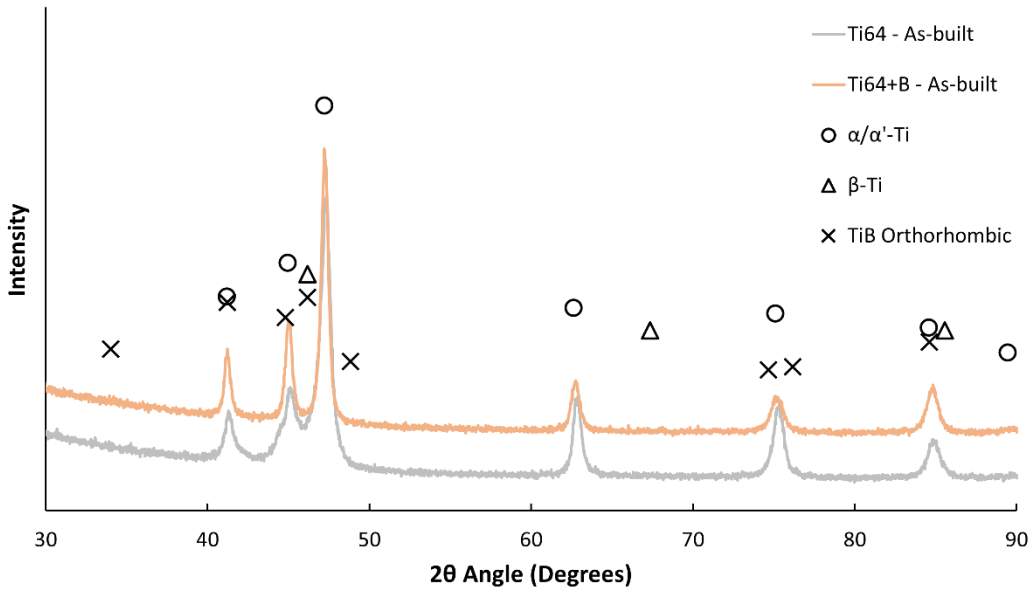

Figure 4.9: XRD pattern for as-built SLM manufactured Ti64+B compared with unmodified Ti64 in the same condition. Positions of titanium α/α', β, and TiB phase reference peaks are indicated for phase identification of the measured patterns.

The addition of boron is the only change made to the samples compared to as-built Ti64. This has resulted in significantly different microstructural features (Figure 4.7 compared to Figure 4.1). No identification of Ti_xB_y phases was made however it is most likely that TiB compounds exist on a small scale where observation/identification via BSD and XRD is not possible. The observed microstructural differences must be the result of the boron presence and interaction during SLM processing.

Boron has a significant grain refining effect on titanium which has been observed in previous studies [30, 40, 77, 161]. This occurs during solidification as boron is fully soluble within liquid titanium and precipitates as TiB during solidification by a eutectic reaction from liquid to β+TiB. The eutectic composition for Ti64+B has been measured at 1.55wt% boron [161]. Below this (0.2wt% in this study) solidification occurs in a hypoeutectic zone, within which β phase titanium grains nucleate and grow with boron rejected into the liquid due to its low solid solubility. This is shown to further nucleate fine titanium grains and restrict growth [77]. When the temperature falls below the eutectic temperature, 1545°C [161], the melt solidifies into TiB and β phase. Further cooling results in the diffusionless transformation of fine β grains into finer α' martensite. This mechanism results in the fine lamellar microstructures of Figure 4.8.

The formation of this fine microstructure also drives the macro features observed in optical micrographs of Figure 4.7. The grain refinement of boron eliminates the generation of larger prior-β grains observed in unmodified Ti64 and eliminates long columnar grains in the build direction. Each melt pool along a laser track solidifies under the influence of boron refinement and relative to the greatest thermal gradient. The heat affected zone surrounding each track is likely raised to temperatures that exceeded the β-transus, resulting in new β grain development from the previous α' martensite. With subsequent rapid cooling these β grains reform α' martensite in a different arrangement than it was previously, forming the identifiable boundary region. These combine into macro features where laser tracks are obvious in the microstructure and exhibit a layer-core appearance, similar to the effect observed in Ti64+O (Figure 4.4).

4.2.1.1 As-built microstructure summary

As-built Ti64 presented the expected microstructure for SLM manufactured titanium, with an α' martensitic structure formed in columnar colonies from prior-β grains.

The addition of oxygen had little impact on the microstructure but did form a boundary region around prior-β grains that is attributed to reheating of adjacent laser tracks and subsequent layers. The addition of oxygen made this effect manifest in an observable microstructural feature. No phase difference was identified, with the material consisting of α/α'.

Boron addition to Ti64 had a profound effect on the materials microstructure appearance. A macro texture existed that was the result of laser tracks, presenting as parallel tracks in the horizontal section and scalloped track cross sections in the vertical micrographs. This effect is the result of grain refinement that occurs due to the solidification influence of boron. The phase of the material was no different to that of Ti64, being α/α' phase, presenting as a finer lamellar structure. No Ti_xB_y products were detected in the material.

4.2.2 Stress relieved microstructure

Stress relief heat treatment was carried out in a vacuum furnace at 700°C for 2 hours to eliminate any residual stress that is induced by the thermal cycling and layer-based melt and solidification of the SLM process. This is a standard treatment of SLM manufactured Ti64 in commercial settings for geometric stabilisation of parts however it is at the upper end of what would be considered a stress relief for titanium [1].

Microstructures for Ti64, Ti64+O and Ti64+B are presented in the stress relieved condition in Figure 4.10, 4.12, and 4.14 respectively. Observations of microstructural features are followed by discussion relating to phase changes and transformations that may result from the thermal treatment. The influence of the modifying elements of boron and oxygen are accounted for through comparison with unmodified Ti64 after identical processing.

Figure 4.10 presents micrographs for the stress relieved Ti64. Overall, the material has a lamellar structure, with equiaxed prior-β grains in the horizontal section and columnar prior-β grains in the vertical section. There is little visual difference between the stress relieved Ti64 (Figure 4.10) and the as-built Ti64 material (Figure 4.1). Prior-β grain size remained the same at around 100 µm in horizontal section and columnar grains extending beyond the size of the single micrographs presented here (these were observed to be comparable to as-built structures at 1-3 mm).

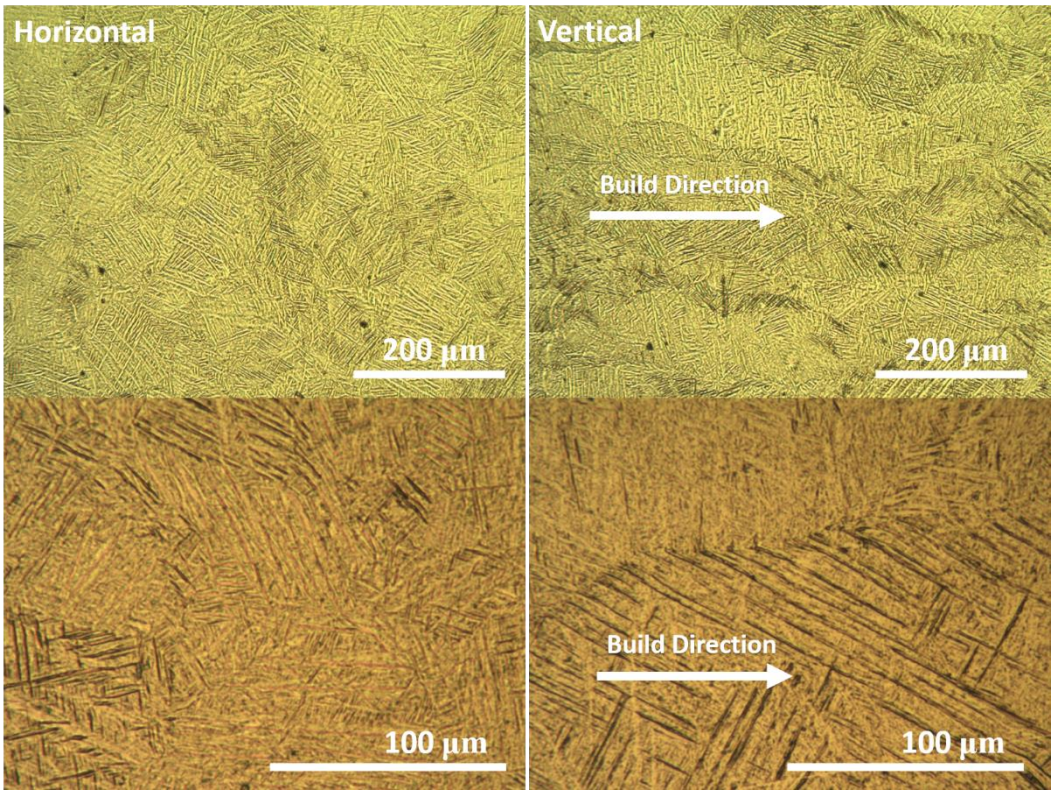

Figure 4.10: SLM Ti64 microstructures for stress relieved material. Horizontal and vertical cross-section micrographs are presented for different magnifications to show different scale features of the microstructures.

A heat treatment study of SLM manufactured Ti64 by Wu et al. [162] identified that up to 600°C there was no difference in heat treated microstructure from the as-built material. For treatments over 750°C an observation was made that the material became more susceptible to etching. This was attributed to diffusion of a large proportion of the initial α' martensite into α phase. Yu et al. [163] identified a small amount of β phase in SLM manufactured Ti64 using XRD after heat treatment for two hours at 750°C. XRD cannot easily distinguish between α'

martensite and α titanium as they have similar hexagonal structures. However, from the presence of a small amount of β phase they concluded that there was sufficient time for diffusion of α to form β phase within α lamellae. Other investigations of SLM manufactured Ti64 processed with similar heat treatments have identified the transformation of most α' to α phase, with some β phase identified with sufficient heat treatment time [96, 164, 165]. No change in prior-β structure occurred as expected from this sub-β transus treatment.

The stress relief treatment performed on the samples presented in Figure 4.10 is between the above referred studies so it is expected that a small amount of diffusion may take place however primarily most of the original α' martensite will transform to α phase, retaining the lamellar grain structure from the as-built condition. Some α' martensite may be retained after this stress relief however appearance wise it is indistinguishable from α phase.

XRD comparing the stress relieved TI64 to the as-built Ti64 in Figure 4.11 shows the two conditions are very similar. There is no discernible difference in peak positions with the material phase identified as α/α'. There is no evidence from XRD to suggest formation of β phase from the bulk transformation of α' into α+β, which in accordance with literature, suggests the α/α' phase structure remains [162, 163]. This transformation may have partially taken place however on a small scale where any β phase is below the detection limits.

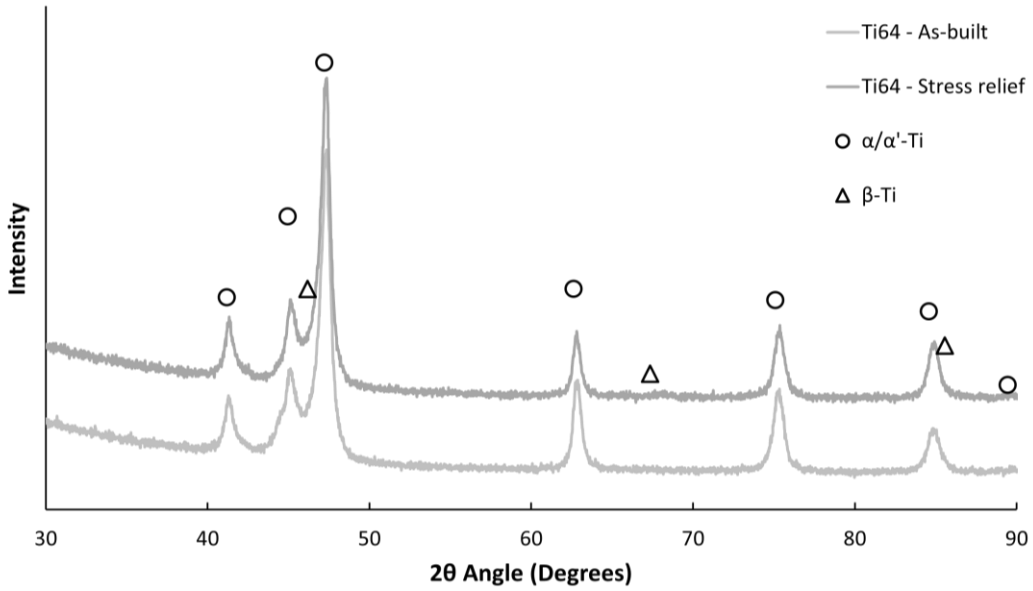

Figure 4.11: XRD pattern for SLM manufactured Ti64 in as-built and stress relieved conditions. Positions of titanium α/α' and β phase reference peaks are indicated for phase identification of the measured patterns.

The stress relieved Ti64+O microstructure of Figure 4.12 presents with lamellar structure arranged in colonies that are equiaxed in the horizontal section (100 μm diameter) and columnar in the vertical section (100 μm wide and greater than 600 μm long). The distinct boundary region around these colonies is also observable in both vertical and horizontal micrographs of the stress relieved TI64+O, as it was in the as-built material.

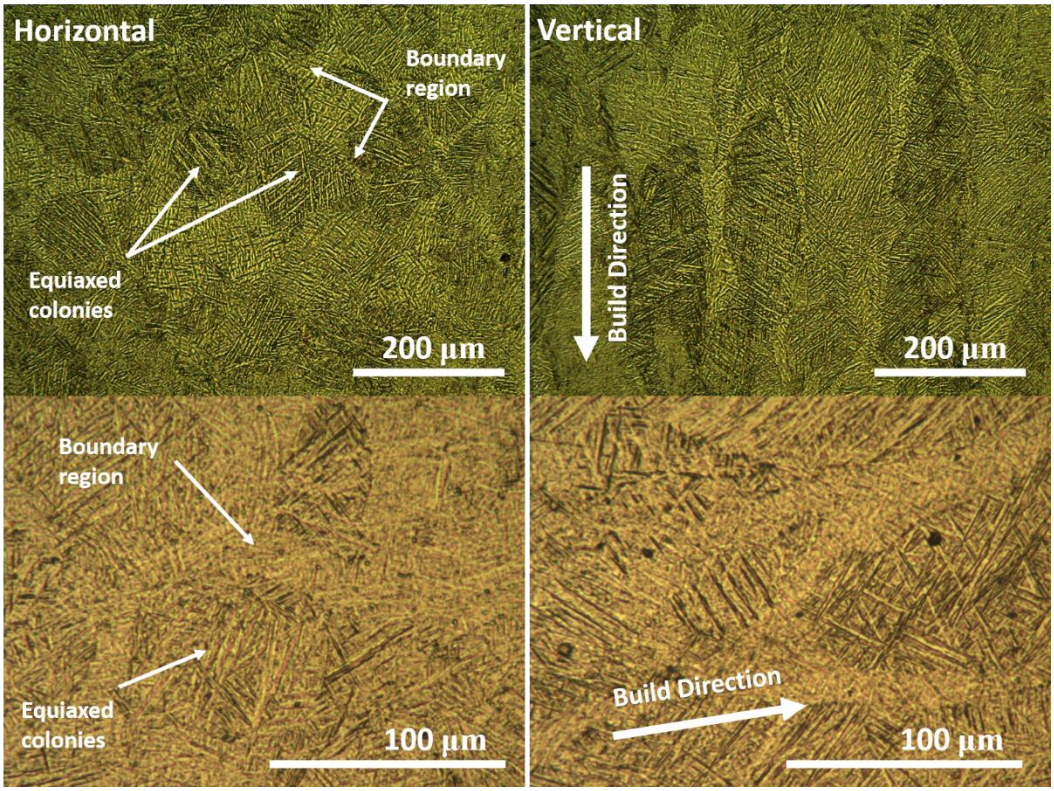

Figure 4.12: SLM Ti64+O microstructures for stress relieved material. Horizontal and vertical cross-section micrographs are presented for different magnifications to show different scale features of the microstructures.

Ti64+O appears to have followed a similar trend to the stress relieved Ti64, with little change in prior-β grain size between the as-built and stress relieved condition. Some of the columnar grains observed were shorter at 600 µm however columnar features longer than 1 mm were also observed. There is slight coarsening of some of the previously acicular α' martensite lathes in Figure 4.12. This would be consistent with diffusion phase change from fine α' martensite lathes, to more course lamellar α phase. The boundary region is still evident separating the horizontal equiaxed or vertical columnar prior-β grains. The visual appearance of the coarser lamellar structure is consistent with the transformation of α' to α lamellae attributed to the α stabilising properties of the oxygen addition [1, 158].

In the transformation of α' to α phase, β phase forms between the α lamellae resulting in a fine α+β structure [96, 162, 163]. XRD for the stress relieved Ti64+O in Figure 4.13 identifies a peak at approximately 67° which corresponds with titanium β phase. This is not the primary β phase peak that should be observed,

which occurs at 46°. There is no clear signal identified here however the primary α/α' peak may obscure this.

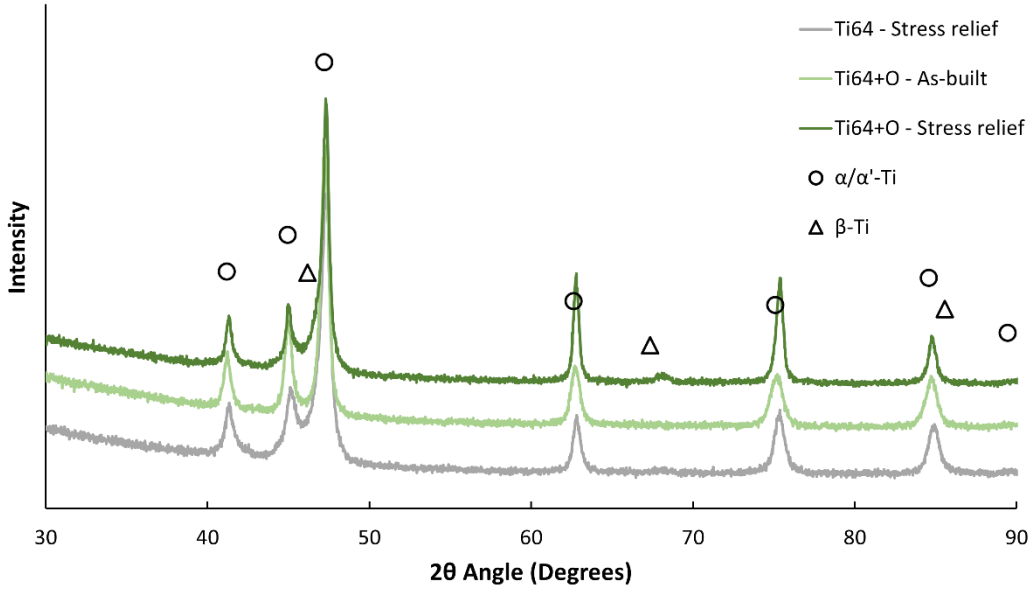

Figure 4.13: XRD pattern of SLM Ti64+O in stress relieved condition with Ti64+O and Ti64 in as-built condition for comparison. Positions of titanium α/α' and β phase reference peaks are indicated for phase identification of the measured patterns.

The presence of β phase in the stress relieved Ti64+O is unexpected as oxygen is α stabilising and should result in a reduction in β formation compared to that of the stress relieved Ti64. It is possible that the signal at 67° is an artifact of some microtextural effect or altered diffusion behaviour to enable the transformation of α' martensite into α+β phases.

Micrographs of stress relieved Ti64+B in Figure 4.14 do not appear significantly changed from those of the as-built condition in Figure 4.7. In the horizontal section, the laser scan pattern is still clearly visible as overlayed parallel paths approximately 100 μm wide. The vertical section again presented the scalloped pattern that results from the laser tracks in the layer wise build-up of SLM manufacture, as described for the as-built condition.

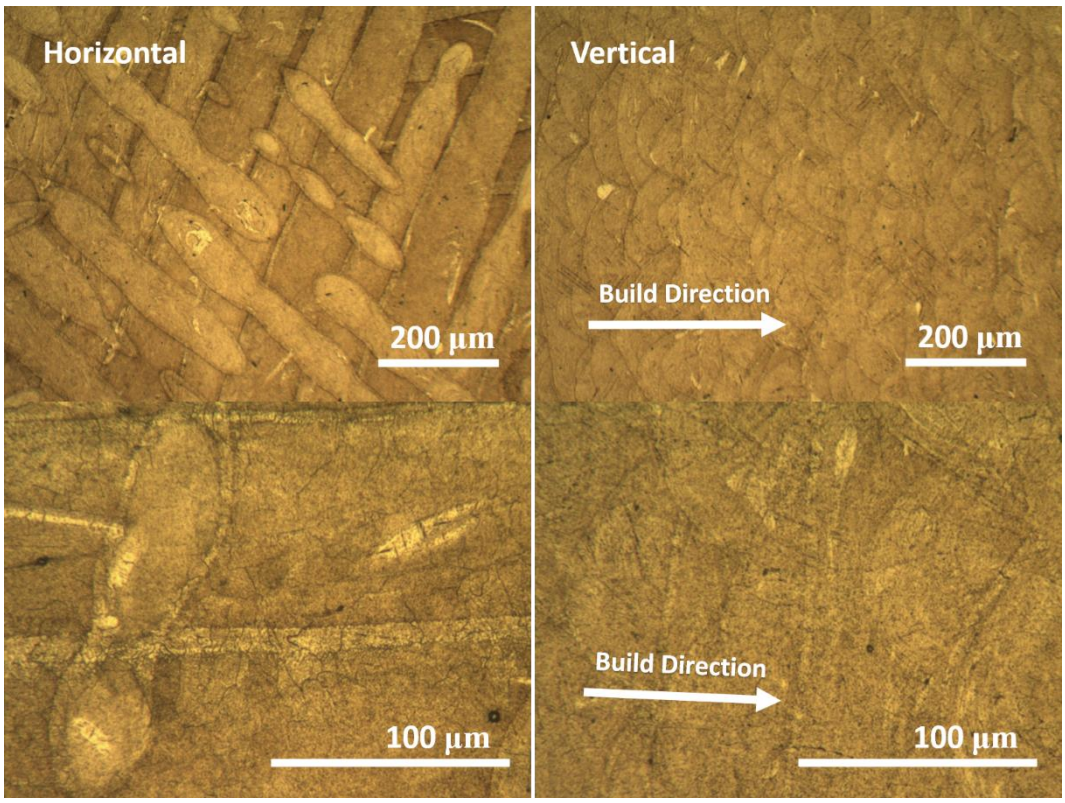

Figure 4.14: Ti64+B microstructures for stress relieved material. Horizontal and vertical cross-section micrographs are presented for different magnifications to show different scale features of the microstructures.

There is no evidence of columnar prior-β grains extending through layers in the vertical section indicating that the boron addition effectively eliminates this typical SLM microstructural feature. The difference between horizontal and vertical micrographs suggests that while the columnar prior-β grains are eliminated, there are still features of the microstructure (laser track texture) that may cause different material properties dependant on the alignment of the material..

The finer microstructure is still somewhat indistinct and obscured in Figure 4.14 so further investigation using BSD imaging in Figure 4.15 was required. A fine acicular phase is presented in the BSD micrograph with little to differentiate it from Figure 4.8 for the same boron modified material in as-built condition. Any Ti_xB_y phases are still not clear in the BSD images after stress relief.

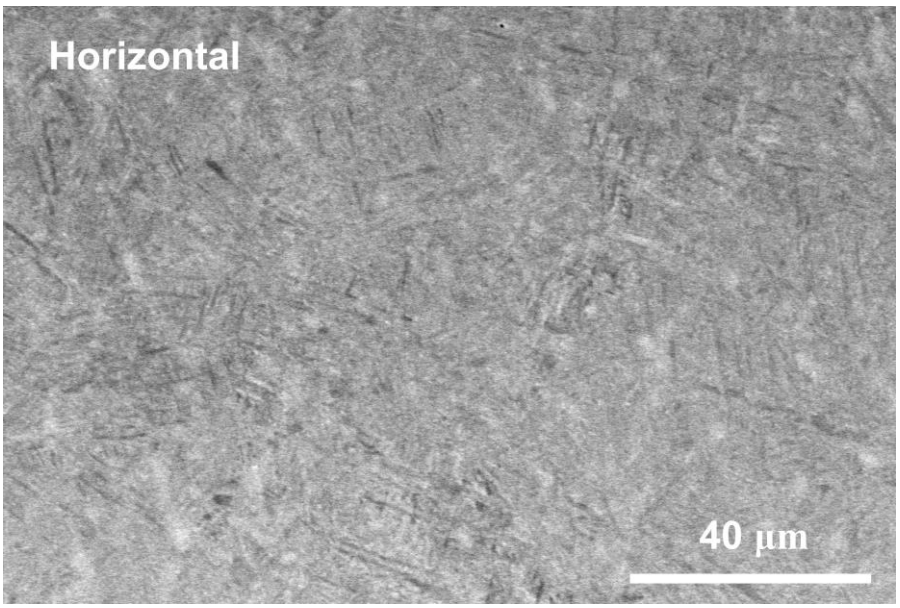

Figure 4.15: BSD image of stress relieved Ti64+B showing materials microstructure.

XRD of stress relieved Ti64+B in Figure 4.16 identifies the material as α/α' phase. No distinct peaks indicating significant β phase are present suggesting that the stress relief treatment did not alter the bulk material to a great extent. A peak is detected at 34.2° which is a significant peak for B27 orthorhombic TiB phase which does not coincide with other titanium peaks. TiB is the most stable Ti_xB_y phase in excess titanium and is well established by other research in this field [28, 33, 34, 77, 159]. The stress relief treatment has clearly enabled the formation/diffusion of detectible levels of TiB.

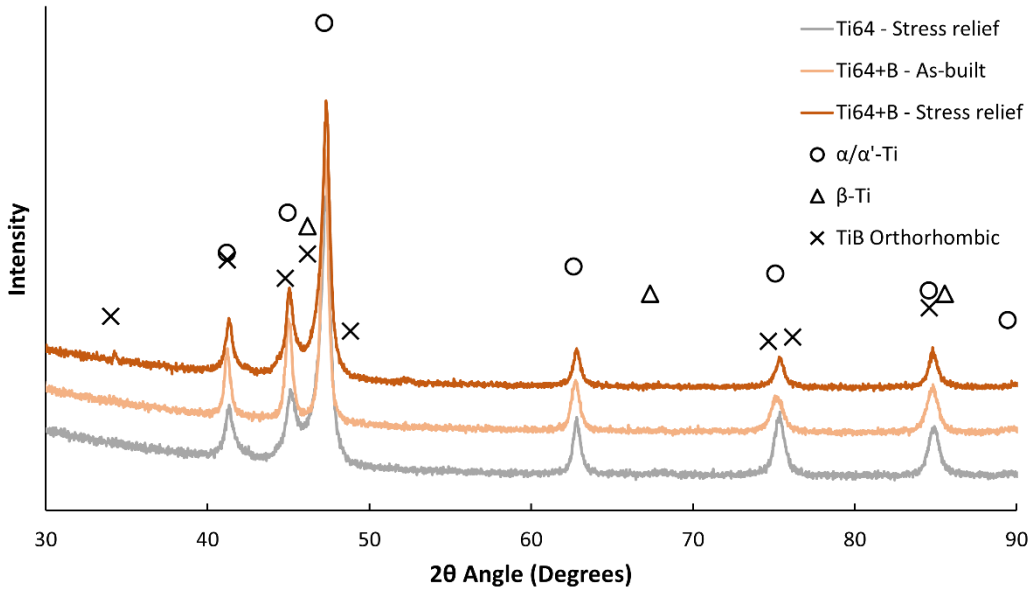

Figure 4.16: XRD pattern for SLM TI64+B in stress relieved condition compared with Ti64 in the same stress relieved condition and Ti64+B in the as-built condition. Positions of titanium α/α', β, and TiB phase reference peaks are indicated for phase identification of the measured patterns.

The diffusion and growth of TiB particles, referred to as whiskers due to their typically high aspect ratio, is observed to take place in solid state conditions such as the sintering of titanium powder [166]. Diffusion surface coatings of titanium with TiB and TiB_2 have also been shown to generate at temperatures as low as 700°C [167-169]. At the stress relief temperature of 700°C in this study the diffusion of boron and subsequent the accumulation of larger TiB particles explains the appearance of TiB phase in XRD results compared to the as-built condition.

A further signal at 52° is also evident that does not match with any compounds of Ti64, boron, and other elements present. This peak was observed in other XRD profiles of small samples and is attributed to aluminium of the sample stage in the XRD machine. This peak is not in the correct position for aluminium due to different height and alignment of the stage but from other observations in different materials it is clearly attributed to this and can be discounted.

4.2.2.1 Stress relieved microstructure summary

Stress relief treatment has had little visual effect on the overall microstructural appearance of the three materials as would be expected from this lower temperature treatment.

The overall phase of all materials has likely undergone some diffusion from α' martensite to α with some fine β phase interspaced between α lamelle. This is supported by XRD results showing some β phase for the Ti64+O stress relieved sample.

The Ti64+B material indicated that some TiB B27 orthorhombic phase was present in XRD results. This suggests that some diffusion and growth of TiB particles has occurred under stress relief to enable detection of this material.

4.2.3 Annealed microstructure.

A higher temperature annealing treatment was also investigated in this study. The temperature of this treatment was selected at 920°C to be below the β-transus of Ti64 (approx. 980°C [1]) and held for 2 hours. This annealing treatment is also comparable with the temperature cycle of commercial hot isostatic pressing (HIP), a common treatment for SLM titanium products. The intention of this treatment was to identify changes in microstructure and changes caused by added boron and oxygen that may result from typical commercial post processing of SLM Ti64.

Microstructures are presented for annealed Ti64, Ti64+O and Ti64+B in Figure 4.17, 4.19, and 4.21 respectively. Observations are made from these, followed by discussions relating any changes to phase transformation mechanisms and the influence boron and oxygen have under this thermal processing history.

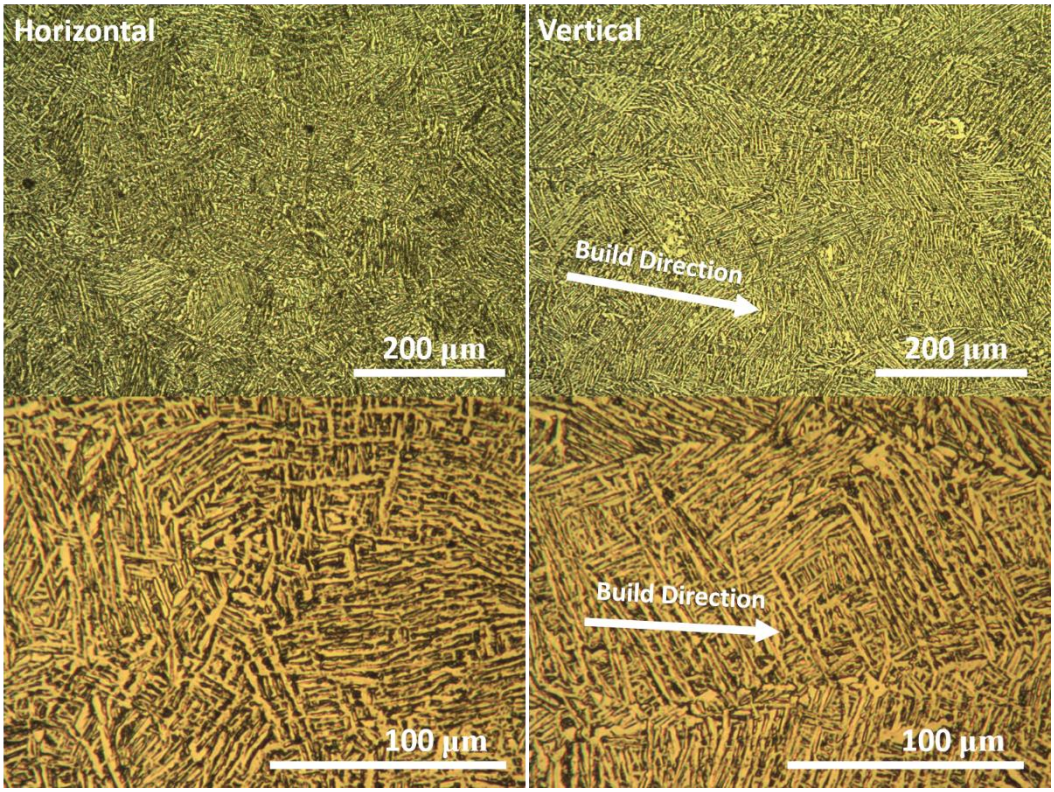

Figure 4.17: SLM Ti64 microstructures in annealed condition. Horizontal and vertical cross-section micrographs are presented for different magnifications to show different scale features of the microstructures.

Ti64 experiences significant changes after the high temperature annealing treatment. The microstructure consists of relatively coarse lamellae in both horizontal and vertical cross sections of Figure 4.17. This is significantly different to the finer acicular microstructure of the as-built condition from which it transitioned. These lamellae retain coordination within prior-β colonies where the colony size and shape are unchanged compared to the as-built material (equiaxed 100 µm in horizontal section and long columnar colonies in vertical section).

XRD of the annealed SLM Ti64 identifies phases of α/α' and a small among of β phase in the material. The development of some β phase, combined with the coarser appearance of the lamellar microstructure are consistent with expected changes to the material as a result of the annealing treatment. The treatment at 920°C has allowed the full decomposition of the as-built α' martensitic Ti64 material into a fully α+β lamellar structure following well understood behaviour with regards to heat treatments [1, 86, 100, 162, 170, 171].

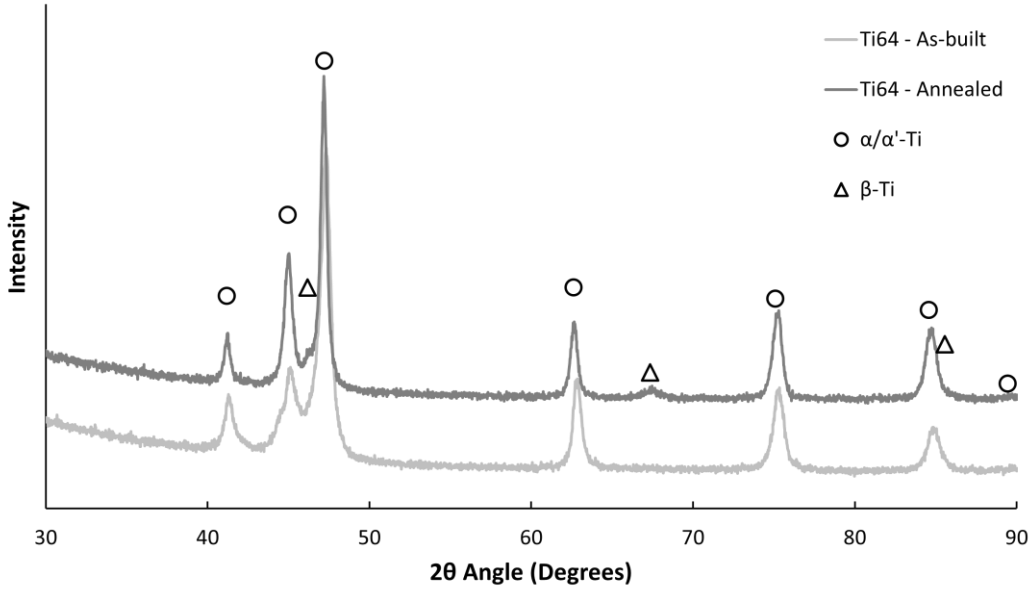

Figure 4.18: XRD pattern for SLM Ti64 in an annealed condition compared to as-built Ti64 material. Positions of titanium α/α' and β phase reference peaks are indicated for phase identification of the measured patterns.

Specifically, in SLM manufactured Ti64 the same behaviours were observed by Zhao, et al. [170] and Huang, et al. [171]. A full transformation to interspaced α and β lamellae that retain coordination within prior-β colonies with coarsening of the α phase is consistent with these results.

Ti64+O microstructures after an annealing heat treatment in Figure 4.19 behaves similarly to unmodified Ti64 with a transformation to a coarser lamellar phase and no change in the prior-β colony sizes. The boundary region around the equiaxed prior-β colonies appears to have slightly coarser lathes than within the equiaxed colonies.

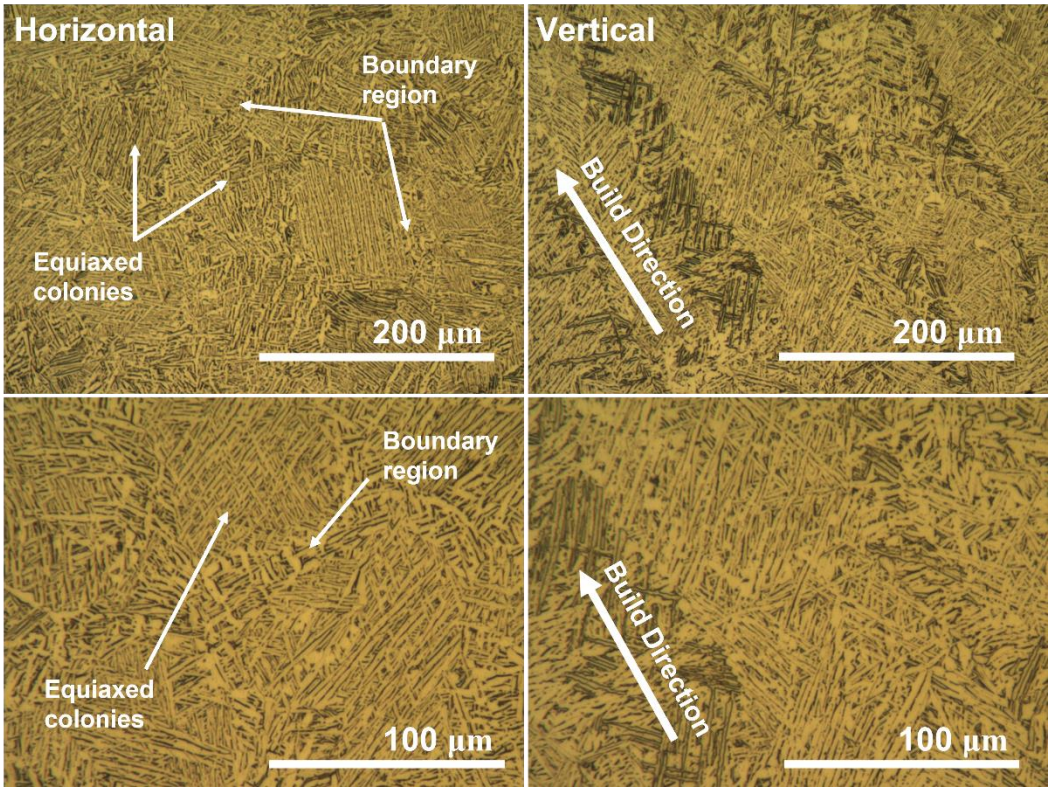

Figure 4.19: Ti64+O microstructures in annealed condition. Horizontal and vertical cross-sections of the microstructure are presented showing colony alignment that results from the build process.

These changes in microstructure suggest that all α' martensite in the as-built material has now become lamellae α+β phase with the annealing heat treatment providing sufficient time and temperature for the transformation to take place and the lamellae to become coarser. There is little difference between Ti64 and Ti64+O as they undergo an annealing treatment from the as-built condition. The only difference observed in the microstructures is the presence of the boundary region in Ti64+O, which is developed in the as-built condition and upon further heat treatment experiences equivalent effects to its structure as the rest of the material.

XRD of the annealed Ti64+O compared to Ti64 in Figure 4.20 show both materials have almost identical profiles. The material clearly consists of both α and β titanium which is in line with literature regarding heat treatment effects on SLM material [51, 170-172].

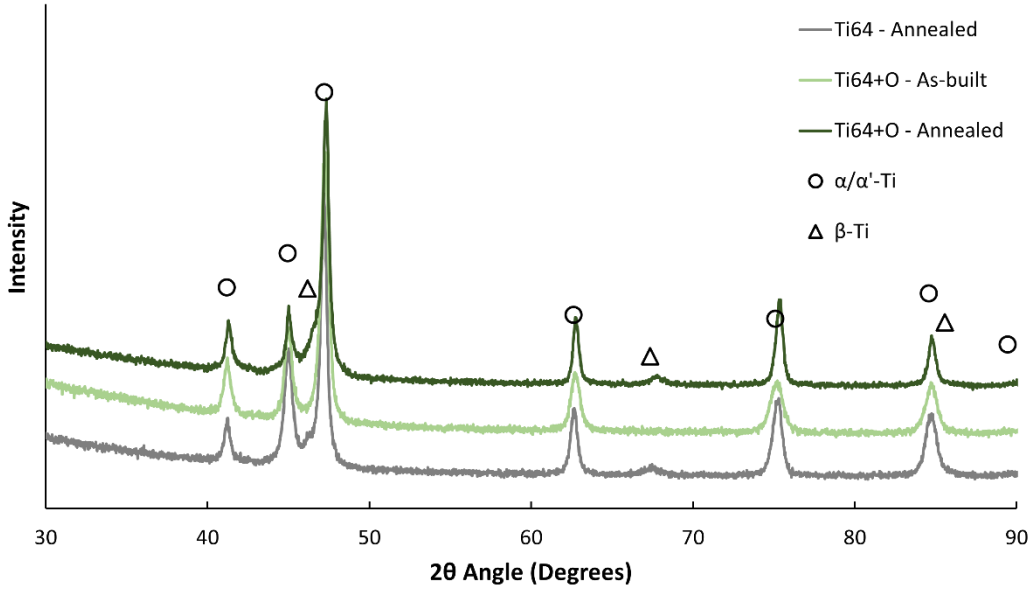

Figure 4.20: XRD pattern for SLM Ti64+O in the annealed condition. Ti64 in the annealed condition and Ti64+O in the as-built conditions are included for comparison. Positions of titanium α/α' and β phase reference peaks are indicated for phase identification of the measured patterns.

Oxygen being an α stabilising element [1], it is expected that Ti64+O may have a different proportion of α and β phases compared to Ti64 in the same condition [51]. From a visual standpoint this cannot be concluded with the lathes of both materials appearing very similar. More detailed phase investigation would be required to fully determine if this was the case.

High temperature annealing of the Ti64+B has had a significant effect on its microstructure (Figure 4.21) compared to the as-built condition (Figure 4.7). The previously obscured texture of the microstructure is now observable with a relatively fine lamellar appearance. The laser track features that were so clear in the other conditions of Ti64+B are much less obvious in the annealed condition. The edges of the laser tracks are still visible but are now identified by thin dark parallel lines (indicated in Figure 4.21).

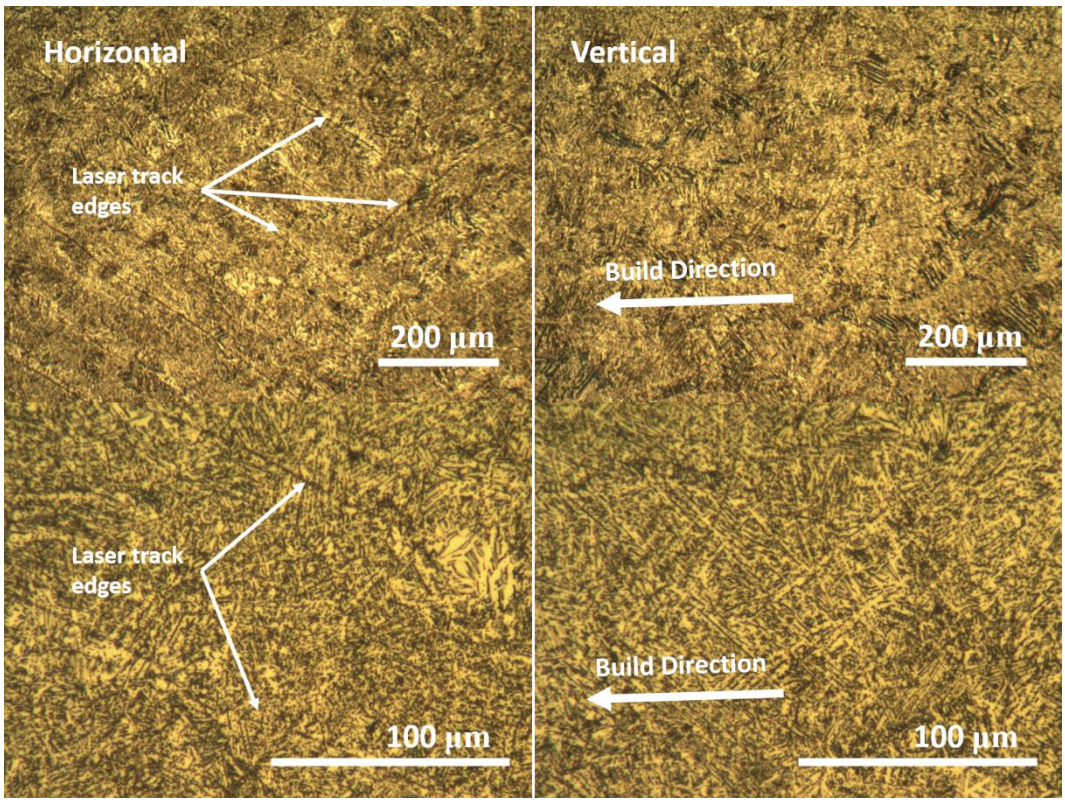

Figure 4.21: Ti64+B microstructures in annealed condition. Horizontal and vertical cross-sections of the microstructure are presented to identify directional features that results from the build process.

The fine acicular/lamellar structure visible only in BSD imaging for the as-built condition material, appears to have coarsened to give the microstructure observed here. This would be consistent with a full transformation to α+β phase with sufficient treatment time and temperature to allow some coarsening of the interspaced α and β. This behaviour is equivalent to that of both Ti64 and Ti64+O annealed materials.

BSD imaging in Figure 4.22 shows a stark difference between the as-built martensitic material and this annealed sample. The BSD images clearly shows the α+β lamellar structure with interspaced grey α phase and white β phase [1]. As with unmodified Ti64, the transformation to a coarser lamellar structure is in line with literature for this thermal treatment [100, 162, 170, 171]. The Ti64+B material has a finer lamellar structure than that developed by annealed SLM Ti64 which is consistent with the grain refining effect of the added boron [30, 40, 77, 161].

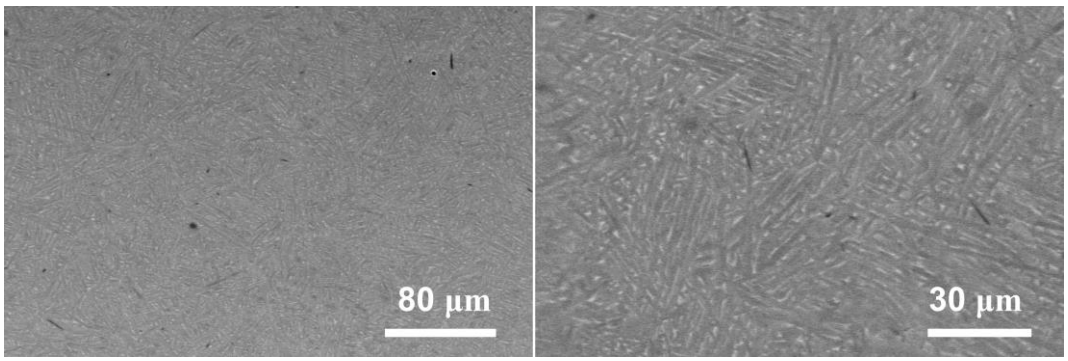

Figure 4.22: BSD images of Ti64+B in the annealed condition at 2 different magnifications showing microstructure and TiB particulates.

A new needle-like feature is also visible in the BSD cross sections, presenting as an almost black phase. These needle-like particles are expected to be TiB due to their appearance in accordance with literature [34, 173]. The annealing temperature (920°C) being greater than that of the stress relief treatment (700°C) enables greater diffusion of boron [167-169], allowing increased growth of the TiB particulates that have become visible in the BSD images.

In these BSD images (Figure 4.22) there is no distinct phase that defines the dark bands that form the edge of the laser paths as observed in the optical micrographs of Figure 4.21.

XRD identifies the phases present in the annealed Ti64+B material in Figure 4.23. As in the annealed, unmodified Ti64 there is some indication of β phase with a peak at approximately 67° with α/α' phase clearly evident. In the annealed Ti64+B there is a TiB B27 orthorhombic phase peak at 34.2°. This, along with observations of needle like particles in the material, provides evidence that TiB has formed in this modified alloy as expected.

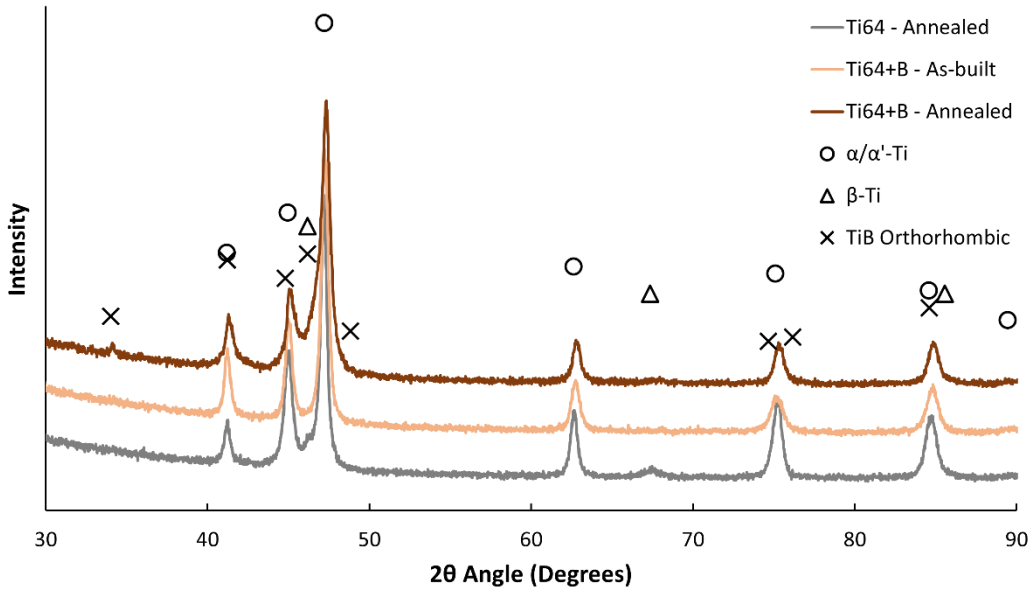

Figure 4.23: XRD of annealed Ti64+B and Ti64 along with as-built Ti64+B for comparison. Positions of titanium α/α', β, and TiB phase reference peaks are indicated for phase identification of the measured patterns.

EDS was carried out to further identify the particles and if they could be characterised as boron compounds. Table 4.1 clearly identifies the particulates consist of a high concentration of boron. The needle like appearance of these particles is consistent with studies of TiB. The needle/whisker like appearance of TiB is a result of established preferential crystallographic growth. The growth direction is parallel to [010] axis of the B27 orthorhombic unit cell of TiB [28, 34, 174]. This leads to the development of high aspect ratio, needle like particles forming. These particles have not been visually present in the other conditions of the Ti64+B material. The darker aluminium rich α phase and light vanadium rich β are also correctly identified in the EDS analysis of Table 4.1 with spectrum 1 characterising a β phase region while spectrum 3 identifies α phase.

Table 4.1: EDS elemental identification of phases and particulates in annealed Ti64+B material. EDS spectra are taken from different features that present in Figure 4.22. The results are presented in wt%.

Spectrum	B	Ti	Al	V
Spectrum 1	-	83.85	3.78	12.37
Spectrum 2	**21.26**	73.55	1.91	3.28
Spectrum 3	-	91.12	6.44	2.44
Spectrum 4	**21.81**	72.64	2.41	3.14

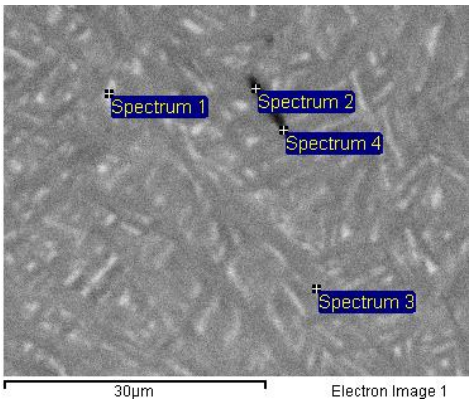

Annealed condition microstructure summary

Across all three materials, the annealing treatment has developed a fully α+β lamellar structure with relative coarsening of the lamellae. This is consistent with the higher treatment temperature enabling the diffusion transformation of α' martensite.

There is no change in prior-β colony size as the treatment temperature remained below the β-transus temperature. The large columnar prior-β colonies in the build direction remain in the Ti64 and Ti64+O materials.

This higher temperature treatment allowed further diffusion and growth of TiB particles. These were identified by phase (XRD), chemical (EDS), and visual analysis as needle like particulates in the microstructures.

Features identifying the laser tracks remained present in the optical Ti64+B microstructures. These were unresolved in BSD imaging and do not identify as concentrations of TiB particulates or a different detectible phase in the material.

4.3 Hardness

Vickers hardness of the different materials in different heat-treated states are presented in Figure 4.24. Hardness values are the combined measurements taken from horizontal and vertical cross sections of the materials. At least five measurements were taken from each sample.

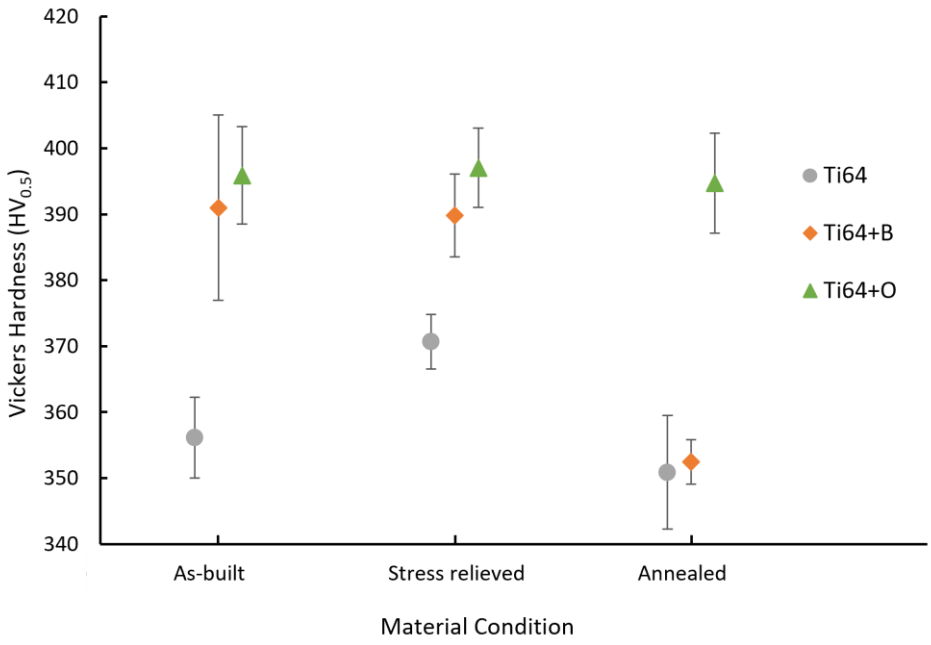

Figure 4.24: Hardness of different titanium materials with respect to their heat treatment condition. Error bars presented are 95% confidence intervals.

In the as-built condition, Ti64 has a hardness of 356±6 $HV_{0.5}$. Hardness increased to 370±4 $HV_{0.5}$ after performing the stress relief treatment, while annealed material has very similar hardness to the original as-built condition at 351±8 $HV_{0.5}$. This behaviour is expected in SLM Ti64 material and has been characterised by others working in this field [74, 162, 165, 170]. The increase in hardness after stress relief is attributed to partial decomposition of α' martensite to α phase (and potentially some β phase however this was below detection limits) while retaining the very fine lamellar structure. This microstructural change was also identified when the material in this study was characterised (Figure 4.10).

The decreased hardness of the annealed Ti64 is also explained by microstructural changes. After annealing, the microstructure of the Ti64 became coarser α+β lamellae (Figure 4.17). While the transition from metastable α' martensite is attributed to an increase in hardness, as seen in the stress relieved material,

coarser lamellae of the annealed condition result in a similar hardness to the as-built condition, as an increase in grain size causes a hardness reduction [175].

Across the different treatments, the Ti64+O material experiences very little change in hardness, remaining at approximately 395 $HV_{0.5}$, even after the annealing treatment. The increase in hardness compared to unmodified Ti64 is significant across the range of treatments. The hardening effect is attributed to the oxygen addition through interstitial solution strengthening and α phase stabilisation [176]. Oxygen forms an interstitial solid solution with titanium and subsequently strengthens the material [158, 172, 177]. Solid solution strengthening is well studied with many resources available on the subject so is not detailed here [178, 179]. Oxygen is also known to stabilise α phase and as such generates a higher proportion of the harder α phase in the material. Microstructural investigation of the Ti64+O material (Figure 4.4, 4, and 4) did not visually identify a greater proportion of α, however with more targeted analysis this would be expected, in line with other literature [51].

Annealing of the Ti64+O material did cause coarsening of the lamellar α+β phase as presented in Figure 4.19. This coarsening appears to have limited effect on the materials hardness, as there are almost no hardness differences in Ti64+O between the different heat treatments. It can be concluded that the increased oxygen content is the major contributor to the hardness difference and is effectively independent of the microstructural changes produced through heat treatment.

The Ti64+B material has a mean hardness of 390 $HV_{0.5}$ for both the as-built and stress relieved material. This is consistent with the microstructures of the material in these conditions being very similar as presented in Figure 4.7 and 4.14. As established in microstructural discussions, all boron in the material will exist as TiB particles. The addition of hard particulates can increase the hardness of a material as seen through the process of precipitation hardening [175, 180]. Hardening in this way is achieved by a distribution of very fine particulates throughout a material. These hard particles restrict slip and dislocations within the material, which results in an increase in hardness and strength. The effectiveness of

precipitation hardening depends on the size and distribution of the particulates [175].

The annealed hardness behaviour can also be associated precipitation hardening mechanisms. This heat treatment resulted in a hardness of the Ti64+B reducing to 352±4 $HV_{0.5}$. The microstructure of this material is significantly different compared to the as-built material, as described in reference to Figure 4.21. There is a coarser structure along with the development of relatively large TiB needles throughout the material. As established in the investigation of the microstructure, the development of TiB needles is due to diffusion and growth of TiB under the higher treatment temperature during annealing. Precipitation hardening is most effective with a large number of small particulates throughout the material. The diffusion and growth of TiB particulates means there must now be a smaller number of large particles in the material, having a reduced effect. This is commonly referred to as over-aging of precipitation hardened alloys [175].

The reduced effectiveness of TiB particles and coarser α+β microstructure results in the significant decrease in micro hardness observed.. The annealed micro hardness of the Ti64+B is effectively equivalent to that of the unmodified Ti64, suggesting that the added TiB in this condition has limited effect. The larger particulates may possibly improve the macro hardness of the annealed material and provide some strengthening benefit however on the macro level the effect is diminished.

4.4 Compressive Strength

Compressive properties of the different heat treatment conditions allow further understanding of the different microstructures seen in this study and the impact the additives have on mechanical properties and potential applications. Compressive tests were performed in accordance to ASTM Standard E9 [129], on cylindrical samples manufactured axially in the build direction as detailed in the methods section.

The effect of heat treatments on compressive yield strength of the various materials are presented in Figure 4.25. Across the different heat treatment

conditions all materials behaved similarly. In each condition Ti64 had the lowest yield strength and Ti64+O presented the highest, while boron modified Ti64 was between these. For each material, the stress relieved samples presented with the highest yield strength while annealing reduced yield strength compared to the as-built condition.

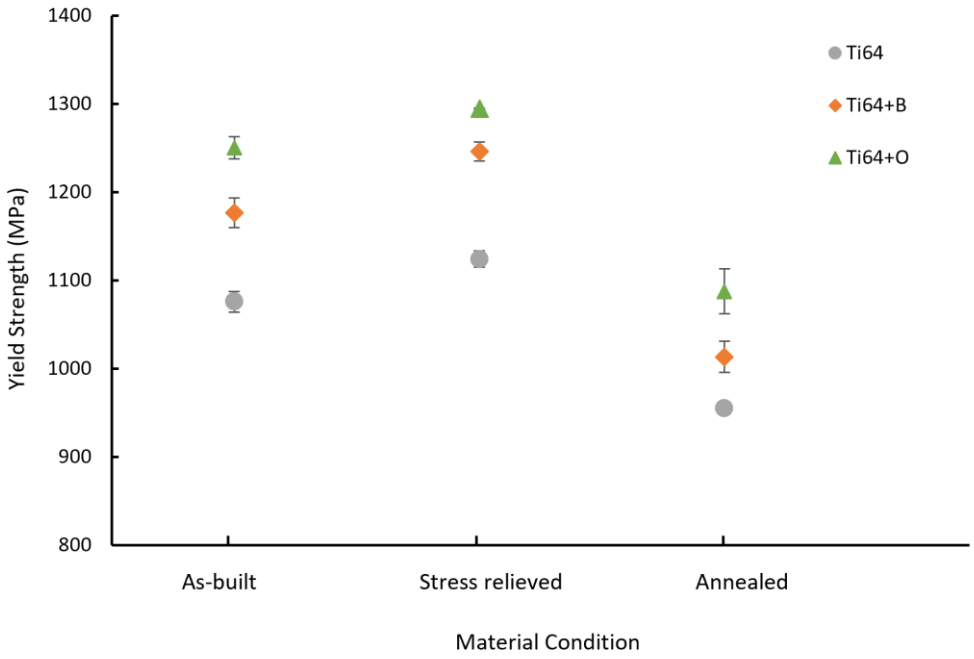

Figure 4.25: Yield strength (MPa) for the different titanium materials of this study and their heat treatment condition. Error bars represent 95% confidence intervals, some are small and obscured by the data points.

Relating the yield strength trends to observations in the materials microstructures provides supporting evidence for the observed behaviour. The stress relief treatment caused little visible change to each of the materials microstructure compared to the as-built condition, as presented by Figure 4.10, 4.12, and 4.14. It is expected that there would be little difference in the as-built and stress relieved yield strength of each of the materials. This is the case, as presented in Figure 4.25, with yield strength increasing by only approximately 50 MPa for the three different materials. This small increase in yield strength can be attributed to the stress relief treatment partially decomposing the as-built α' martensite into α phase (some β phase is likely generated but remained undetectable) as discussed in relation to XRD data and microstructure images (Figure 4.10, 4.12, and 4.14). The decomposition of α' martensite to stronger α phase, while retaining a fine grain structure results in the minor yield strength increase [162, 163].

Annealing results in a significant reduction in yield strength compared to the as-built material. Annealing also resulted in the most significant changes in microstructure for these materials presented by Figure 4.17, 4.19, and 4.21. All annealed materials were identified as α+β phase with a significant coarsening of the grain structure. While α phase is slightly stronger than α' martensite, coarser grains serve to reduce the materials strength. This is known through the Hall-Petch relationship in Equation 4.1. This defines that yield strength (σ_y) is inversely related to grain diameter (d) through the Hall-Petch equation below. σ_0 is the stress at which dislocation movement starts for a material and k_y is a material specific strengthening coefficient [175].

$$\sigma_y = \sigma_0 + \frac{k_y}{\sqrt{d}} \qquad \textbf{Equation 4.1}$$

The coarser grain structure of the annealed condition materials provides explanation for the corresponding reduction in observed yield strength. This behaviour is effectively summarised in a review of Ti64 by Liu and Shin [10].

Ti64+B has a yield strength consistently higher than Ti64 through all treatments. This can again only be due to the influence of the boron. It is clearly seen in the microstructures of Figure 4.7 (as-built), 4.14 (stress relieved), and 4.21 (annealed), that the boron has a profound influence on the prior β grain size and lamellae grain size, both being smaller than that observed in Ti64 for the same heat treatment condition. Consistent with the Hall-Petch relationship, smaller grain size results in an increase in yield strength, which corresponds to the relative increase in yield for Ti64+B.

Ti64+O has yield strengths in all conditions greater again than Ti64+B. The microstructures for Ti64+O in Figure 4.4 (as-built), 4.12 (stress relieved), and 4.19 (annealed) are very similar to those of unmodified Ti64 in the corresponding conditions with very similar appearing grain sizes and phase composition according the previously presented discussion regarding XRD. Grain structure does not explain the significant difference in strength between Ti64 and Ti64+O.

Notably, Ti64+O had a much greater hardness than Ti64 in all heat treatment conditions as presented in Figure 4.24. There are typically parallels between

hardness and yield strength of metals following an empirical relationship (Equation 4.2) between Vickers hardness (HV) and yield strength (σ_y) [181].

$$HV \approx A \cdot \sigma_y \qquad \textbf{Equation 4.2}$$

Where A is a value close to 3 for ductile materials [177, 182].

Testing this relationship, HV/σ_y values are plotted for each heat treatment condition in Figure 4.26. This empirical approximation appears to hold true for these materials and their heat treatment conditions with values varying between 3 and 3.7. When comparing each heat treatment condition, Ti64+O does not differ significantly from the other materials. This is significant as it identifies that the ratio between hardness and yield strength remains approximately the same for all materials in the same condition. The higher hardness overall for the Ti64+O is matched by a proportional increase in yield strength. The solid solution strengthening of additional oxygen is causing the increase in yield across all heat treatments of Ti64+O and a proportional increase in hardness.

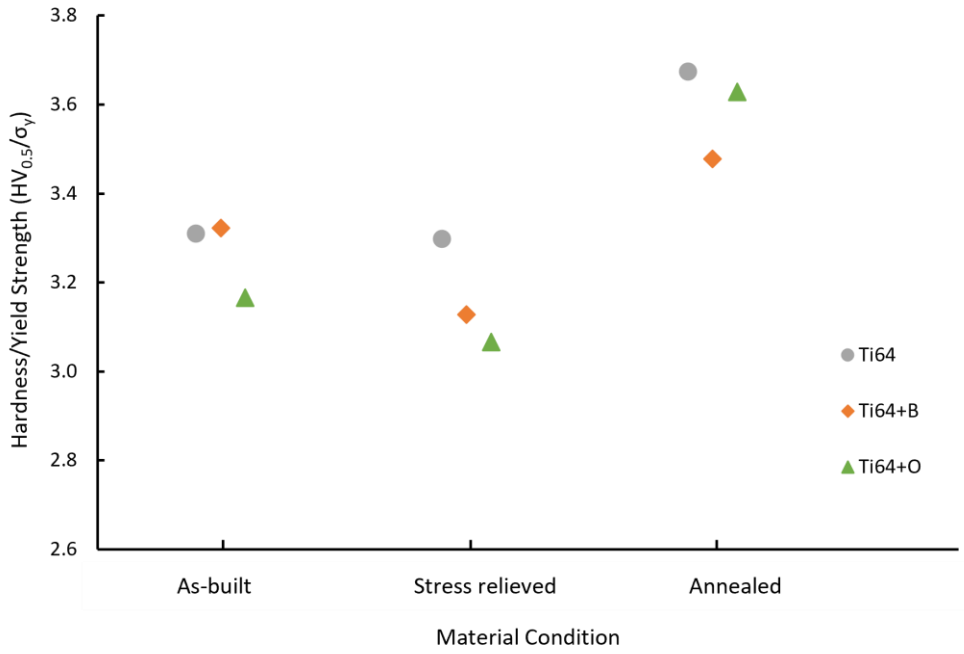

Figure 4.26: Vickers hardness over yield strength ratio compared to the different heat treatment conditions for Ti64 and modified materials of this study.

This relationship between hardness and yield strength also suggests that, in the Ti64+B materials, the increase in hardness above that of Ti64 (Figure 4.24) describes the increase in yield strength. In the annealed condition there is no

difference in hardness between Ti64 and Ti64+B while a difference in yield strength remains, which is linked with the smaller lamellar grain size. Both hardness and grain size are modified by the addition of boron and are identified as contributing to the increase in strength of Ti64+B.

From compression testing, the Young's moduli of the different materials were also compared (Figure 4.27). In the different heat treatment conditions, the relative order of stiffness of the different materials remained the same. Ti64 had the lowest Young's modulus in each condition, followed by Ti64+B, and Ti64+O presenting with the highest. Heat treatments appeared to have almost the same effect on the modulus of all materials. Stress relief increased the modulus of the materials by an average of 21 GPa while annealing caused a more modest increase of 14 GPa on average.

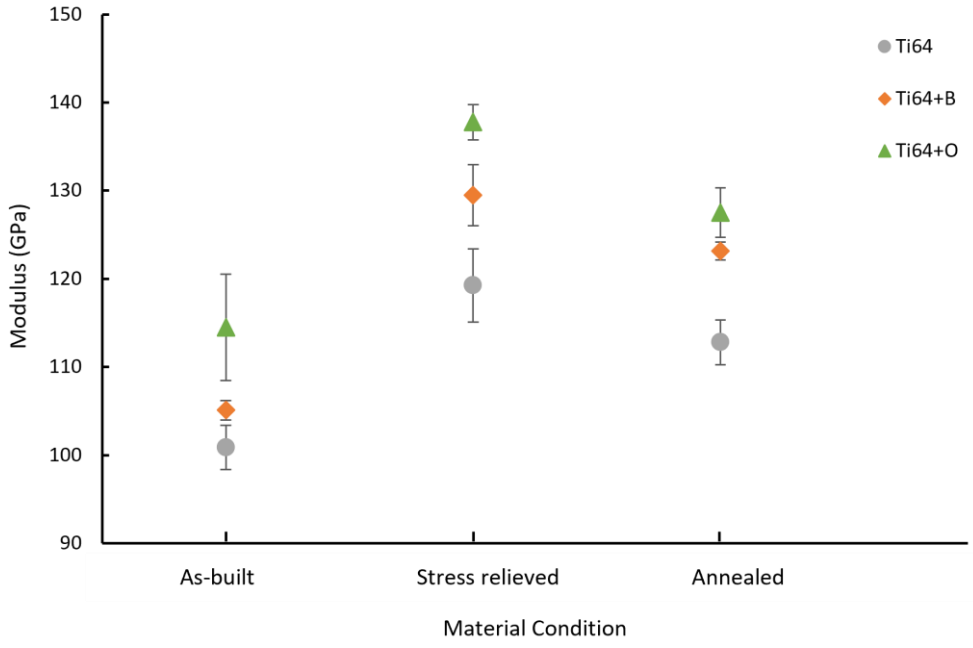

Figure 4.27: Young's modulus (GPa) for the different titanium materials of this study and their heat treatment condition.

Young's modulus is dependent on the phases and their proportion within a material. α phase Young's modulus is known to be stable however β phase modulus varies dependent on composition [183]. In α+β phase of Ti64 alloys, the modulus of α phase is reported to be 117 GPa while the β modulus is around 82 GPa with some variation based on processing and heat treatment. α' modulus is only slightly lower than α phase at 113 GPa [176, 183, 184]. The law of mixtures

directly relates the proportion and stiffness of each constituent phase to the overall stiffness of a material. The relative differences in Young's moduli of the materials can be described by the phase changes that occur through the heat treatments [185, 186]. In the as-built condition the materials were predominantly α' and as such have a Young's modulus that matches this phase. Stress relief introduced some α phase transformation so consequently the modulus increased. Following annealing the structure transformed to α+β, the resultant being a slight increase from the as-built condition however less than that of the stress relief due to the presence of a greater proportion of β phase. This general change holds true for all the materials as observed in the microstructure images.

Additional phases in the form of a composite, like the addition of TiB particulates seen in the annealed Ti64+B, adds an additional stiffening element as the Young's modulus of TiB is reported to be between 371 GPa and as high as 550 GPa compared to 117 GPa in α+β lamellar Ti64 [16, 34]. The amount of TiB present is very small so this influence would likely be minor. The boron has a significant impact on the microstructure of Ti64 with grain refinement and additional phases, which clearly has the effect of increasing the Young's modulus of the Ti64.

In the oxygen modified material the increased Young's modulus provides evidence that there is further stabilisation of α phase. This would result in more α phase present under all heat treatment conditions of the material. The resulting effect is an increasing of the modulus of this material across the range of heat treatments. Studies of oxygen content in Ti64 have seen this modulus increase through the processes of interstitial hardening and α stabilisation with an increase in oxygen content [187]. The same processes also result in a relative Young's modulus increase for additional oxygen in SLM Ti64 material.

To identify any difference between the Ti64 materials in this study and their processing, relative strain energy density during compression can be compared. Strain energy density (J/m^3) is the area under the stress-strain curve. It is hypothesised that the additives may change the plastic behaviour of the materials. Specifically, the additives may change how the materials strain harden during plastic deformation due to the concentration of boron compound particulates or

oxygen interstitials. The presence of these additives may have a disproportionate effect on dislocation motion during compression, resulting in different energy requirements for deformation. Calculating and comparing strain energy density required to compress the samples by 4% will identify material specific differences in ductile behaviour. This comparative strain energy density will increase with yield strength as this increases the area under the stress-strain curve. It will also be sensitive to changes in the plastic portion of the stress strain curve. The materials strain energy up to 4% compression is compared with yield strength in Figure 4.28.

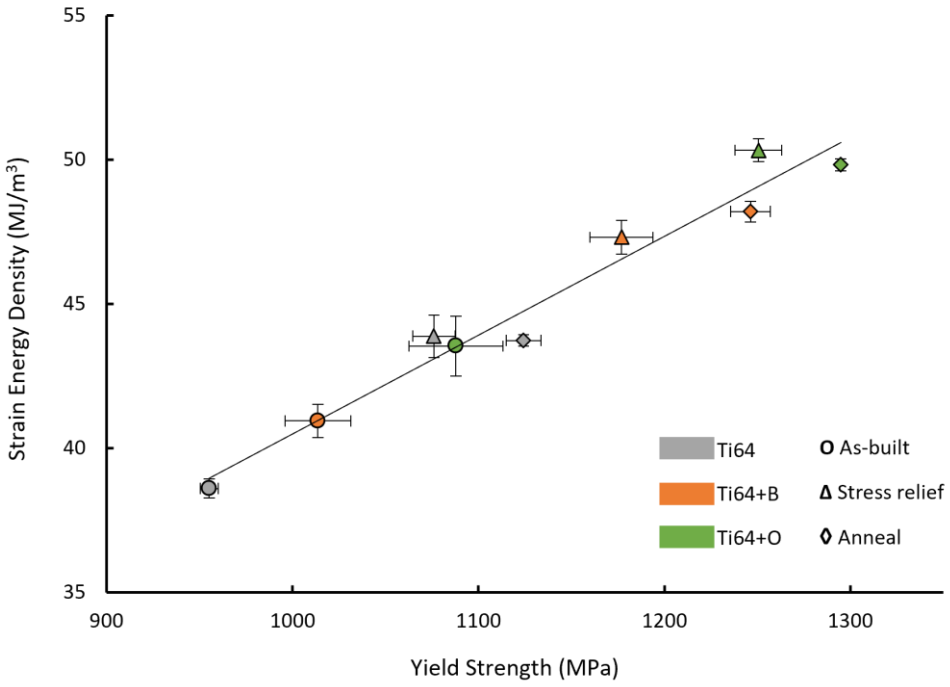

Figure 4.28: Strain energy density up to 4% compression compared with yield strength for the different Ti64 material of this study in three different heat treatment conditions. R^2 = 0.961 for the linear trend.

There is a distinct linear trend between the comparative 4% strain energy density and yield strength that correlates well with all Ti64 materials in all heat treatment conditions. This is expected, as increasing yield strength results in a greater area beneath the stress-strain curve. There is no significant variation away from this trend between the different modified materials and their heat treatment conditions. This result concludes that there is little evidence to support any significant differences in plastic deformation behaviour between the different materials aside from an increase in yield strength.

4.5 Summary

The addition of oxygen and boron have an effect on the microstructure of Ti64 and effect the response to different heat treatments. The material structure consists of prior-β colonies of fine or coarse lath/lamellar phases depending on heat treatment. Initially the materials consist fully of α' martensite. Stress relieving decomposes α' martensite into mostly α phase with little structure change, while annealing fully transforms the materials to α+β lamellar structure. Annealing also serves to coarsen the lamellar structure due to its higher temperature.

Hardness and grain/lamellar size determine the compressive yield strength of the materials with oxygen addition providing a greater hardening and strengthening effect in line with its stabilisation of α phase and interstitial reinforcement within the Ti64. Boron particulates of TiB remain fine and distributed in the as-built and stress relieved condition however annealing serves to combine these particles into much coarser needles which reduces the hardening effect on Ti64. The hardening and strengthening effect of adding boron to Ti64 is due to a combination of particulate reinforcement and grain refinement.

There is a small difference in Young's modulus in each of the materials (Ti64, Ti64+B, Ti64+O) that can be attributed to the different phases and proportions of phases in the materials.

Finally, the plastic compressive behaviour does not appear to be significantly influenced by the addition of boron or oxygen to Ti64. Any differences in comparing relative strain energy density values up to 4% strain are effectively described by differences in yield strength.

Chapter 5
Wear Characterisation

5.1 Overview

This chapter explores the wear properties of SLM Ti64 and the materials with boron and oxygen addition. Reciprocating ball on plate wear properties were investigated by pairing these materials with silicon nitride (Si_3N_4) in salt water, with the experimental described in method section 2.4.3. The wear performance of these materials is discussed regarding the characteristics of the wear tracks, current literature, and the properties of these material determined through this work.

5.2 Wear Characterisation

Ti64 is recognised as performing poorly in wear applications. This has a significant impact on the applications of this material where its other properties would present a significant advantage. These include medical devices and marine applications where titanium's other properties such as corrosion resistance have significant benefits. Any improvement in wear performance of titanium may expand the application of titanium in these fields.

Titanium wear against Si_3N_4 in salt water has been the subject of a limited amount of research. Si_3N_4 has been observed to have tribochemical interactions in salt water that have aided lubrication [188-193]. It has however, been determined that there is little evidence of enhancement through lubricious tribochemical products when wearing against titanium. Wear in these cases was dominated by standard mechanical processes of adhesion and abrasion [194].

The SLM materials of this wear study were compared with commercial Ti64 plate material. This provided an effective, commercially relevant, reference of performance for how the modified Ti64 materials and respective heat treatments compared regarding wear properties. The microstructure of the plate material consisted of α+β lamellar structure, comparable to that of the annealed Ti64

material in this study as can be seen in Figure 5.1. The lathes of α are much coarser in the plate Ti64, however they are very similar overall.

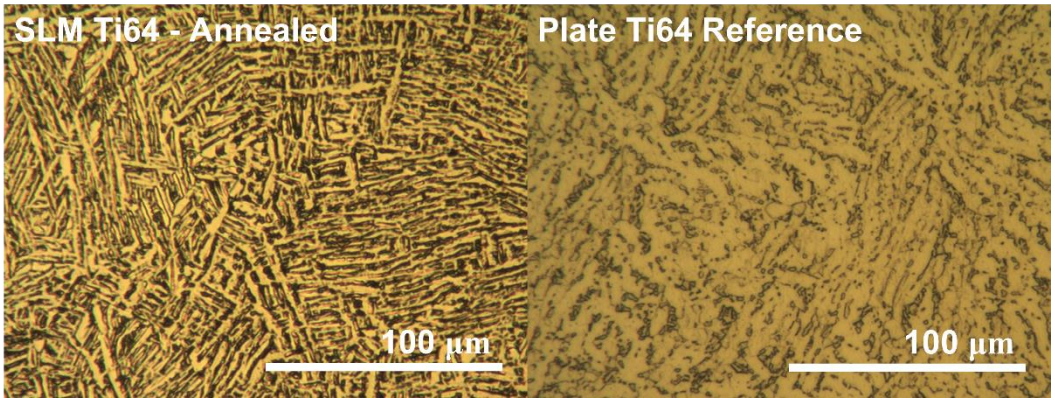

Figure 5.1: Etched microstructure images of SLM Ti64 in the annealed condition compared with commercial plate Ti64 as a reference material.

5.3 Wear Track Size and Wear Rate Analysis

5.3.1 As-built condition wear analysis

The change in cross section of the wear tracks over time in Figure 5.2 show there is a difference in behaviour between the boron modified material and other materials in their as-built condition. Ti64 and the material with additional oxygen demonstrate similar behaviour with a linear increase in wear track cross section over time. Boron differs from this with an initial larger wear track cross section. However, at the completion of the test (6 hours) there was very little difference in size of the wear tracks in the boron modified material compared to Ti64 and Ti64+O. The commercial plate Ti64 has a very similar wear performance to the as-built SLM Ti64. From a microstructure basis, the plate Ti64 is most comparable to the annealed Ti64 material, consisting of α+β lamellar structure as presented in Figure 5.1. The as-built Ti64 material is fully α' martensite as presented and discussed in section 4.2.1. This suggests there is little difference in wear performance with regards to the phase and structure of the SLM Ti64 material.

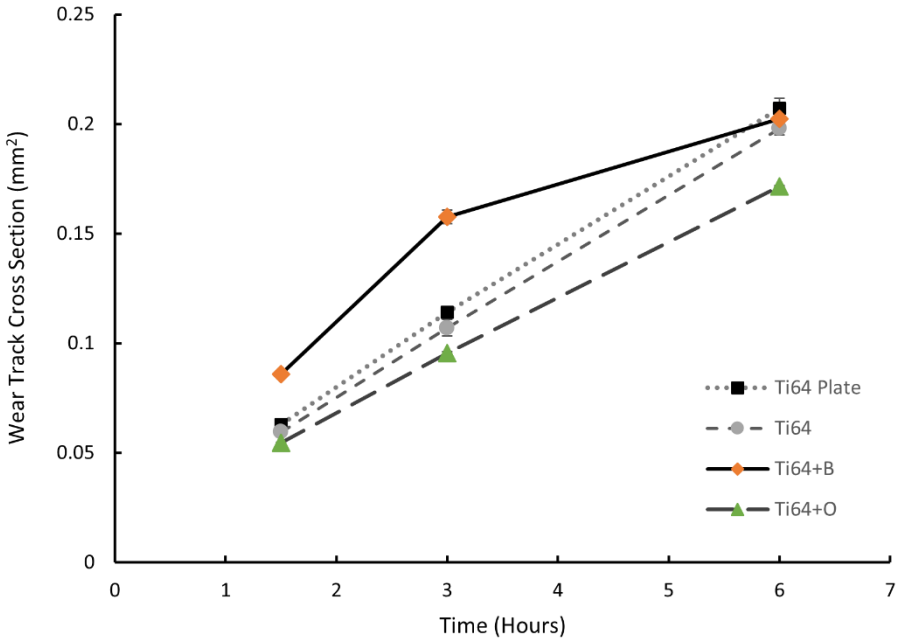

Figure 5.2: Cumulative wear track cross section area for reciprocating wear on all SLM Ti64 materials of this study in the as-built condition. 95% confidence interval error bars are included but are not obvious due to the small size.

For further comparison, the change in wear rates over the experiment are investigated in Figure 5.3. The rate of wear is determined by comparing the change in size of the wear profile cross section over each measurement interval.

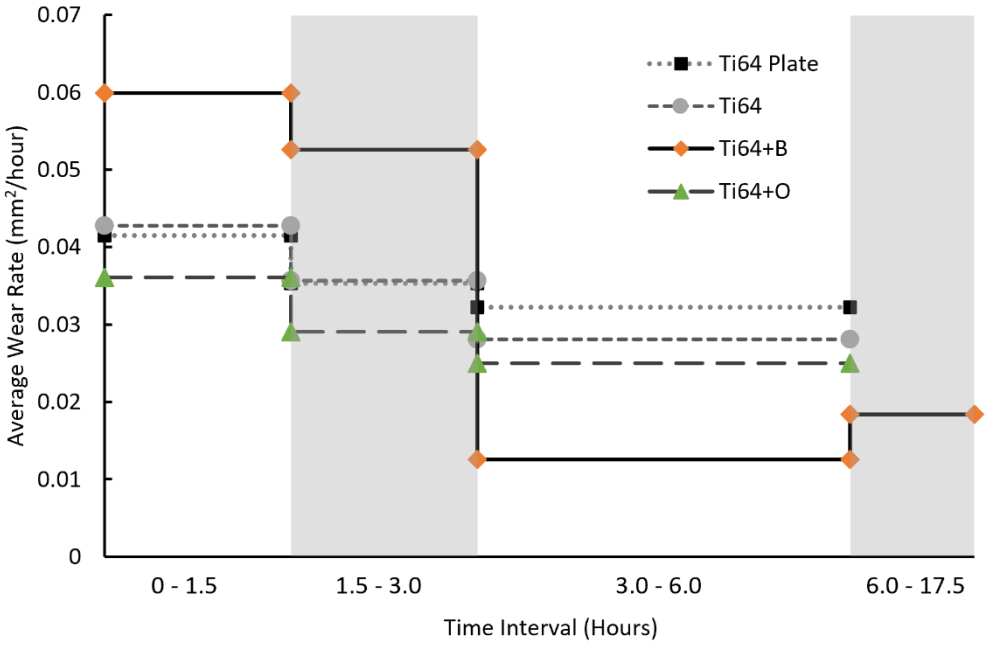

Figure 5.3: Average wear rate for the as-built materials over the different measurement time intervals of reciprocating wear. Note that the average is for the specific time interval, not a cumulative average.

It is evident that Ti64, Ti64+O, and the Ti64 plate samples have similar wear rate behaviour. Initially the wear rate starts at its highest for each of these materials. This is expected due to standard transient wear behaviour during the bedding in of the surfaces and high initial contact pressure. Following this transient period, the wear rate is shown to have decreased in the following measurement intervals with a relatively small reduction in wear rate when comparing 1.5-3 hour period and the 3-6 hour measurement. As the conditions of the test are not changing it is expected that wear will reach a steady state [195].

The boron modified material presents a somewhat different behaviour with an initial transient wear rate almost double that of the as-built Ti64. There is a modest reduction in wear rate in the intermediate time interval (1.5-3 hours). In the final interval (3-6 hours) the rate of wear has reduced significantly to the point where this material presented the lowest rate of wear of all materials in this final 3 hours of testing. This is almost a 50% reduction in wear rate compared to Ti64 during the same wear interval. This response is significant with high confidence as the test was performed in triplicate on different samples with little difference in behaviour, as demonstrated by the very small 95% confidence interval error bars presented in Figure 5.2.

To further identify if this result for as-built Ti64+B was not in error and that steady state wear had been achieved a further extended test was conducted to identify the long-term wear rate. After 3 hours the wear rate of the Ti64+B remains below 0.02 mm^2/hour as shown in Figure 5.3. This test identified that the wear rate remained low compared to the minimum wear rate observed after 6 hours for the other materials in the as-built condition.

5.3.2 Stress relieved condition wear analysis

After stress relief heat treatment, the wear performance of all materials was very similar, as presented in Figure 5.4. The Ti64, Ti64+O, and Ti64+B samples had almost identical wear track cross sectional area over the test period of 0.17 mm^2 after 6 hours. This was a slight reduction for Ti64 compared to the as-built condition where the wear track cross section was 0.2 mm^2 after 6 hours.

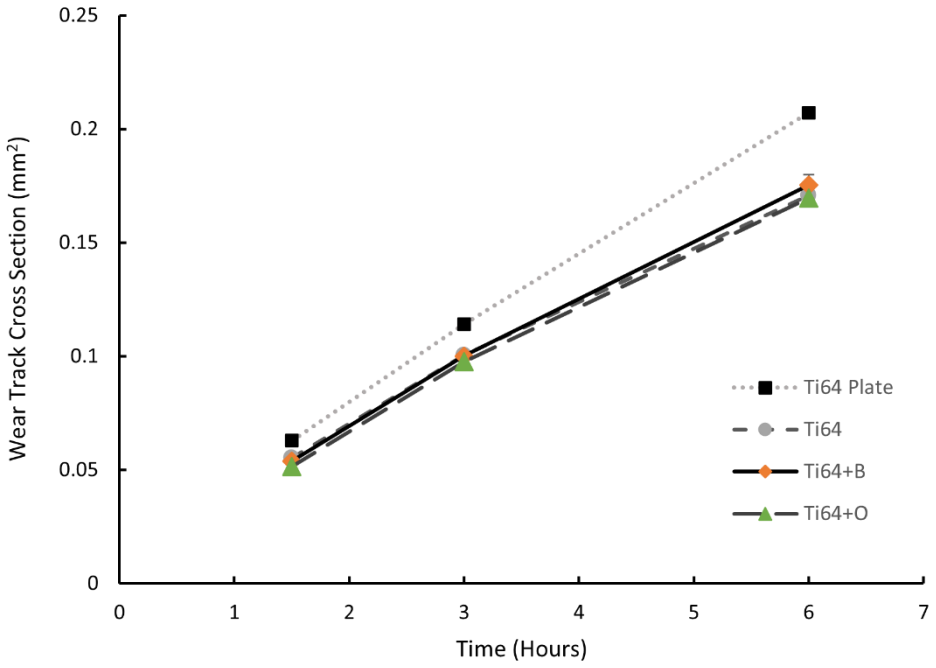

Figure 5.4: Cumulative wear track cross section area for reciprocating wear on all SLM Ti64 materials of this study in the stress relieved condition. 95% confidence interval error bars are included but are not obvious due to the small size.

The wear track size of stress relieved Ti64+O in Figure 5.4 was practically identical to the as-built condition (Figure 5.2) while the stress relieved boron modified material is significantly different. The stress relieved Ti64+B wear cross section matches identically with that of Ti64 and Ti64+O over the duration of the test, in contrast to the behaviour observed in the as-built Ti64+B material. Wear rates of the stress relieved materials in Figure 5.5 highlight this difference when compared to the as-built condition wear rates of Figure 5.3.

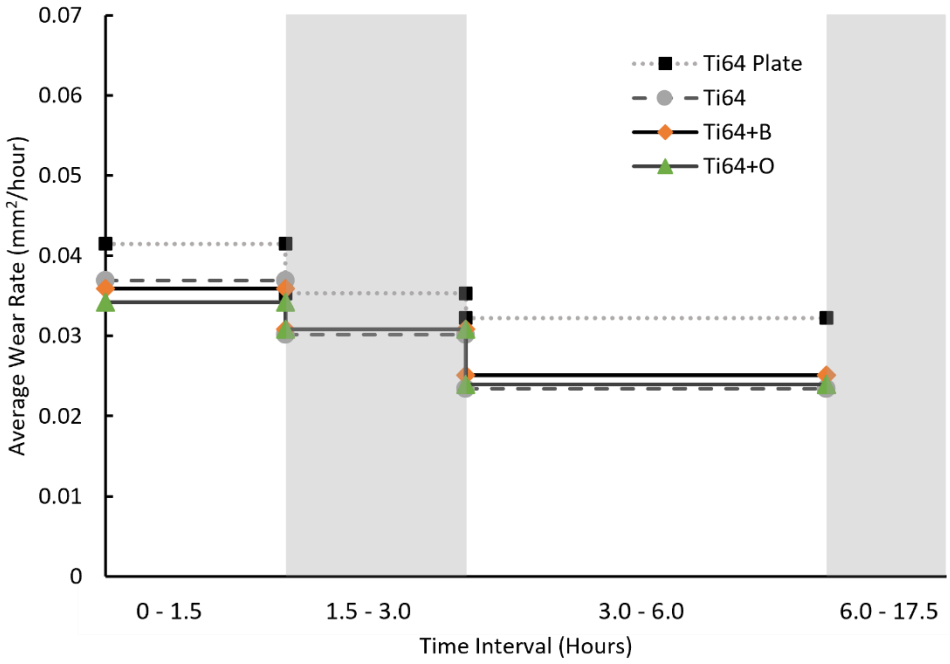

Figure 5.5: Average wear rate for the stress relieved materials over the different measurement time intervals of reciprocating wear. Note that the average is for the specific time interval, not a cumulative average.

The wear rates of the stress relieved materials are all equivalent over the duration of the reciprocating wear test. In Ti64+B the process of stress relief appears to have eliminated the initial high transient wear of the as-built material seen in Figure 5.3.

Stress relief was observed to have little effect on the microstructure of Ti64+B, and only minor changes in hardness and compressive yield strength as determined in the previous chapter (Section 4.2.2). The change in wear behaviour of the boron modified material from the as-built condition to stress relieved condition is therefore unexplained by differences in microstructure or measured mechanical properties.

Further investigation of the wear tracks will be carried out later in this chapter to determine if there has been an obvious wear mechanism change that may be responsible for different transient wear performance.

The wear performance of all SLM printed and stress-relieved materials was only slightly better than that of the reference Ti64 plate. From these results it is evident

that the additives of oxygen and boron have had little impact on the absolute wear performance of the Ti64.

5.3.3 Annealed condition wear analysis

In the boron modified material, TiB particulates were observed in the annealed material as presented in Figure 4.21 in section 4.2.3. Particulate reinforcement has been seen to have an impact on wear properties in titanium when a greater amount of particulate reinforcement is used [123, 196, 197]. To investigate if a small concentration of TiB particulate had any effect on wear performance under the conditions of this test a further investigation was carried out on the annealed boron containing sample and compared to the commercial Ti64 plate reference.

Testing of wear performance in the annealed condition was limited to the Ti64+B material due to difficulty accessing equipment. It is also justified by the as-built and stress relieved conditions of Ti64 and Ti64+O having almost identical wear performance (Figure 5.2 and 5.4) and being very comparable to the Ti64 plate reference. Given that the Ti64 plate reference microstructure (Figure 5.1) is analogous to the annealed microstructures of Ti64 and Ti64+O characterised in section 4.2.3 (α+β lamellar colonies), results suggest that the microstructure and phase of Ti64 materials have little impact on the wear properties of the material under these reciprocating wear conditions.

It was decided that the most significant insights could be gained by investigating only the Ti64+B in the annealed condition to determine the impact of the larger TiB particulates that were observed within the microstructure in this condition.

Figure 5.6 clearly demonstrates there is very little difference in wear performance between the annealed Ti64+B and the stress relieved material condition. Further comparing with Figure 5.2 and 5.4 it can be seen that only Ti64+B in the as-built condition presented with different wear properties.

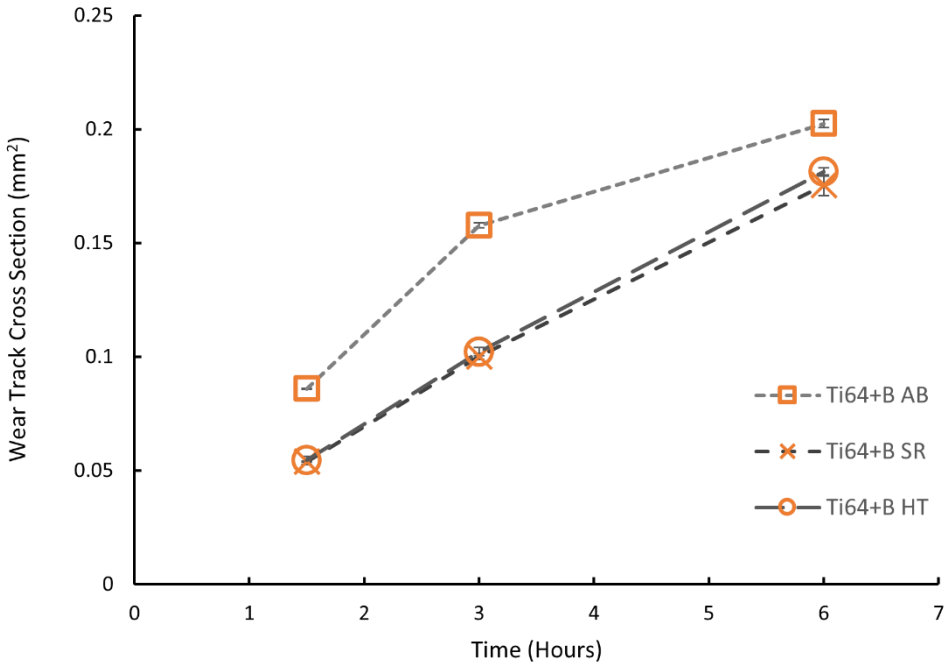

Figure 5.6: Wear track cross-sectional area for Ti64+B in different heat treatment conditions. AB=as-built, SR=stress relieved, HT=annealed.

The behaviour of the Ti64+B in the annealed condition also supports the justification for not conducting wear testing the other materials in their annealed condition. The annealed Ti64+B and Ti64 plate materials both present similar behaviour and support the evidence that wear performance is not significantly dependent on the materials microstructure.

The appearance of larger TiB particulates in the annealed condition Ti64+B has no impact on size and rate of wear track generated in these test conditions. Wear resistance improvement via particulate inclusion has been determined to be dependent on the fraction of particulate material with a greater proportion typically reducing the wear rate [197-199]; the small fraction of TiB in the Ti64+B material would therefore have a limited effect. Study of the wear surfaces may present different features with regards to TiB particulates being present and can determine if there has been a change in wear mechanism to further understand the materials wear behaviour.

5.4 Wear Track Observations

The type of wear and performance of a material can be understood through analysis of resulting wear tracks. Different wear mechanisms will present different damage to the wearing surfaces. These can be characterised by identifying: tearing, parallel track scoring, presence of wear debris, or appearance of fracture as just a few examples [195].

In this study wear is taking place between titanium materials against silicon nitride in saltwater solution. Studies on the tribochemical and corrosive wear on titanium have found that water and salt water have minimal effect on the wear behaviour [200]. The impact salt water has on Ti64 wear is attributed to some lubrication and cooling of the wear surface as adhesive and abrasive processes break the protective oxide film, which continues to reform and be removed. There is little synergistic influence of corrosion and wear taking place that stand out with regards to the standard poor wear performance of titanium [201-203].

The commercial Ti64 plate wear behaviour presented in Figure 5.7 shows typical titanium wear features. There is significant plastic damage as indicated by the parallel scoring of the surface. This is indicative of abrasive wear processes. In the case of titanium, oxides are removed from the surfaces and act as third body abrasive particles in the wearing interface which further increases the damage [204]. The dark pockmarks/speckling of the wear tracks are difficult to resolve at low magnification. Higher magnification in Figure 5.8 reveals this as tearing of the surface as the material breaks down under wear. This is a feature of adhesive wear processes that are common in the wear of titanium alloys [195, 204]. Particles can also be identified in the wear surface at higher magnification, as indicated in Figure 5.8, which are likely to be oxides.

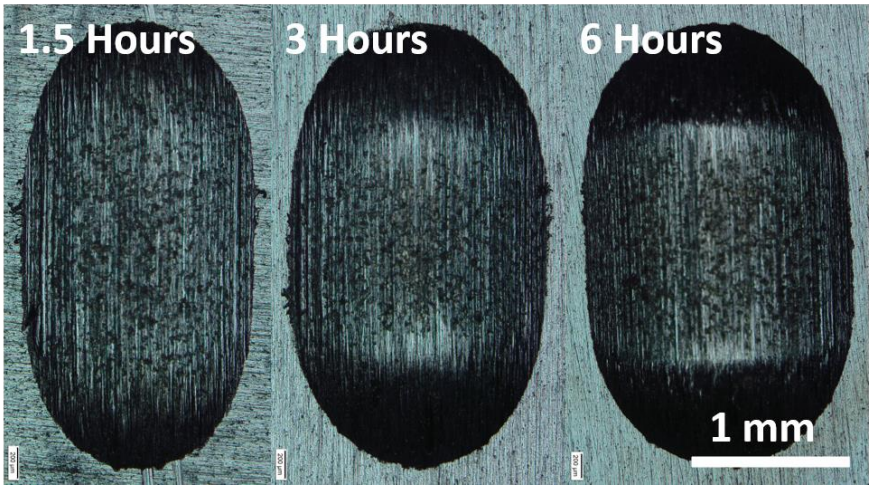

Figure 5.7: Commercial Ti64 plate wear tracks after different lengths of time wearing against Si_3N_4 in salt water.

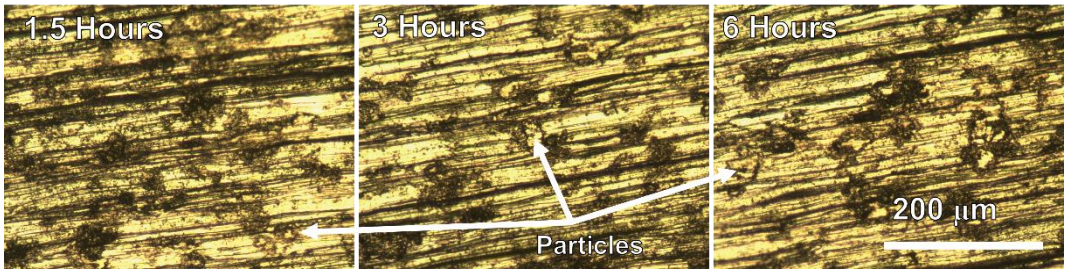

Figure 5.8: Higher magnification of commercial Plate Ti64 wear tracks after different lengths of time wearing against Si_3N_4 in salt water.

Figure 5.9 presents the Si_3N_4 bearing counterbody after 3 hours of wear on the commercial Ti64 plate and that of the Si_3N_4 bearing after only a few cycles of wear on a hardened steel substrate to act as a "clean" reference surface. There is clear evidence of a transfer of titanium metal to the surface of the bearing through the different appearance of the contact region compared to the "clean" worn bearing. This transfer of metal supports the conclusion that an adhesive wear mechanism is taking place in this wear pairing. Titanium is highly reactive and with the subsequent breakdown of its surface oxide film, it will readily react with further materials under the right conditions. Titanium may react with both silicon and nitrogen in the counterbody. This is evident in the breakdown of Si_3N_4 in experiments investigating its use as a reinforcement of titanium [205]. The flash temperature at the contact points in the wear surface may provide the conditions to generate this reaction. Through this process, reaction leading to adhesive wear could take place and generate the metal transfer film observed. The wear process then partially becomes a titanium-titanium interface with debris particles removed from both surfaces to exaggerate scoring, smearing, and tearing.

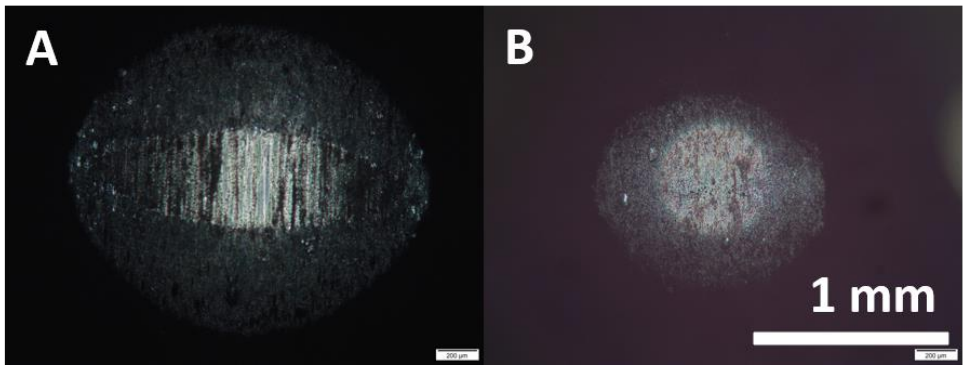

Figure 5.9: Si_3N_4 bearing wear contact surfaces. A) After wear against commercial Ti64 plate for 3 hours. B) Reference surface after contact with hardened steel for only a few cycles.

The SLM manufactured Ti64 (Figure 5.10) and boron modified Ti64 (Figure 5.11) in the as-built condition present the same mechanisms of wear when compared to the commercial plate material (Figure 5.7). The same plastic scoring of the surface is present with similar speckling indicative of smearing and tearing. The Si_3N_4 bearing surfaces were also identified to have a transfer film of titanium (evident later in Figure 5.16).

There are few observable differences between the as-built Ti64 and Ti64+B materials, limiting the ability to differentiate the materials in order to help understand the processes that result in high initial wear of the boron modified material. After 3 hours of wear the Ti64 material approaches approximately steady state wear while the boron modified Ti64 was still suffering from a high wear rate (identified in Figure 5.3). The differences between the tracks at 3 hours show more of the dark pockmarks/speckling in the boron sample. In higher magnification images (Figure 5.12). Particles are present in the wear surface of the boron modified material, as they were in the unmodified Ti64. It is noted that there is little difference in appearance of these torn regions or the nature of the wear damage occurring. After 6 hours of wear, the tracks of both materials appear very similar with regards to the amount of speckling and parallel scoring. Differences are difficult to resolve in optical micrographs and as such there is little conclusive evidence in these track images that explain why the boron might have a reduced wear rate compared to Ti64 after 6 hours.

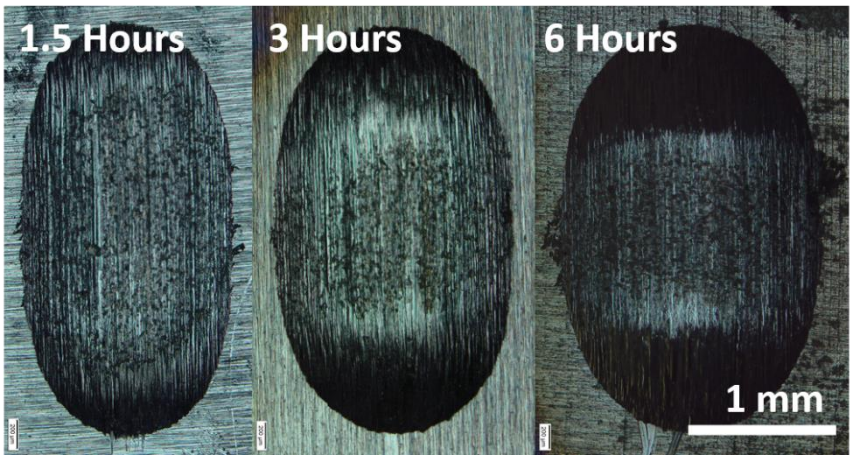

Figure 5.10: Wear tracks of SLM Ti64 in the as-built condition after different lengths of time wearing against Si_3N_4 in salt water.

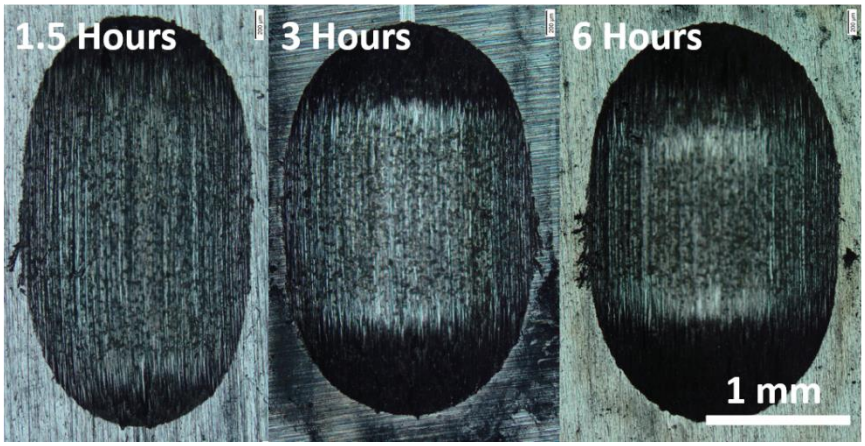

Figure 5.11: Wear tracks of SLM Ti64+B in the as-built condition after different lengths of time wearing against Si_3N_4 in salt water.

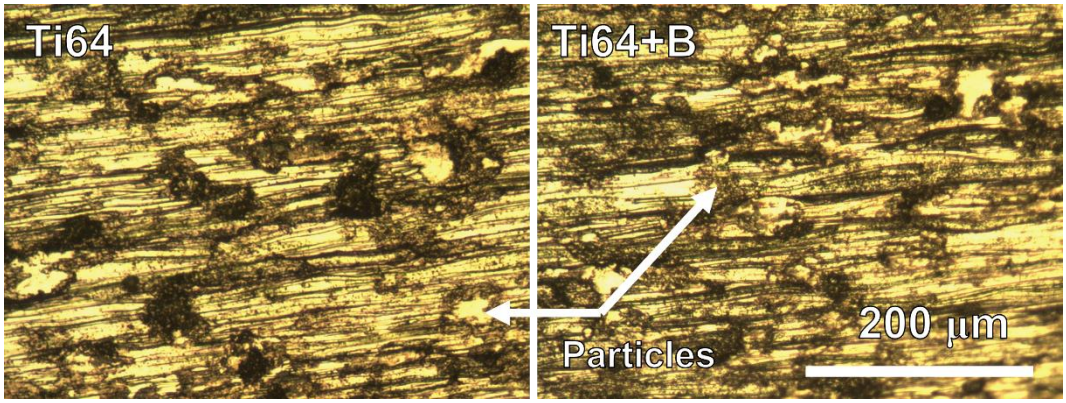

Figure 5.12: Higher magnification images of the wear tracks of as-built Ti64 and Ti64+B after 3 hours of wear.

SEM imaging of the wear damage (Figure 5.13) provides a more detailed image of the wear damage. This indicates there is more tearing of the boron containing material with more breaks in the parallel abrasion furrows and rougher edges on these breaks. This is caused by adhesive wear processes with the counterbody via

possible reactions with the Si_3N_4 and the metal transfer film. The increase in breaks may be due to the boron content raising the hardness of the material and Ti+B compounds causing an increase in tearing of the materials rather than the more furrowed appearance in the Ti64 surface. An increase of this in the boron modified material would be consistent with an increase in material removal and the subsequent high wear rate. The SEM images of Figure 5.13 show fine particulates of wear debris throughout both materials. These are the result of the breakdown of the material under wear conditions and lead to the scoring of the surface. This debris acts as a third body in the wearing interface and further works to abrade the material [195].

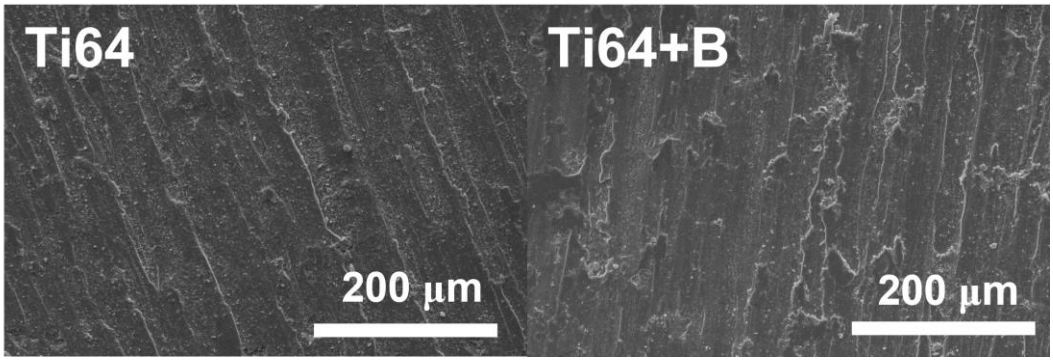

Figure 5.13: SEM images of the wear tracks of as-built Ti64 and Ti64+B after 3 hours of wear.

The wear tracks for the as-built oxygen modified material in Figure 5.14 are very similar to the as-built Ti64 (Figure 5.10) across the different test periods. The same scoring and speckling features of abrasive wear, adhesion and tearing are present. This appearance is consistent with the similar wear rates between the Ti64 and oxygen modified material (Figure 5.3).

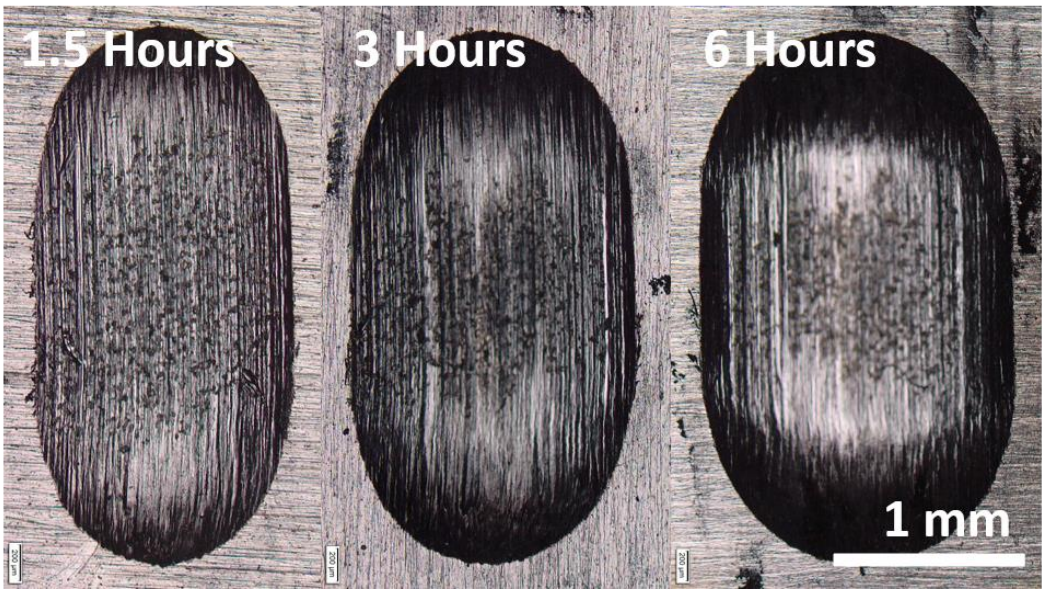

Figure 5.14: Wear tracks of SLM Ti64+O in the as-built condition after different lengths of time wearing against Si_3N_4 in salt water.

After stress relief the materials all had very similar wear behaviour over the total duration of the tests (Figure 5.4 and 5.5). The wear tracks for all materials (Figure 5.15) have a similar appearance that is indicative of the wear mechanisms of abrasion, adhesion, and tearing. The Ti64 and Ti64+B appear almost identical however the Ti64+O material appears to have less dark speckling (visually linked to adhesion and tearing in SEM images in Figure 5.13). The features of the corresponding worn Si_3N_4 counterbodies (Figure 5.16) appear to show some relation to the different behaviour from the oxygen enriched titanium. There appears to be less metal transferred to the surface of the counterbody. This suggests that oxygen addition is resulting in a slight change in how the material is worn. There is less tendency for adhesive tearing and formation of the transferred metal film. This does not appear to impact the wear performance of the material overall as no difference in comparative material removal is identified (Figure 5.4).

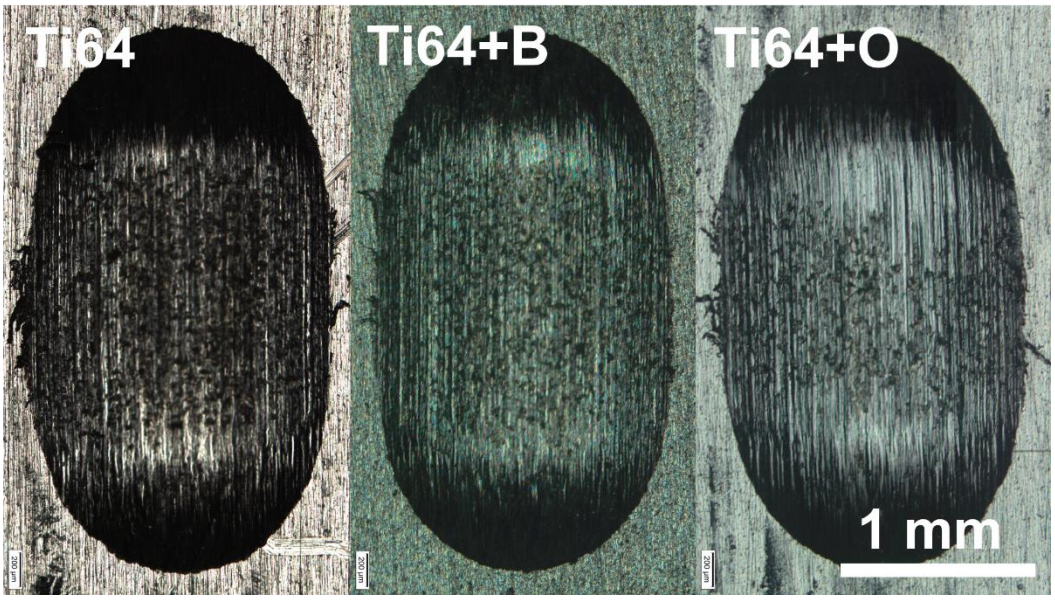

Figure 5.15: Wear tracks of stress relieved titanium materials after 3 hours against Si_3N_4 in salt water.

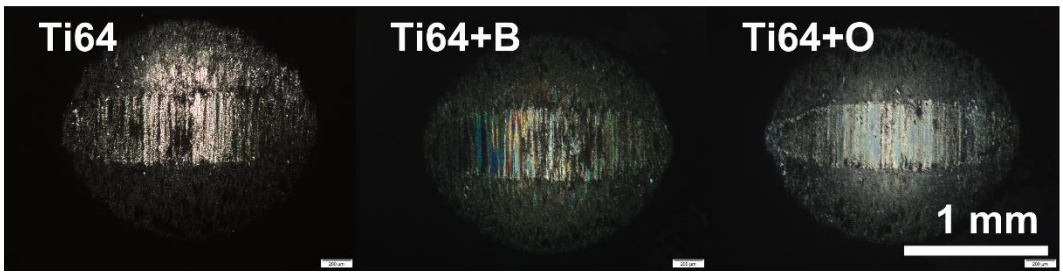

Figure 5.16: Si_3N_4 wear counterbody after 3 hours against the different titanium materials in salt water.

The wear surfaces of the annealed boron modified titanium in Figure 5.17 showed no visual difference compared to the same stress relieved material (Figure 5.15). This corresponds to the similar wear performance of these materials and supports the earlier conclusion that the low level of boron has little effect on wear properties.

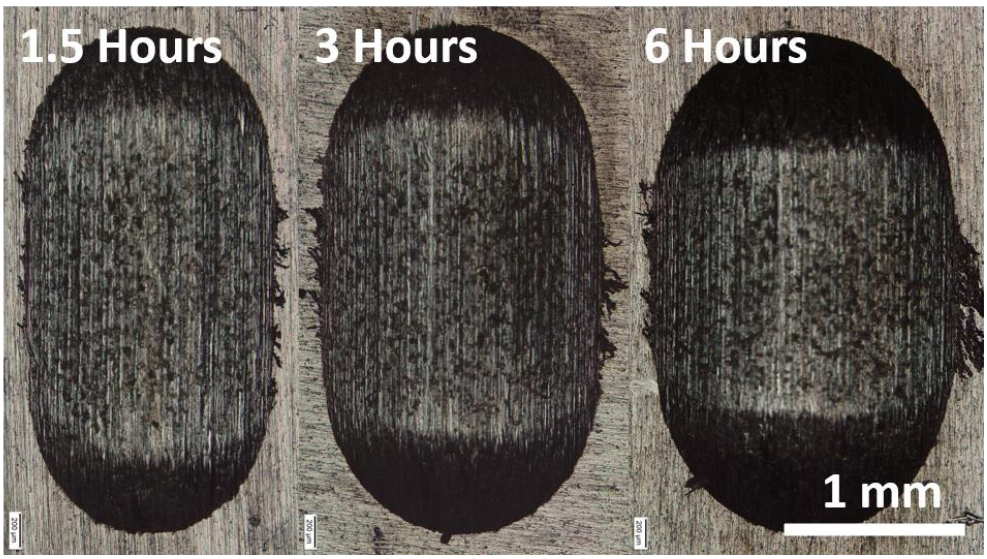

Figure 5.17: Wear tracks of SLM Ti64+B in the annealed condition after different lengths of time wearing against Si_3N_4 in salt water.

Overall, through heat treatments and small additions of boron and oxygen, the wear mechanisms of Ti64 appear to remain the same in this system. Abrasion and adhesive wear processes are both active.

The impact of the Si_3N_4 counterbody has not been quantified through this work. There is clearly an interaction between this wearing pair under salt water as is evident by the metal transfer film being established. Further investigation of friction coefficients and wear chemistry may lead to better characterisation of this impact however these are not covered here.

5.5 Wear and Hardness Correlations

Wear is recognised as being related to hardness for many metals [206] with an increase in wear resistance that corresponds with increased hardness. This is a general case and other factors such as toughness and tribochemical interactions can be more significant factors [195, 207-209]. Comparing the hardness with wear performance of the materials in this investigation it can be seen in Figure 5.18 that there is an apparent linear relationship between wear and hardness, with increasing hardness resulting in a reduction in wear damage. The as-built Ti64+B material is the only material that appears to break significantly from this relationship with much higher than expected wear with respect to average hardness after 1.5 and 3 hours.

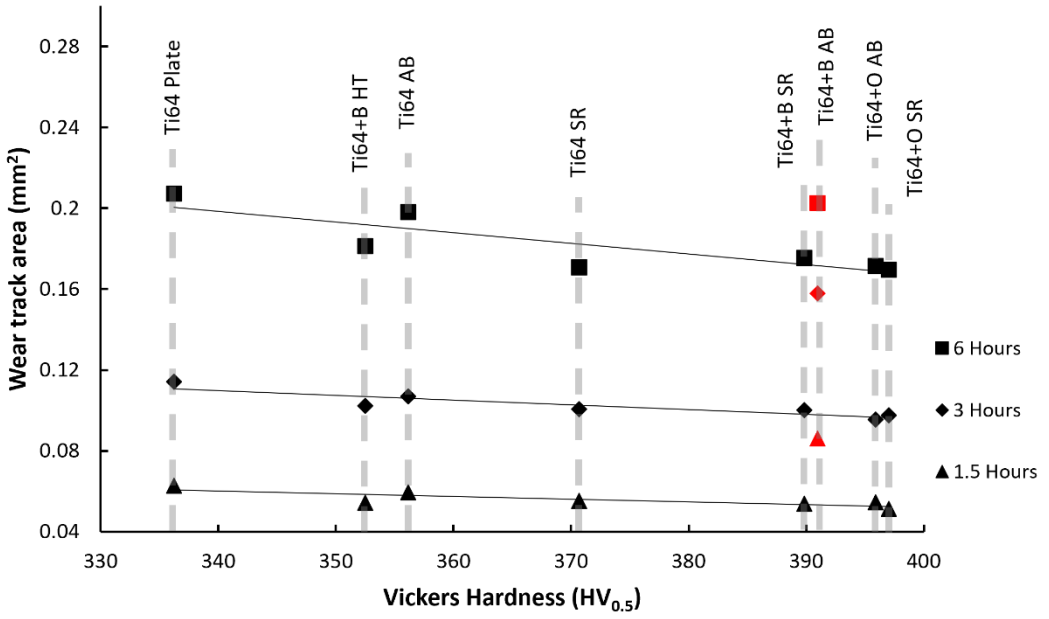

Figure 5.18: Wear track area compared with material hardness for Ti64 and modified alloys against Si_3N_4 in salt water. Conditions: AB=as-built, SR=stress relieved, HT=annealed.

When further comparing wear rates with hardness in Figure 5.19 it is evident that the wear properties of boron containing material are somewhat different to the other materials of the study. Ti64+B differs from the trend in the as-built condition with an initial high wear rate and steady state low wear rate. This does not correspond to the average hardness when compared to Ti64 and oxygen modified material. Additionally, the annealed Ti64 with boron has an average wear rate lower than might be expected due to its comparatively low hardness.

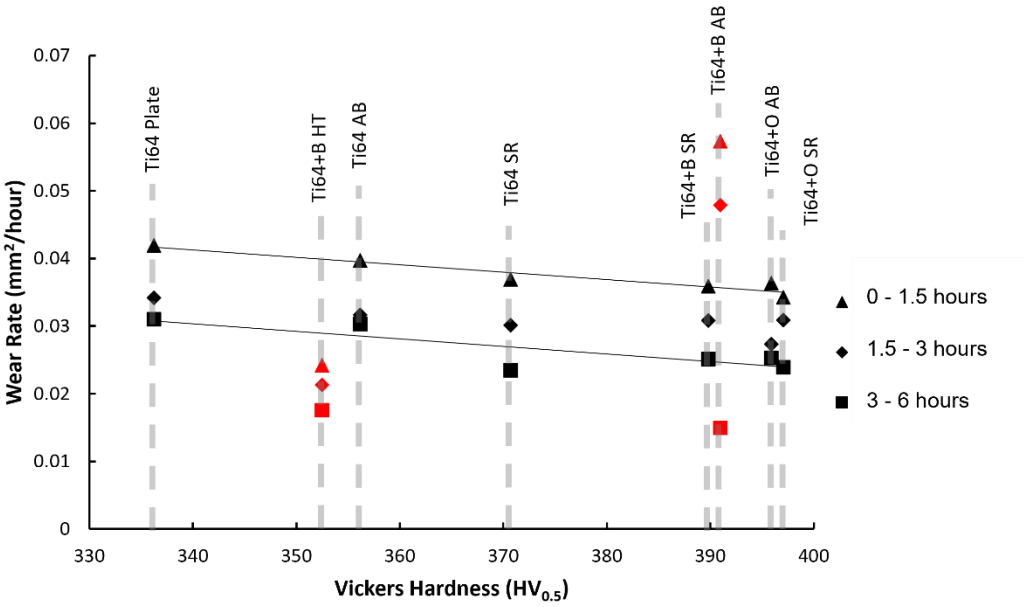

Figure 5.19: Wear rate during the specified time intervals compared with material hardness for Ti64 and modified alloys against Si_3N_4 in salt water.

Hardness appears to have a relationship with the wear performance of Ti64 and Ti64 with additional oxygen where higher material hardness results in a reduction in wear rate. This does not appear to be the case with boron addition. Adding boron to titanium does have an influence on the wear properties with the annealed condition presenting reduced wear rates below that which may be explained by the hardness of the material.

The cause of this difference in wear is not clearly explained through observations in the wear tracks. The wear mechanisms of abrasion and adhesive tearing are both evident to a similar extent as the other titanium materials. There may be a difference in interaction between the surfaces of the wearing pairs with the inclusion of boron but is it not obviously evident in the wear tracks.

Hardness of a material is a significant factor in wear performance along with many other properties that influence this process. Titanium wear is typically dominated by adhesive processes which result in free particle generation at the wearing interface and lead to three-body abrasion taking place [204]. Adhesive wear processes have been related to hardness through the Archard wear model where the wear volume is inversely proportional to hardness [210]. This model is limited in predictive capability due to the use of a factor known as the wear coefficient

that is empirically derived and accounts for other parameters involved in wear. Some wear mechanisms that are poorly described by Archard's model include erosion, contact fatigue, corrosive wear, and micro-cracking [211-213].

The linear relationship between hardness and wear rate for most material of this study (Figure 5.19) suggest that these materials share a similar wear coefficient in Archard's model. The Ti64+B material in the as-built and the annealed conditions do not appear to follow the same relationship. The presence of boron particulates have likely altered other wear related parameters not specifically accounted for in Archard's model, and as such appears to deviate from the wear rate vs hardness relationship that describes the performance of the other materials. Either typical titanium adhesive wear processes have been altered, or other material properties have changed that influence wear behaviour. Further investigation of these materials would be required to characterise material properties not explored in this work that may describe this wear behaviour and identify the mechanism through which these apply to the observed wear performance.

Additionally, the significance of the silicon nitride counterbody has also not been quantified through this work. The establishment of a metal transfer film on the Si_3N_4 suggests there could be an interaction in the wear paring under salt water. This could change the friction properties of these parings against the modified Ti64 materials which could be explored in further experiments with equipment able to investigate friction coefficients.

5.6 Summary

There is little improvement in wear resistance of these materials under the conditions of this study with regards to commercially available Ti64 material. This was despite changes in microstructure, hardness, and mechanical performance. Hardness is a useful metric for identifying the wear resistance of Ti64 with regards to an increased oxygen content however boron addition does not follow this trend. The limited change in wear performance does not justify these materials for applications where wear resistance is required beyond the current performance of commercial Ti64.

Chapter 6
Conclusions and Recommendations

6.1 Overview

The conclusions of this thesis will be presented as a summary of the key findings from each chapter with reference to the implications of these results and the contribution this work makes to expanding the knowledge of the field. Outcomes of this work are summaries in reference to the thesis objectives and recommendations for future investigation are made

6.2 Process Development and Optimisation of SLM

Chapter 3 concluded that the optimisation of parameters using the energy density formula is an effective method for comparing processing parameters. While this does not account for all variation that is observed in density and hardness of manufactured samples, it does effectively represent general trends. There are a number of other parameters which have an influence on consolidation in the SLM processes which lead to significant differences in optimised SLM parameters reported by other researchers (making direct comparisons difficult between literature in the field, as not all parameters are published.)

For this study it was observed that there was variation in sample hardness and density when parts were manufactured from different sets of parameters that had the same energy density. However, this variation was small and overall energy density values provide an effective metric for relating porosity and microstructural differences within an individual study.

This study showed that fine boron and TiO_2 powders could be added in small proportions to Ti64 powder feedstock for the SLM process by simply mixing these different materials. The added powders were successfully incorporated into SLM manufactured parts in-situ during the process with little disparity between the amount of added elements and the composition of the final product. In as-built material there was some incomplete mixing of the additives, which can be reduced by selecting suitable SLM operating parameters.

Porosity was identified in samples at both low and high energy density levels which is in line with literature. Lack of fusion porosity was identified in samples manufactured with low energy density and gas entrapment pores were generated using high energy density parameters.

It was concluded that optimum SLM parameters for manufacturing both boron, and oxygen modified Ti64 had an energy density level of 54.5 J/mm^3. This was identified as producing material with high relative density (>99%), low variation in hardness (<±10 $HV_{0.5}$), and good incorporation and mixing of the additive materials, as identified in microstructure cross sections.

Analysis in Chapter 3 also highlighted that efficient production of samples using additive manufacturing can be further improved for research by designing samples that take advantage of the additive manufacturing process. This process enables the manufacture of multiple samples with different parameters in a single build. Samples that combine different experiments into a single part can simplify preparation and streamline research investigations. A segmented disk sample was developed for this research which provided results of: hardness, microstructures, and porosity identification, for 16 different manufacturing parameter variations in a single, easy to process part. These samples aided in the investigations of this study and the optimisation of processing parameters for SLM manufacturing Ti64 modified with additional boron and oxygen. This type of sample preparation is not present in the literature reviewed during this study and could aid researchers in the field by enabling rapid testing of multiple processing conditions at once, simplifying sample preparation and record keeping.

6.3 Microstructure and Mechanical Properties

Samples which successfully incorporated oxygen and boron were compared to Ti64 in Chapter 4. The influence the additives had on the development of the as-built SLM microstructures and after two standard heat treatments (stress relief and sub β-transus annealing) were assessed. These microstructures were further compared to the mechanical performance of the materials to classify observed behaviour.

SLM fabricated Ti64 demonstrated expected behaviour with regards to different heat treatments, the as-built material consisted of fine lamella α' martensite, the texture of which was mostly retained after stress relief treatment as α phase and any untransformed α'. Annealing below the β-transus transformed the material to lamella α+β phase with significant coarsening of the lamella. Columnar colony/prior-β grain texture was observed extending in the build direction through multiple layers and was unchanged by the heat treatments of this study.

There were no significant differences in microstructure between the Ti64 and the Ti64 with additional oxygen across the different heat treatment conditions. One small difference was the presence of a boundary region around columnar prior-β colonies; however, the phases within this apparent boundary region were equivalent to that of the columnar colonies they formed around. Heat treatments performed on the oxygen enriched material caused the same transformations as the unmodified Ti64, transforming from fine α' martensite to coarser α+β arranged in prior-β colonies that persist through the heat treatments.

In comparison, the addition of boron caused large changes to the microstructure of SLM Ti64. There was significant refinement of the α' martensite colonies that form from prior-β grains. This included the elimination of the columnar structure that propagates through build layers. The presence of boron also results in texture effects linked with the laser scan pattern, with the boundary of laser melted tracks remaining visible when etched. This visible feature was retained through both heat treatment conditions but was not discernible as concentrations of particulates or different elemental concentrations. Relatively large needle like TiB particulates only became visible in the modified material after annealing at 920°C for 2 hours. These do not appear to form with any preference to the laser track features or prior-β grain boundaries. The appearance of the larger TiB needles is attributed to diffusion of boron and growth occurring during high temperature heat treatment. Much finer TiB must exist distributed throughout the as-built material which diffuses to form the visible TiB needles under heat treatment.

The implication of the microstructural observations is that small amounts of boron may be added to Ti64 and result in significant refinement of the grain structure.

The process of adding and boron is simplified by the in-situ incorporation during the SLM process. This eliminates the appearance of columnar prior-β colonies that have been identified as contributing to anisotropic properties. Other features are introduced into the microstructure by the boron addition and investigation into the influence of these on anisotropy of the material is an area of future study.

Both boron and oxygen addition increased the compressive yield strength and hardness of the SLM printed Ti64. In each heat treatment condition, the oxygen modified material had the greatest improvement in yield strength, up to 16% higher than that of Ti64. While hardness of the boron modified Ti64 was increased, in the annealed condition this was relatively small and corresponded to the appearance of larger TiB whisker particulates. Through diffusion of boron in the annealing process, these whiskers grew and reduced the distribution of boron compounds throughout the material, reducing the hardening effect. Overall, the observed strengthening of the materials was caused by interstitial hardening in the case of oxygen addition and predominantly through grain refinement in the presence of added boron.

The Young's modulus of the materials also changed with respect to the additives and the different heat treatments. The addition of boron increases the modulus of Ti64 in all material conditions and is attributed to the presence of TiB phase that is stiffer than the matrix material along with the refined grain structure. TiB particles were only observed in the annealed condition however, this stiffening effect is consistent across all conditions and is evidence of very fine TiB influencing the material. The low solubility of boron in titanium and reaction paths that occur determine that TiB must be present, the increase in stiffness is evidence of this however these very find TiB particles were not detected by techniques used in this study. The addition of oxygen causes an overall increase in Young's modulus greater than that observed in the boron modified material. This is attributed to greater proportion of α phase being developed by the α stabilising effect of oxygen.

No significant difference in plastic compressive behaviour was observed between the modified materials and their heat-treated conditions. Increases in strain

energy density required to deform the materials, up to 4% strain, is explained by the differences in compressive yield strength, with no discernible differences in plastic deformation behaviour.

6.4 Wear Characterisation

It was hypothesised that the wear performance of the modified Ti64 materials may be altered by the boron and oxygen inclusion, however there was little difference in wear mechanisms taking place between the materials of this study compared to commercial Ti64 plate material.

Mechanisms of adhesion and third body abrasion were evident in wear tracks, which is consistent with typical performance of Ti64. Both Ti64 and the oxygen modified material present wear performance that changes linearly with respect to the materials hardness. This is an expected result as an increase in hardness corresponds with a reduction in the amount of wear damage in other materials.

Boron modification resulted in different wear behaviour to that of the other materials. The as-built material had a high initial wear rate which reduced significantly as the test duration increased. After stress relief treatment this behaviour was lost, with wear performance equivalent to Ti64 and the oxygen modified material. Annealing results in a low wear rate that does not correspond to the relatively low hardness of this material, in contrast to Ti64 and Ti64 with oxygen added

Overall, there is little difference in wear performance of the SLM materials compared to commercial Ti64 plate. Minor differences in the amount of wear are apparent with respect to hardness however these offer little advantage to extending the use of SLM manufactured Ti64 into wear applications. While these material combinations may not be suited for wear applications, in-situ modification of metals through the SLM process is possible, and does develop different behaviours in the resultant materials. For different reinforcement/matrix combinations the SLM process may enable significant improvements in wear performance.

6.5 Outcomes of Thesis Objectives

This work achieved the thesis objectives as summarised below.

Objective 1: Analytically compare sample properties using different process parameters to generate processing windows for the in-situ modified material

This objective was met by successfully developing processing parameters for SLM manufacture of modified Ti64. Investigation of energy density levels and sources of variation identified energy density as an effective parameter for process optimisation. Variation in the process exists that are linked to a number of other parameters, however general trends are suitably correlated to energy density.

Objective 2: To investigate how processing may influence the distribution and homogeneity of the modified material.

This investigated how the oxygen and boron additives became incorporated and distributed within the materials through parameter development and heat treatments. Suitable processing parameter levels could be identified that evenly distributed the additives through SLM processing. The additives, especially boron, had an impact on the microstructures developed from the process and after subsequent heat treatment, with annealing resulting in development of distributed, larger TiB whisker particulates.

Objective 3: Characterise the effect the additives have on the mechanical and wear properties of the resultant materials.

The effect of boron and oxygen modification on SLM manufactured Ti64 was investigated through hardness measurements, compressive properties, and wear performance. Heat treated conditions were also characterised. Hardness and compressive strength were increased by the modifying additions through all treatment conditions, although some of these increases were modest. Wear behaviour was also characterised and found to have no substantial change in performance that would enable new applications. While there were limited improvements in performance of these modified materials, differences in microstructure, specifically with the addition of boron, may improve other properties not investigated in this study.

6.6 Recommendations

From this work a number of areas were identified for future study. These were not investigated in this work as they were either out of scope or because data collection was limited by available techniques. These are:

- Identify distribution and nature of proposed fine boron particulates in as-built material.

  Fine TiB particulates are proposed to be broadly distributed throughout the modified Ti64 in the as-built condition. This could not be proven due to detection limits and availability of equipment. Further exploration via transmission electron microscopy would confirm the nature of boron in the as-built condition. This would help to explain the mechanism of TiB whisker formation and how this may be influenced to alter the distribution of TiB particulates observed after heat treatment.

- Investigate anisotropy in the boron modified Ti64:

  The microstructure developed by the as-built Ti64 with boron after SLM processing eliminated the typical directionally aligned features microstructure of SLM manufactured Ti64. This was replaced by a macro texture of parallel features in the horizontal cross section, consistent with the path of the laser tracks. This new structure formed in the Ti64+B may introduce different anisotropic properties compared to those of traditional Ti64. As features are present that align with the laser tracks, different laser scan patterns may develop different directional properties. Developing an understanding this phenomenon may give rise to a new approach for the modification of SLM materials through boron addition and laser track orientation. This could be employed to produce parts where mechanical properties can be specified with a customisable orientation.

- Investigate other mechanical properties of boron modified Ti64 to determine if the substantially different microstructure causes significant improvement.

The effect of a small addition of boron significantly alters the microstructure of SLM manufactured Ti64. Mechanical properties of compression strength, hardness, stiffness, and wear were investigated in this study and showed only minor differences compared to unmodified Ti64. The different microstructure in the presence of boron may significantly impact other properties of Ti64 outside the scope of this work. For example: creep resistance, fatigue, and impact strength. Investigations into these properties could identify new applications where this material has a significant benefit.

- Investigate friction coefficients for these modified materials to improve the understanding of wear characteristics.

  Analysis of wear rates for these modified Ti64 materials identified as-built Ti64+B as initially having very high rates of wear. The wear mechanisms taking place did not obviously distinguish behaviour of this material from the others in this study. Friction coefficient data was unavailable with the reciprocating pin-on-disk equipment used. This data may provide evidence that clarifies this behaviour.

- Investigate tribochemical interaction between the silicon nitride counterbody and titanium wearing materials:

  Si_3N_4 may have tribochemical interactions with the salt water and titanium paring which could have an influence on friction coefficients. Further study into the friction between the wearing materials in this study would help understand if any significant chemical interactions are taking place that have an influence on tribological properties. Study of wear debris composition could also help determine these interactions that might be of benefit in wearing applications of SLM modified titanium.

6.7 List of Publications

6.7.1 Publications directly relating to this thesis

B. Jackson, R. Torrens, L. Bolzoni, F. Yang, M. Fry, A. Mukhtar, Additive Manufacturing of Ti-6Al-4V with Added Boron: Microstructure and Hardness Modification, Key Engineering Materials 770 (2018) 165-173.

B. Jackson, R. Torrens, L. Bolzoni, F. Yang, N. Ross, M. Fry, Wear performance of selective laser melted Ti-6Al-4V alloy in situ modified with oxygen and boron, International Journal of Modern Physics B 34(01n03) (2019) 2040027.

6.7.2 Other relevant work

P. Franz, A. Mukhtar, W. Downing, G. Smith, **B. Jackson**, Mechanical Behaviour of Gas Nitrided Ti6Al4V Bars Produced by Selective Laser Melting, Key Engineering Materials 704 (2016) 225-234.

A. Mukhtar, M. Fry, **B. Jackson**, Evaluation of Nitriding and Surface Machining Effects on Tensile and Fatigue Properties of Additively Manufactured Ti6Al4V, World Congress on Powder Metallurgy – WORLDPM2018, Beijing, China, Proceedings USB Version, Part 11, 2018, pp. 1575-1583.

A. Mukhtar, M. Fry, **B. Jackson**, L. Bolzoni, Effects of Gas Nitriding on Fatigue and Crack Initiation of Ti6Al4V produced by Selective Laser Melting, Materials Research (online) 22(suppl 2) (2019).

T. Pasang, B. Tavlovich, O. Yannay, **B. Jackson**, M. Fry, Y. Tao, C. Turangi, J.-C. Wang, C.-P. Jiang, Y. Sato, M. Tsukamoto, W.Z. Misiolek, Directionally-Dependent Mechanical Properties of Ti6Al4V Manufactured by Electron Beam Melting (EBM) and Selective Laser Melting (SLM), Materials (Basel) 14(13) (2021) 3603.

References

[1] M.J. Donachie, Titanium: a technical guide, 2nd ed., ASM International, Materials Park, OH, 2000.
[2] W. Zhang, Z. Zhu, C.Y. Cheng, A literature review of titanium metallurgical processes, Hydrometallurgy 108(3–4) (2011) 177-188.
[3] E. Poulsen, J. Hall, Extractive Metallurgy of Titanium: A Review of the State of the Art and Evolving Production Techniques, JOM 35(6) (1983) 60-65.
[4] T. Saito, T. Furuta, T. Yamaguchi, Development of low cost titanium matrix composite, JOM, 1995, pp. 33-44.
[5] F.H. Froes, D. Eylon, Powder metallurgy of titanium alloys, International Materials Reviews 35(1) (1990) 162-184.
[6] W.T. Roberts, Titanium, Endeavour 7(4) (1983) 189-193.
[7] MatWeb, MatWeb: Material property data, 2014. http://www.matweb.com/. (Accessed August 2014).
[8] M. Peters, J. Hemptenmacher, J. Kumpfert, C. Leyens, Structure and Properties of Titanium and Titanium Alloys, Titanium and Titanium Alloys, Wiley-VCH Verlag GmbH & Co. KGaA, 2003, pp. 1-36.
[9] G. Welsch, R. Boyer, E.W. Collings, Materials Properties Handbook: Titanium Alloys, ASM International, 1993.
[10] S. Liu, Y.C. Shin, Additive manufacturing of Ti6Al4V alloy: A review, Materials & Design 164 (2019) 107552.
[11] ASTM, Standard B348-13 "Standard Specification for Titanium and Titanium Alloy Bars and Billets", ASTM international, West Conshohocken, PA, 2013.
[12] S.R. Nutt, A.W. Ruff, Study of the Friction and Wear Behavior of Titanium Under Dry Sliding Conditions, Wear of Materials: International Conference on Wear of Materials, 1983, pp. 426-433.
[13] K.G. Budinski, Tribological properties of titanium alloys, Wear 151(2) (1991) 203-217.
[14] S. Chauhan, K. Dass, Dry Sliding Wear Behaviour of Titanium (Grade 5) Alloy by Using Response Surface Methodology, 2013.
[15] S.C. Tjong, Z.Y. Ma, Microstructural and mechanical characteristics of in situ metal matrix composites, Materials Science and Engineering: R: Reports 29(3–4) (2000) 49-113.
[16] I.A. Ibrahim, F.A. Mohamed, E.J. Lavernia, Particulate reinforced metal matrix composites — a review, Journal of Materials Science 26(5) (1991) 1137-1156.
[17] Y.J. Kim, H. Chung, S.J.L. Kang, In situ formation of titanium carbide in titanium powder compacts by gas–solid reaction, Composites Part A: Applied Science and Manufacturing 32(5) (2001) 731-738.
[18] R.R. Kieschke, H.E. Deve, C. McCoullough, C.J. Griffin, Processing of Tow-Based Titanium Composites, in: F.H. Froes, J. Storer (Eds.) Recent Advances in Titanium Metal Matrix Composites, Rosemont, Illinois, 1994.
[19] D.B. Miracle, Aeronautical Applications of Metal-Matrix Composites, in: D.B. Miracle, S.I. Donaldson (Eds.), ASM Handbook, Composites, ASM International, 2001, pp. 1043-1049.
[20] J.F. Shackelford, W. Alexander, CRC Materials Science and Engineering Handbook, CRC Press, 2000.

[21] Z.F. Yang, W.J. Lu, D. Xu, J.N. Qin, D. Zhang, In situ synthesis of hybrid and multiple-dimensioned titanium matrix composites, Journal of Alloys and Compounds 419(1–2) (2006) 76-80.
[22] L. Cai, Y. Zhang, L. Shi, H. Yang, M. Xi, Research on development of in situ titanium matrix composites and in situ reaction thermodynamics of the reaction systems, Journal of University of Science and Technology Beijing, Mineral, Metallurgy, Material 13(6) (2006) 551-557.
[23] S. Ranganath, A review on particulate-reinforced titanium matrix composites, Journal of Materials Science 32(1) (1997) 1-16.
[24] Y.Y. Zhao, P.S. Grant, Z.X. Guo, B. Cantor, The Mechanical Behaviour of SiC Fibres in a Ti Matrix During Fabrication by Vacuum Plasma Spraying and Vacuum Hot Pressing, in: F.H. Froes, J. Storer (Eds.) Recent Advances in Titanium Metal Matrix Composites, Rosemont, Illinois, 1994.
[25] SP Aerospace, Metal matrix composite landing gear component, SP Aerospace, Geldrop, Netherlands, 2003.
[26] S.C. Tjong, Y.-W. Mai, Processing-structure-property aspects of particulate- and whisker-reinforced titanium matrix composites, Composites Science and Technology 68(3–4) (2008) 583-601.
[27] T. Saito, T. Furuta, T. Yamaguchi, Development of low cost titanium alloy matrix composites, in: F.H. Froes, J. Storer (Eds.) Recent Advances in Titanium Metal Matrix Composites, Rosemont, Illinois, 1994.
[28] K.S. Ravi Chandran, K.B. Panda, S.S. Sahay, TiBw-reinforced Ti composites: Processing, properties, application prospects, and research needs, JOM 56(5) (2004) 42-48.
[29] X. Ma, C. Li, Z. Du, W. Zhang, Thermodynamic assessment of the Ti–B system, Journal of Alloys and Compounds 370(1-2) (2004) 149-158.
[30] S. Tamirisa, D. Miracle, An Overview of Titanium Alloys Modified with Boron, in: M.Niinomi, S. Akiyama, M. Ikeda, M. Hagiwara, K. Maruyama (Eds.) 11th World Conference on Titanium (JIMIC5), Japan Institute of Metals, Kyoto, Japan, 2007, pp. 737-740.
[31] T. Saito, The automotive application of discontinuously reinforced TiB-Ti composites, JOM 56(5) (2004) 33-36.
[32] D. Xu, W.J. Lu, Z.F. Yang, J.N. Qin, D. Zhang, In situ technique for synthesizing multiple ceramic particulates reinforced titanium matrix composites (TiB+TiC+Y2O3)/Ti, Journal of Alloys and Compounds 400(1–2) (2005) 216-221.
[33] S. Gorsse, D.B. Miracle, Mechanical properties of Ti-6Al-4V/TiB composites with randomly oriented and aligned TiB reinforcements, Acta Materialia 51(9) (2003) 2427-2442.
[34] K. Morsi, V.V. Patel, Processing and properties of titanium–titanium boride (TiBw) matrix composites—a review, Journal of Materials Science 42(6) (2007) 2037-2047.
[35] X. Zhang, W. Lue, D. Zhang, R. Wu, Y. Bian, P. Fang, In situ technique for synthesizing (TiB + TiC)/Ti composites, Scripta Materialia 41(1) (1999).
[36] B.J. Kooi, Y.T. Pei, J.T.M. De Hosson, The evolution of microstructure in a laser clad TiB–Ti composite coating, Acta Materialia 51(3) (2003) 831-845.
[37] R.R. Atri, K.S. Ravichandran, S.K. Jha, Elastic properties of in-situ processed Ti–TiB composites measured by impulse excitation of vibration, Materials Science and Engineering: A 271(1–2) (1999) 150-159.

[38] T.M.T. Godfrey, A. Wisbey, P.S. Goodwin, K. Bagnall, C.M. Ward-Close, Microstructure and tensile properties of mechanically alloyed Ti–6A1–4V with boron additions, Materials Science and Engineering: A 282(1–2) (2000) 240-250.
[39] S. Gorsse, J.P. Chaminade, Y. Le Petitcorps, In situ preparation of titanium base composites reinforced by TiB single crystals using a powder metallurgy technique, Composites Part A: Applied Science and Manufacturing 29(9–10) (1998) 1229-1234.
[40] S. Tamirisakandala, R.B. Bhat, J.S. Tiley, D.B. Miracle, Grain refinement of cast titanium alloys via trace boron addition, Scripta Materialia 53(12) (2005) 1421-1426.
[41] O.O. Bilous, L.V. Artyukh, A.A. Bondar, T.Y. Velikanova, M.P. Burka, M.P. Brodnikovskyi, O.S. Fomichov, N.I. Tsyganenko, S.O. Firstov, Effect of boron on the structure and mechanical properties of Ti–6Al and Ti–6Al–4V, Materials Science and Engineering: A 402(1) (2005) 76-83.
[42] I. Sen, S. Tamirisakandala, D.B. Miracle, U. Ramamurty, Microstructural effects on the mechanical behavior of B-modified Ti–6Al–4V alloys, Acta Materialia 55(15) (2007) 4983-4993.
[43] W. Chen, C.J. Boehlert, The elevated-temperature fatigue behavior of boron-modified Ti–6Al–4V(wt.%) castings, Materials Science and Engineering: A 494(1) (2008) 132-138.
[44] I. Sen, K. Gopinath, R. Datta, U. Ramamurty, Fatigue in Ti–6Al–4V–B alloys, Acta Materialia 58(20) (2010) 6799-6809.
[45] B.-J. Choi, I.L.Y. Kim, Y.-Z. Lee, Y.-J. Kim, Microstructure and friction/wear behavior of (TiB+TiC) particulate-reinforced titanium matrix composites, Wear 318(1) (2014) 68-77.
[46] D.E. Alman, J.A. Hawk, The abrasive wear of sintered titanium matrix–ceramic particle reinforced composites, Wear 225-229 (1999) 629-639.
[47] S.K. Nayak, C.J. Hung, V. Sharma, S.P. Alpay, A.M. Dongare, W.J. Brindley, R.J. Hebert, Insight into point defects and impurities in titanium from first principles, npj Computational Materials 4(1) (2018) 11.
[48] H. Conrad, Effect of interstitial solutes on the strength and ductility of titanium, Progress in Materials Science 26(2) (1981) 123-403.
[49] H. Güleryüz, E. Atar, F. Seahjani, H. Çimenoğlu, An Overview on Surface Hardening of Titanium Alloys by Diffusion of Interstitial Atoms, Diffusion Foundations 4 (2015) 103-116.
[50] H. Okamoto, O-Ti (Oxygen-Titanium), Journal of Phase Equilibria and Diffusion 32(5) (2011) 473.
[51] A.I. Kahveci, G.E. Welsch, Effect of oxygen on the hardness and alpha/beta phase ratio of Ti6Al4V alloy, Scripta Metallurgica 20(9) (1986) 1287-1290.
[52] Y.V. Petunina, Effect of high oxygen and nitrogen contents on the mechanical properties of titanium, Metal Science and Heat Treatment of Metals 3(5) (1961) 276-279.
[53] D.J. Simbi, J.C. Scully, The effect of residual interstitial elements and iron on mechanical properties of commercially pure titanium, Materials Letters 26(1) (1996) 35-39.
[54] V.V. Vavilova, T.A. Peradze, L.P. Fatkullina, O.S. Korobov, Oxygen in titanium alloys with aluminum, Metal Science and Heat Treatment 17(3) (1975) 229-231.

[55] T.L. Jones, K. Kondoh, T. Mimoto, N. Nakanishi, J. Umeda, The Development of a Ti-6Al-4V Alloy via Oxygen Solid Solution Strengthening for Aerospace & Defense Applications, Key Engineering Materials 551 (2013) 118-126.
[56] K. Aniołek, M. Kupka, A. Barylski, Sliding wear resistance of oxide layers formed on a titanium surface during thermal oxidation, Wear 356-357 (2016) 23-29.
[57] R. Yazdi, H.M. Ghasemi, M. Abedini, C. Wang, A. Neville, Oxygen Diffusion Layer on Ti–6Al–4V Alloy: Scratch and Dry Wear Resistance, Tribology Letters 67(4) (2019) 101.
[58] T. Chen, S. Koyama, S. Nishida, L. Yu, Mechanical Properties and Frictional Wear Characteristic of Pure Titanium Treated by Atmospheric Oxidation, Materials (Basel) 14(12) (2021) 3196.
[59] D. Kümmel, J. Schneider, P. Gumbsch, Influence of Interstitial Oxygen on the Tribology of Ti6Al4V, Tribology Letters 68(3) (2020) 96.
[60] S.P. Ingole, Tribology of Metals and Alloys, in: P.L. Menezes, M. Nosonovsky, S.P. Ingole, S.V. Kailas, M.R. Lovell (Eds.), Tribology for Scientists and Engineers: From Basics to Advanced Concepts, Springer New York, New York, NY, 2013, pp. 197-210.
[61] SLM Solutions GmbH, SLM 280 HL, 2014. http://stage.slm-solutions.com/index.php?slm-280_en. (Accessed August 2014).
[62] Y. Shang, Y. Yuan, Y. Zhang, D. Li, Y. li, Investigation into Effects of Scanning Speed on in Vitro Biocompatibility of Selective Laser Melted 316L Stainless Steel Parts, MATEC Web of Conferences 95 (2017) 01009.
[63] O. Rehme, C. Emmelmann, Reproducibility for properties of selective laser melting, Third International WLT-Conference in Laser Manufacturing, Munich, 2005.
[64] B. Zhang, Y. Li, Q. Bai, Defect Formation Mechanisms in Selective Laser Melting: A Review, Chinese Journal of Mechanical Engineering 30(3) (2017) 515-527.
[65] A. Sola, A. Nouri, Microstructural porosity in additive manufacturing: The formation and detection of pores in metal parts fabricated by powder bed fusion, Journal of Advanced Manufacturing and Processing 1(3) (2019) n/a.
[66] S. Coeck, M. Bisht, J. Plas, F. Verbist, Prediction of lack of fusion porosity in selective laser melting based on melt pool monitoring data, Additive Manufacturing 25 (2019) 347-356.
[67] H.J. Niu, I.T.H. Chang, Instability of scan tracks of selective laser sintering of high speed steel powder, Scripta Materialia 41(11) (1999) 1229-1234.
[68] D. Gu, Y. Shen, Balling phenomena in direct laser sintering of stainless steel powder: Metallurgical mechanisms and control methods, Materials & Design 30(8) (2009) 2903-2910.
[69] Y.F. Shen, D.D. Gu, Y.F. Pan, Balling process in selective laser sintering 316 stainless steel powder, Key Engineering Materials 315-316 (2006) 357-360.
[70] G. Yu, D. Gu, D. Dai, M. Xia, C. Ma, K. Chang, Influence of processing parameters on laser penetration depth and melting/re-melting densification during selective laser melting of aluminum alloy, Applied Physics A 122(10) (2016) 891.
[71] J.J.S. Dilip, S. Zhang, C. Teng, K. Zeng, C. Robinson, D. Pal, B. Stucker, Influence of processing parameters on the evolution of melt pool, porosity, and

microstructures in Ti-6Al-4V alloy parts fabricated by selective laser melting, Progress in Additive Manufacturing 2(3) (2017) 157-167.
[72] J. Svenungsson, I. Choquet, A.F.H. Kaplan, Laser Welding Process – A Review of Keyhole Welding Modelling, Physics Procedia 78 (2015) 182-191.
[73] I. Yadroitsev, A. Gusarov, I. Yadroitsava, I. Smurov, Single track formation in selective laser melting of metal powders, Journal of Materials Processing Technology 210(12) (2010) 1624-1631.
[74] J.-P. Kruth, M. Badrossamay, E. Yasa, J. Deckers, L. Thijs, J. Van Humbeeck, Part and material properties in selective laser melting of metals, 16th International Symposium on Electromachining (ISEM XVI), Shanghai-China, 2010.
[75] S. Bai, N. Perevoshchikova, Y. Sha, X. Wu, The Effects of Selective Laser Melting Process Parameters on Relative Density of the AlSi10Mg Parts and Suitable Procedures of the Archimedes Method, Applied Sciences 9(3) (2019).
[76] G. Dzukey, k. Yang, Process Parameter Optimization for Selective Laser Melting of 316L Stainless Steel Material using Taguchi's Statistical Design of Experiment Procedure, International Journal of Engineering and Technology 11 (2019) 6-13.
[77] H. Attar, M. Bönisch, M. Calin, L.-C. Zhang, S. Scudino, J. Eckert, Selective laser melting of in situ titanium–titanium boride composites: Processing, microstructure and mechanical properties, Acta Materialia 76 (2014) 13-22.
[78] T.H. Childs, C. Hauser, Raster scan selective laser melting of th surface layer of a tool steel powder bed, Proceedings of the Institution of Mechanical Engineers 219(Part B) (2005) 379-384.
[79] C. Wright, M. Youseffi, S. Akhtar, T.H. Childs, C. Hauser, P. Fox, Selective laser melting of prealloyed high alloy steel powder beds, Material Science Forum 514 (2006) 516-523.
[80] B. Zhang, H. Liao, C. Coddet, Microstructure evolution and density behavior of CP Ti parts elaborated by Self-developed vacuum selective laser melting system, Applied Surface Science 279 (2013) 310-316.
[81] B. Song, S. Dong, B. Zhang, H. Liao, C. Coddet, Effects of processing parameters on microstructure and mechanical property of selective laser melted Ti6Al4V, Materials & Design 35 (2012) 120-125.
[82] M. Elsayed, M. Ghazy, Y. Youssef, K. Essa, Optimization of SLM process parameters for Ti6Al4V medical implants, Rapid Prototyping Journal 25(3) (2019) 433-447.
[83] A. Simchi, H. Pohl, Effects of laser sinterinng processing parameters on the microstructure and densification of iron powder, Materials Science and Engineering: A 359(1-2) (2003) 119-128.
[84] E.O. Olakanmi, R.F. Cochrane, K.W. Dalgarno, Densification mechanism and microstructural evolution in selective laser sintering of Al–12Si powders, Journal of Materials Processing Technology 211(1) (2011) 113-121.
[85] L. Lu, J.Y.H. Fuh, Y.S. Wong, Laser-Induced Materials and Processes for Rapid Prototyping, Springer US, 2001.
[86] L. Thijs, F. Verhaeghe, T. Craeghs, J.V. Humbeeck, J.-P. Kruth, A study of the microstructural evolution during selective laser melting of Ti–6Al–4V, Acta Materialia 58(9) (2010) 3303-3312.
[87] S. Dadbakhsh, L. Hao, N. Sewell, Effect of selective laser melting layout on the quality of stainless steel parts, Rapid Prototyping Journal 18(3) (2012) 241-249.

[88] B. Ferrar, L. Mullen, E. Jones, R. Stamp, C.J. Sutcliffe, Gas flow effects on selective laser melting (SLM) manufacturing performance, Journal of Materials Processing Technology 212(2) (2012) 355-364.
[89] S. Das, H. Chung, Scaling Laws for Melting and Resolidification in Direct Selective Laser Sintering of Metals, Solid Freeform Fabrication Symposium, University of Texas, Austin, 2001.
[90] N.K. Tolochko, M.K. Arshinov, A.V. Gusarov, V.I. Titov, T. Laoui, L. Froyen, Mechanisms of selective laser sintering and heat transfer in Ti powder, Rapid Prototyping Journal 9(5) (2003) 314-326.
[91] T. Chen, Y. Zhang, Three-Dimensional Modeling of Laser Sintering of a Two-Component Metal Powder Layer on Top of Sintered Layers, Journal of Manufacturing Science and Engineering 129(3) (2007) 575.
[92] F. Verhaeghe, T. Craeghs, J. Heulens, L. Pandelaers, A pragmatic model for selective laser melting with evaporation, Acta Materialia 57(20) (2009) 6006-6012.
[93] A.V. Gusarov, I. Smurov, Modeling the interaction of laser radiation with powder bed at selective laser melting, Physics Procedia 5 (2010) 381-394.
[94] D.Q. Zhang, Q.Z. Cai, J.H. Liu, L. Zhang, R.D. Li, Select laser melting of W–Ni–Fe powders: simulation and experimental study, The International Journal of Advanced Manufacturing Technology 51(5-8) (2010) 649-658.
[95] H. Gong, K. Rafi, T. Starr, B. Stucker, The effects of processing parameters on defect regularity in Ti-6Al-4V parts fabricated by selective laser melting and electron beam melting, Solid Freeform Fabrication Symposium, University of Texas, Austin, 2013, pp. 424-439.
[96] M. Simonelli, Y.Y. Tse, C. Tuck, Effect of the build orientation on the mechanical properties and fracture modes of SLM Ti–6Al–4V, Materials Science and Engineering: A 616 (2014) 1-11.
[97] G. Kasperovich, J. Hausmann, Improvement of fatigue resistance and ductility of TiAl6V4 processed by selective laser melting, Journal of Materials Processing Technology 220 (2015).
[98] D. Gu, Y.-C. Hagedorn, W. Meiners, G. Meng, R.J.S. Batista, K. Wissenbach, R. Poprawe, Densification behavior, microstructure evolution, and wear performance of selective laser melting processed commercially pure titanium, Acta Materialia 60(9) (2012) 3849-3860.
[99] J. Sun, Y. Yang, D. Wang, Parametric optimization of selective laser melting for forming Ti6Al4V samples by Taguchi method, Optics & Laser Technology 49 (2013) 118-124.
[100] B. Vrancken, L. Thijs, J.-P. Kruth, J. Van Humbeeck, Heat treatment of Ti6Al4V produced by Selective Laser Melting: Microstructure and mechanical properties, Journal of Alloys and Compounds 541 (2012) 177-185.
[101] W.M. Steen, J. Mazumder, Laser Material Processing, Springer, London, 2010.
[102] P.A. Hooper, Melt pool temperature and cooling rates in laser powder bed fusion, Additive Manufacturing 22 (2018) 548-559.
[103] M. Shiomi, K. Osakada, K. Nakamura, T. Yamashita, F. Abe, Residual Stress within Metallic Model Made by Selective Laser Melting Process, CIRP Annals - Manufacturing Technology 53(1) (2004) 195-198.
[104] M. Matsumoto, M. Shiomi, K. Osakada, F. Abe, Finite element analysis of single layer forming on metallic powder bed in rapid prototyping by selective laser

processing, International Journal of Machine Tools and Manufacture 42(1) (2002) 61-67.
[105] T. Kühnle, K. Partes, In-Situ Formation of Titanium Boride and Titanium Carbide by Selective Laser Melting, Physics Procedia 39 (2012) 432-438.
[106] D. Bourell, B. Stucker, A.B. Spierings, N. Herres, G. Levy, Influence of the particle size distribution on surface quality and mechanical properties in AM steel parts, Rapid Prototyping Journal 17(3) (2011) 195-202.
[107] B. Liu, R. Wildman, C. Tuck, I. Ashcroft, R. Hague, Investigating the effect of particle size distributions on processing parameters optimisation in selective laser melting process, Solid Freeform Fabrication Symposium, University of Texas, Austin, 2011.
[108] Y. Shi, Y. Zhang, Simulation of random packing of spherical particles with different size distributions, Applied Physics A 92(3) (2008) 621-626.
[109] H.H. Zhu, J.Y.H. Fuh, L. Lu, The influence of powder apparent density on the density in direct laser-sintered metallic parts, International Journal of Machine Tools and Manufacture 47(2) (2007) 294-298.
[110] H.K. Rafi, N.V. Karthik, H. Gong, T.L. Starr, B.E. Stucker, Microstructures and Mechanical Properties of Ti6Al4V Parts Fabricated by Selective Laser Melting and Electron Beam Melting, Journal of Materials Engineering and Performance 22(12) (2013) 3872-3883.
[111] W. Frazier, Metal Additive Manufacturing: A Review, Journal of Materials Engineering and Performance 23(6) (2014) 1917-1928.
[112] L.E. Murr, S.M. Gaytan, D.A. Ramirez, E. Martinez, J. Hernandez, K.N. Amato, P.W. Shindo, F.R. Medina, R.B. Wicker, Metal Fabrication by Additive Manufacturing Using Laser and Electron Beam Melting Technologies, Journal of Materials Science & Technology 28(1) (2012) 1-14.
[113] S. Cecchel, D. Ferrario, G. Cornacchia, M. Gelfi, Development of Heat Treatments for Selective Laser Melting Ti6Al4V Alloy: Effect on Microstructure, Mechanical Properties, and Corrosion Resistance, 22(8) (2020) 2000359.
[114] N. Eshawish, S. Malinov, W. Sha, P. Walls, Microstructure and Mechanical Properties of Ti-6Al-4V Manufactured by Selective Laser Melting after Stress Relieving, Hot Isostatic Pressing Treatment, and Post-Heat Treatment, Journal of Materials Engineering and Performance 30(7) (2021) 5290-5296.
[115] G. Ter Haar, T. Becker, Selective Laser Melting Produced Ti-6Al-4V: Post-Process Heat Treatments to Achieve Superior Tensile Properties, Materials 11 (2018).
[116] L. Facchini, E. Magalini, P. Robotti, A. Molinari, S. Höges, K. Wissenbach, Ductility of a Ti-6Al-4V alloy produced by selective laser melting of prealloyed powders, Rapid Prototyping Journal 16(6) (2010) 450-459.
[117] C. Kenel, D. Grolimund, X. Li, E. Panepucci, V.A. Samson, D.F. Sanchez, F. Marone, C. Leinenbach, In situ investigation of phase transformations in Ti-6Al-4V under additive manufacturing conditions combining laser melting and high-speed micro-X-ray diffraction, Scientific reports 7(1) (2017) 16358-16358.
[118] P.A. Kobryn, S.L. Semiatin, The laser additive manufacture of Ti-6Al-4V, JOM 53(9) (2001) 40-42.
[119] R. Banerjee, P.C. Collins, A. Genç, H.L. Fraser, Direct laser deposition of in situ Ti–6Al–4V–TiB composites, Materials Science and Engineering: A 358(1-2) (2003) 343-349.

[120] Y. Zhang, J. Sun, R. Vilar, Characterization of (TiB+TiC)/TC4 in situ titanium matrix composites prepared by laser direct deposition, Journal of Materials Processing Technology 211(4) (2011) 597-601.
[121] F. Wang, J. Mei, X. Wu, Direct laser fabrication of Ti6Al4V/TiB, Journal of Materials Processing Technology 195(1) (2008) 321-326.
[122] M.J. Bermingham, D. Kent, H. Zhan, D.H. StJohn, M.S. Dargusch, Controlling the microstructure and properties of wire arc additive manufactured Ti–6Al–4V with trace boron additions, Acta Materialia 91 (2015) 289-303.
[123] H. Attar, S. Ehtemam-Haghighi, D. Kent, I.V. Okulov, H. Wendrock, M. Bönisch, A.S. Volegov, M. Calin, J. Eckert, M.S. Dargusch, Nanoindentation and wear properties of Ti and Ti-TiB composite materials produced by selective laser melting, Materials Science and Engineering: A 688 (2017) 20-26.
[124] H. Li, Z. Yang, D. Cai, D. Jia, Y.H. Zhou, Design, Microstructure evolution and mechanical properties of selective laser melted bulk-form titanium matrix nanocomposites with minor B4C additions, Materials 185 (2020) 108245.
[125] O.A. Quintana, W. Tong, Effects of Oxygen Content on Tensile and Fatigue Performance of Ti-6Al-4 V Manufactured by Selective Laser Melting, JOM 69(12) (2017) 2693-2697.
[126] A.T. Sutton, C.S. Kriewall, M.-C. Leu, J.W. Newkirk, Powders for Additive Manufacturing Processes: Characterization Techniques and Effects on Part Properties, Proceedings of the 27th Annual International Solid Freeform Fabrication Symposium, Austin, TX, 2016, pp. 1004-1030.
[127] ASTM, Standard E384-17 "Standard Test Method for Microindentation Hardness of Materials", ASTM international, West Conshohocken, PA, 2017.
[128] J. Schindelin, I. Arganda-Carreras, E. Frise, V. Kaynig, M. Longair, T. Pietzsch, S. Preibisch, C. Rueden, S. Saalfeld, B. Schmid, J.-Y. Tinevez, D.J. White, V. Hartenstein, K. Eliceiri, P. Tomancak, A. Cardona, Fiji: an open-source platform for biological-image analysis, Nature Methods 9(7) (2012) 676-682.
[129] ASTM, Standard E9-19 "Standard Test Methods of Compression Testing of Metallic Materials at Room Temperature", ASTM international, West Conshohocken, PA, 2019.
[130] ASTM, Standard E8/E8M-15a "Standard Test Methods for Tension Testing of Metallic Materials", ASTM international, West Conshohocken, PA, 2015.
[131] ASTM, G133-05(2016) "Standard Test Method for Linearly Reciprocating Ball-on-Flat Sliding Wear", ASTM International, West Conshohocken, PA, 2016.
[132] L. Dowling, J. Kennedy, S. O'Shaughnessy, D. Trimble, A review of critical repeatability and reproducibility issues in powder bed fusion, Materials & Design 186 (2020) 108346.
[133] C. Qiu, N.J.E. Adkins, M.M. Attallah, Microstructure and tensile properties of selectively laser-melted and of HIPed laser-melted Ti–6Al–4V, Materials Science and Engineering: A 578 (2013) 230-239.
[134] S. Pal, N. Gubeljak, R. Hudák, G. Lojen, V. Rajťúková, T. Brajlih, I. Drstvenšek, Evolution of the metallurgical properties of Ti-6Al-4V, produced with different laser processing parameters, at constant energy density in selective laser melting, Results in Physics 17 (2020) 103186.
[135] T. Vilaro, C. Colin, J.D. Bartout, As-Fabricated and Heat-Treated Microstructures of the Ti-6Al-4V Alloy Processed by Selective Laser Melting, Metallurgical and Materials Transactions A 42(10) (2011) 3190-3199.

[136] K.Q. Le, C. Tang, C.H. Wong, On the study of keyhole-mode melting in selective laser melting process, International Journal of Thermal Sciences 145 (2019) 105992.
[137] Y. Huang, T.G. Fleming, S.J. Clark, S. Marussi, K. Fezzaa, J. Thiyagalingam, C.L.A. Leung, P.D. Lee, Keyhole fluctuation and pore formation mechanisms during laser powder bed fusion additive manufacturing, Nature Communications 13(1) (2022) 1170.
[138] J.O. Milewski, Additive Manufacturing of Metals: From Fundamental Technology to Rocket Nozzles, Medical Implants, and Custom Jewelry, Springer International Publishing, 2017.
[139] S. Pal, N. Gubeljak, R. Hudak, G. Lojen, V. Rajtukova, J. Predan, V. Kokol, I. Drstvensek, Tensile properties of selective laser melting products affected by building orientation and energy density, Materials Science and Engineering: A 743 (2019) 637-647.
[140] C.L.A. Leung, S. Marussi, R.C. Atwood, M. Towrie, P.J. Withers, P.D. Lee, In situ X-ray imaging of defect and molten pool dynamics in laser additive manufacturing, Nature Communications 9(1) (2018) 1355.
[141] M.J. Torkamany, P. Parvin, M. Jandaghi, J. Sabbaghzadeh, Estimation of Composition Change in Pulsed Nd:YAG Laser Welding, in: X. Na (Ed.), Laser Welding, IntechOpen, 2010.
[142] J. Berlin, Analysis of Boron with Energy Dispersive X-ray Spectrometry: Advances in Light Element Analysis with SDD Technology, Imaging and Microscopy (2011) 20-21.
[143] J. Koch, D. Günther, Review of the State-of-the-Art of Laser Ablation Inductively Coupled Plasma Mass Spectrometry, Applied Spectroscopy 65(5) (2011) 155A-162A.
[144] G. Zhang, J. Chen, M. Zheng, Z. Yan, X. Lu, X. Lin, W. Huang, Element Vaporization of Ti-6Al-4V Alloy during Selective Laser Melting, Metals - Open Access Metallurgy Journal 10 (2020) 435.
[145] L. Thijs, K. Kempen, J.-P. Kruth, J. Van Humbeeck, Fine-structured aluminium products with controllable texture by selective laser melting of pre-alloyed AlSi10Mg powder, Acta Materialia 61(5) (2013) 1809-1819.
[146] J. Yang, H. Yu, J. Yin, M. Gao, Z. Wang, X. Zeng, Formation and control of martensite in Ti-6Al-4V alloy produced by selective laser melting, Materials & Design 108 (2016) 308-318.
[147] J. Han, J. Yang, H. Yu, J. Yin, M. Gao, Z. Wang, X. Zeng, Microstructure and mechanical property of selective laser melted Ti6Al4V dependence on laser energy density, Rapid Prototyping Journal 23(2) (2017) 217-226.
[148] D.K. Do, P. Li, The effect of laser energy input on the microstructure, physical and mechanical properties of Ti-6Al-4V alloys by selective laser melting, Virtual and Physical Prototyping 11(1) (2016) 41-47.
[149] S. Pal, G. Lojen, V. Kokol, I. Drstvensek, Evolution of metallurgical properties of Ti-6Al-4V alloy fabricated in different energy densities in the Selective Laser Melting technique, Journal of Manufacturing Processes 35 (2018) 538-546.
[150] T. Ahmed, H.J. Rack, Phase transformations during cooling in α+β titanium alloys, Materials Science and Engineering: A 243(1) (1998) 206-211.
[151] H. Beladi, Q. Chao, G.S. Rohrer, Variant selection and intervariant crystallographic planes distribution in martensite in a Ti–6Al–4V alloy, Acta Materialia 80 (2014) 478-489.

[152] M. Strantza, R. Vafadari, D. de Baere, B. Vrancken, W. van Paepegem, I. Vandendael, H. Terryn, P. Guillaume, D. van Hemelrijck, Fatigue of Ti6Al4V Structural Health Monitoring Systems Produced by Selective Laser Melting, Materials (Basel) 9(2) (2016).
[153] P.S. Prevéy, D.J. Hornbach, X-Ray Diffraction Residual-Stress Techniques, Materials Characterization, ASM International, 2019, p. 0.
[154] J. He, D. Li, W. Jiang, L. Ke, G. Qin, Y. Ye, Q. Qin, D. Qiu, The Martensitic Transformation and Mechanical Properties of Ti6Al4V Prepared via Selective Laser Melting, Materials (Basel) 12(2) (2019) 321.
[155] W. Xu, M. Brandt, S. Sun, J. Elambasseril, Q. Liu, K. Latham, K. Xia, M. Qian, Additive manufacturing of strong and ductile Ti–6Al–4V by selective laser melting via in situ martensite decomposition, Acta Materialia 85 (2015) 74-84.
[156] M. Yan, W. Xu, M.S. Dargusch, H.P. Tang, M. Brandt, M. Qian, Review of effect of oxygen on room temperature ductility of titanium and titanium alloys, Powder Metallurgy 57(4) (2014) 251-257.
[157] B.F. Vicente, R.N.D. Correa, A.G.T. Donato, E.V. Arana-Chavez, A.R.M. Buzalaf, R.C. Grandini, The Influence of Small Quantities of Oxygen in the Structure, Microstructure, Hardness, Elasticity Modulus and Cytocompatibility of Ti-Zr Alloys for Dental Applications, Materials 7(1) (2014).
[158] J. Guoyu, Thesis: The Effect of Oxygen Content on the Tensile Properties of SLMed Ti6Al4V alloy, Faculty of Engineering: Materials Science and Engineering, Monash University, 2017.
[159] E. Fereiduni, A. Ghasemi, M. Elbestawi, Selective laser melting of hybrid ex-situ/in-situ reinforced titanium matrix composites: Laser/powder interaction, reinforcement formation mechanism, and non-equilibrium microstructural evolutions, Materials & Design 184 (2019) 108185.
[160] S.S. Sahay, K.S. Ravichandran, R. Atri, B. Chen, J. Rubin, Evolution of microstructure and phases in in situ processed Ti–TiB composites containing high volume fractions of TiB whiskers, Journal of Materials Research 14(11) (1999) 4214-4223.
[161] O.M. Ivasishin, R.V. Teliovych, V.G. Ivanchenko, S. Tamirisakandala, D.B. Miracle, Processing, Microstructure, Texture, and Tensile Properties of the Ti-6Al-4V-1.55B Eutectic Alloy, Metallurgical and Materials Transactions A 39(2) (2008) 402-416.
[162] S.Q. Wu, Y.J. Lu, Y.L. Gan, T.T. Huang, C.Q. Zhao, J.J. Lin, S. Guo, J.X. Lin, Microstructural evolution and microhardness of a selective-laser-melted Ti–6Al–4V alloy after post heat treatments, Journal of Alloys and Compounds 672 (2016) 643-652.
[163] G. Yu, Z. Li, Y. Hua, H. Liu, X. Zhao, W. Li, X. Wang, The Effects of Post Heat Treatment on the Microstructural and Mechanical Properties of an Additive-Manufactured Porous Titanium Alloy, Materials (Basel) 13(3) (2020) 593.
[164] E. Wycisk, S. Siddique, D. Herzog, F. Walther, C. Emmelmann, Fatigue Performance of Laser Additive Manufactured Ti–6Al–4V in Very High Cycle Fatigue Regime up to 10^9 Cycles, Frontiers in Materials 2 (2015).
[165] F.X. Gil Mur, D. Rodríguez, J.A. Planell, Influence of tempering temperature and time on the α'-Ti-6Al-4V martensite, Journal of Alloys and Compounds 234(2) (1996) 287-289.

[166] G. Cui, B. Yang, J. Hou, W. Chen, W. Zhang, The Sticking Out Mechanism and Growth of TiB Whiskers from TiBw/Ti-6Al-4V Composites during Sintering, Metals 10(11) (2020) 1467.
[167] B. Sarma, N.M. Tikekar, K.S. Ravi Chandran, Kinetics of growth of superhard boride layers during solid state diffusion of boron into titanium, Ceramics International 38(8) (2012) 6795-6805.
[168] M. Kulka, N. Makuch, P. Dziarski, A. Piasecki, A. Miklaszewski, Microstructure and properties of laser-borided composite layers formed on commercially pure titanium, Optics & Laser Technology 56 (2014) 409-424.
[169] M. Keddam, S. Taktak, Characterization and diffusion model for the titanium boride layers formed on the Ti6Al4V alloy by plasma paste boriding, Applied Surface Science 399 (2017) 229-236.
[170] Z.Y. Zhao, L. Li, P.K. Bai, Y. Jin, L.Y. Wu, J. Li, R.G. Guan, H.Q. Qu, The Heat Treatment Influence on the Microstructure and Hardness of TC4 Titanium Alloy Manufactured via Selective Laser Melting, Materials (Basel) 11(8) (2018).
[171] Q. Huang, X. Liu, X. Yang, R. Zhang, Z. Shen, Q. Feng, Specific heat treatment of selective laser melted Ti–6Al–4V for biomedical applications, Frontiers of Materials Science 9(4) (2015) 373-381.
[172] Z. Liu, G. Welsch, Effects of oxygen and heat treatment on the mechanical properties of alpha and beta titanium alloys, Metallurgical Transactions A 19(3) (1988) 527-542.
[173] K.S.R. Chandran, K. Panda, S. Sahay, TiBw-reinforced Ti composites: Processing, properties, application prospects, and research needs, JOM 56 (2004) 42-48.
[174] H. Attar, M. Bönisch, M. Calin, L.C. Zhang, K. Zhuravleva, A. Funk, S. Scudino, C. Yang, J. Eckert, Comparative study of microstructures and mechanical properties of in situ Ti–TiB composites produced by selective laser melting, powder metallurgy, and casting technologies, Journal of Materials Research 29(17) (2014) 1941-1950.
[175] W.D. Callister, D.G. Rethwisch, Fundamentals of Materials Science and Engineering: An Integrated Approach, 4th Edition: An Integrated Approach, Wiley, 2011.
[176] Y.T. Lee, G. Welsch, Young's modulus and damping of Ti・6Al・4V alloy as a function of heat treatment and oxygen concentration, Materials Science and Engineering: A 128(1) (1990) 77-89.
[177] A.I. Kahveci, G.E. Welsch, Hardness versus strength correlation for oxygen-strengthened Ti-6Al-4V alloy, Scripta metallurgica et materialia 25(8) (1991) 1957-1962.
[178] M.Z. Butt, P. Feltham, Solid-solution hardening, Journal of Materials Science 28(10) (1993) 2557-2576.
[179] H. Neuhäuser, Mechanical Properties of Solid Solutions and Related Topics, in: J. Lépinoux, D. Mazière, V. Pontikis, G. Saada (Eds.), Multiscale Phenomena in Plasticity: From Experiments to Phenomenology, Modelling and Materials Engineering, Springer Netherlands, Dordrecht, 2000, pp. 99-116.
[180] T. Gladman, Precipitation hardening in metals, Materials Science and Technology 15(1) (1999) 30-36.
[181] P. Zhang, S.X. Li, Z.F. Zhang, General relationship between strength and hardness, Materials Science and Engineering: A 529 (2011) 62-73.
[182] D. Tabor, The Hardness of Metals, Clarendon Press, Oxford, 1951.

[183] Z. Fan, On the young's moduli of Ti-6Al-4V alloys, Scripta metallurgica et materialia 29(11) (1993) 1427-1432.
[184] Z. Fan, Microstructure and Mechanical Properties of Multiphase Materials, Department of Materials Science and Technology, University of Surrey, 1993.
[185] Y.T. Lee, M. Peters, G. Welsch, Elastic moduli and tensile and physical properties of heat-treated and quenched powder metallurgical Ti-6Al-4V alloy, Metallurgical Transactions A 22(3) (1991) 709-714.
[186] G. Lütjering, J.C. Williams, Titanium, Springer Berlin Heidelberg, 2007.
[187] J.R.S. Martins, Jr., R.O. Araújo, T.A.G. Donato, V.E. Arana-Chavez, M.A.R. Buzalaf, C.R. Grandini, Influence of Oxygen Content and Microstructure on the Mechanical Properties and Biocompatibility of Ti-15 wt%Mo Alloy Used for Biomedical Applications, Materials (Basel) 7(1) (2014) 232-243.
[188] T. Sugita, K. Ueda, Y. Kanemura, Material removal mechanism of silicon nitride during rubbing in water, Wear 97(1) (1984) 1-8.
[189] H. Tomizawa, T.E. Fischer, Friction and Wear of Silicon Nitride and Silicon Carbide in Water: Hydrodynamic Lubrication at Low Sliding Speed Obtained by Tribochemical Wear, A S L E Transactions 30(1) (1987) 41-46.
[190] J. Xu, K. Kato, Formation of tribochemical layer of ceramics sliding in water and its role for low friction, Wear 245(1) (2000) 61-75.
[191] S. Jahanmir, Y. Ozmen, L. Ives, Water Lubrication of Silicon Nitride in Sliding, Tribology Letters 17 (2004) 409-417.
[192] N. Liu, J. Wang, B. Chen, F. Yan, Tribochemical aspects of silicon nitride ceramic sliding against stainless steel under the lubrication of seawater, Tribology International 61 (2013) 205-213.
[193] M. Kalin, Influence of flash temperatures on the tribological behaviour in low-speed sliding: a review, Materials Science and Engineering: A 374(1) (2004) 390-397.
[194] J. Zhang, Z. Wang, W. Chen, H. Liao, M. Zeng, S. Ma, Wear in Silicon Nitride Sliding Against Titanium Alloy Pairs at Different Loads Under Artificial Seawater Lubrication, Frontiers in Materials 6(155) (2019).
[195] I. Hutchings, P. Shipway, Tribology: Friction and Wear of Engineering Materials, Elsevier Science, 2017.
[196] I.Y. Kim, B.J. Choi, Y.J. Kim, Y.Z. Lee, Friction and wear behavior of titanium matrix (TiB+TiC) composites, Wear 271(9) (2011) 1962-1965.
[197] K. Soorya Prakash, P.M. Gopal, D. Anburose, V. Kavimani, Mechanical, corrosion and wear characteristics of powder metallurgy processed Ti-6Al-4V/B4C metal matrix composites, Ain Shams Engineering Journal 9(4) (2018) 1489-1496.
[198] A. Cerit, M. Karamiş, F. Nair, K. Yildizli, Effect of Reinforcement Particle Size and Volume Fraction on Wear Behavior of Metal Matrix Composites, Journal of the Balkan Tribological Association 12 (2008) 482-489.
[199] A.T. Alpas, J. Zhang, Effect of microstructure (particulate size and volume fraction) and counterface material on the sliding wear resistance of particulate-reinforced aluminum matrix composites, Metallurgical and Materials Transactions A 25(5) (1994) 969-983.
[200] Q. Niu, X. Zheng, W. Ming, M. Chen, Friction and Wear Performance of Titanium Alloys against Tungsten Carbide under Dry Sliding and Water Lubrication, Tribology Transactions 56 (2013).

[201] J. Chen, F.-y. Yan, Tribocorrosion behaviors of Ti–6Al–4V and Monel K500 alloys sliding against 316 stainless steel in artificial seawater, Transactions of Nonferrous Metals Society of China 22(6) (2012) 1356-1365.
[202] J. Chen, Q. Zhang, Q.-a. Li, S.-l. Fu, J.-z. Wang, Corrosion and tribocorrosion behaviors of AISI 316 stainless steel and Ti6Al4V alloys in artificial seawater, Transactions of Nonferrous Metals Society of China 24(4) (2014) 1022-1031.
[203] V. Totolin, V. Pejaković, T. Csanyi, O. Hekele, M. Huber, M. Rodríguez Ripoll, Surface engineering of Ti6Al4V surfaces for enhanced tribocorrosion performance in artificial seawater, Materials & Design 104 (2016) 10-18.
[204] P.D. Miller, J.W. Holladay, Friction and wear properties of titanium, Wear 2(2) (1958) 133-140.
[205] H. Singh, M. Hayat, H. Zhang, P. Cao, The decomposition of Si3N4 in titanium and its effect on wear properties, Wear 420 (2019).
[206] M.M. Khruschov, Principles of abrasive wear, Wear 28(1) (1974) 69-88.
[207] E. Hornbogen, The role of fracture toughness in the wear of metals, Wear 33(2) (1975) 251-259.
[208] A.G. Atkins, Toughness in wear and grinding, Wear 61(1) (1980) 183-190.
[209] W.C. Oliver, R. Hutchings, J.B. Pethica, I.L. Singer, G.K. Hubler, Hardness as a Measure of Wear Resistance, MRS Proceedings 27 (1983) 603.
[210] J.F. Archard, Contact and Rubbing of Flat Surfaces, Journal of Applied Physics 24(8) (1953) 981-988.
[211] J. Hu, H. Song, S. Sandfeld, X. Liu, Y. Wei, Breakdown of Archard law due to transition of wear mechanism from plasticity to fracture, Tribology International 173 (2022) 107660.
[212] Y. Tang, H. Pan, D.Y. Li, Contribution of cold-work to the wear resistance of materials and its limitation – A study combining molecular dynamics modeling and experimental investigation, Wear 476 (2021) 203642.
[213] W.A. Glaeser, R.C. Erickson, K.F. Dufrane, J. Kannel, Tribology : the science of combatting wear, Lubrication Engineering 50 (1994) 121-124.

Appendix

Table A.1: Mechanical properties of TMCs reported in literature [34].

TiB vol. %	Boron Source	Matrix	Process	Properties							Comments	Ref.
				VHN (or HRA)	Yield Strength (MPa)	UTS (MPa)	Ductility %	Young's Modulus (GPa)	Flexural Strength (MPa)	K_{1C} (MPa.m$^{1/2}$)		
0	–	Ti-6Al-4V	C+E+H	–	986	1035	–	110	–	39.9	–	41
0	–	Ti-22Al-27Nb	PM+HR+H	–	701	848	6.8	–	–	–	–	42
0	–	Ti	VAR+HS	–	164	179	20.7	109	–	–	–	43
3.1	B	Ti-6Al-4V	C+E+H	–	1041	1156	–	129	–	44	–	41
3.9	TiB_2	Ti-6Al-4V	RS+HIP	453	–	–	–	123.5	–	–	–	44
3.9	TiB_2	Ti-6Al-4V	RS+H+ HIP+F	526	–	–	–	130	–	–	–	44
5	TiB_2	Ti-6Al-4V	CS+HIP	~440	–	–	–	–	–	–	Ti added to matrix	36
5	MoB	Ti-6Al-4V	CS+HIP	~405	–	–	–	–	–	–	Mo added to matrix	36
5	CrB	Ti-6Al-4V	CS+HIP	~350	–	–	–	–	–	–	Cr added to matrix	36
5	B	Ti	VAR (MACS) +HS	–	639	787	12.5	121	–	–	–	43
5	B	Ti-4.0Fe-7.3Mo	SPS	–	–	–	–	~132	~1284	~9.7	Density ~100%	7
6.5	B	Ti-22Al-27Nb	IM+HR+H	–	818	992	4.0	–	–	–	–	42
6.5	B	Ti-22Al-27Nb	PM+HR+H	–	1068	1260	2.3	–	–	–	–	42
7.1	TiB_2	Ti-6Al-4V	RS+HIP	548	–	–	–	130.8	–	–	–	44
7.1	TiB_2	Ti-6Al-4V	RS+H+ HIP+F	550	–	–	–	132.8	–	–	–	44
10	B	Ti-6Al-4V	MA+HIP	–	–	–	0.25	136.6	–	–	–	45
10	B	Ti-4.0Fe-7.3Mo	SPS	–	–	–	–	137	1560	9.57	Density ~99.5%	7
10	B	Ti	VAR (MACS) +HS	–	706	902	5.6	131	–	–	–	43
10	–	Ti-24Al-10Nb (at. %)	PM+HIP	–	–	695	0.0	–	–	–	Specimens failed before yielding	4
10	TiB_2	Ti-6Al-4V	CS+HIP	~550	–	–	–	–	–	–	Ti added to matrix	36
10	CrB	Ti-6Al-4V	CS+HIP	~430	–	–	–	–	–	–	Cr added to matrix	36
10	TiB_2	Ti-4Fe-7.3Mo	MA+SPS	–	–	–	–	146	1007	8.64	Density 99.60%	31
11	TiB_2	Ti-6Al-4V	GA+HIP/ Extrusion		1315	1470	3.1	144	–	–	–	46
15	B	Ti	VAR (MACS) +HS	–	842	903	0.4	139	–	–	–	43
15	–	Ti-5Al-2.5Fe	PM+HIP	–	–	1092	0.0	151	–	–	Specimens failed before yielding	4
15	B	Ti-4.0Fe-7.3Mo	SPS	–	–	–	–	~145	~1053	~8.2	Density ~98.8%	7
15	CrB	Ti-6Al-4V	CS+HIP	~470	–	–	–	–	–	–	Cr added to matrix	36
15	TiB_2	Ti-6Al-4V	CS+HIP	~630	–	–	–		–	–	Ti added to matrix	36
20	TiB_2	Ti	RHP	550	–	–	–	160	–	–	–	2

Table A.1 Continued: Mechanical properties of TMCs reported in literature [34].

Table 1 continued

TiB vol. %	Boron Source	Matrix	Process	Properties							Comments	Ref.
				VHN (or HRA)	Yield Strength (MPa)	UTS (MPa)	Ductility %	Young's Modulus (GPa)	Flexural Strength (MPa)	K_{1C} ($MPa.m^{1/2}$)		
20	TiB_2	Ti-6Al-4V	RHP	580	–	–	–	–	–	–	–	2
20	TiB_2	Ti	PM	–	–	673	0.0	148	–	–	–	46
20	TiB_2	Ti-6Al-4V	MA+HIP	–	1170		2.5	154	–	–	–	46
20	B	Ti-4.0Fe-7.3Mo	SPS	–	–	~7.7	–	~160	~905	–	Density ~97.8%	7
20	TiB_2	Ti-6Al-4V	PM+E MA+HP+E	–	1181	1215	0.5	170	–	–	TiB aligned	33
20	TiB_2	Ti-6Al-4V	CS+HIP	~710	–	–	–	–	–	–	Ti added to matrix	36
20	TiB2	Ti-6Al-4V	MA+HP	–	–	1018	0.1	145	–	–	TiB randomly oriented	33
30	B	Ti-4.3Fe-7Mo-1.4Al-1.4V	MA+CIP+ Sintering +Hot swaging	–	–	1700	0.5	160	–	–	–	4
34	B	Ti-6.4Fe-10.3Mo	PM+HP	–	–	736	0.5	163	–	–	Specimens failed before yielding	26
34	B	Ti-24.3Mo	PM+HP+HT	–	–	1105	0.9	171	–	–	Specimens failed before yielding	26
34	B	Ti-53Nb	PM+HP+HT	–	710	724	1.7	122	–	–	Specimens failed before yielding	26
40	TiB_2	Ti-6Al-4V	PM+E MA+HP+E	–	–	864	0.0	210	–	–	TiB aligned	33
~40	B	Ti	SHS/ PHIP	(82.7 HRA)	–	140	–	191.5	193	6.11	Density 94.3%	30
~50	B	Ti	SHS/ PHIP	–	–	224	–	227	449	–	Density >94%	30
54	TiB_2	Ti	RHP	–	–	–	–	210	–	–		21
~60	B	Ti	SHS/ PHIP	(84.3 HRA)	–	280	–	271	515	6.22	Density 97.04%	30
67	TiB_2	Ti	RHP	1351	–	–	–	–	350	–	TiB particles	27
69	TiB_2	Ti	RHP	–	–	–	–	276	–	–	–	21
~70	B	Ti	SHS/PHIP	(87.8 HRA)	–	248.8	–	326	416.4	6.15	Density 98.45%	30
~80	B	Ti	SHS/ PHIP	(86.7 HRA)	–	207	–	391	277	5.23	Density 97.57%	30
83	TiB_2	Ti	RHP		–		–	366	–	–	–	21
100	B	Ti	SHS/PHIP	(87.1 HRA)	–	103	–	550	225	3.36	Density 96.86%	30

PM = Powder Metallurgy Processing, F = Forging, GA = Argon Gas Atomization, MA = Mechanical Alloying, RS = Rapidly Solidified, H = Heat Treated, E = Extrusion, CS = Combustion Synthesis, SHS = Self Propagating High Temperature Synthesis, RHP = Reactive Hot Pressing, HIP = Hot Isostatic Pressing, PHIP = Pseudo Hot Isostatic Pressing, DTA = Differential Thermal Analysis, SPS = Spark Plasma Sintering, HP = hot pressing, HR = hot rolling, YS = Yield Strength, VHN = Vickers Hardness Number, HRA = Rockwell Hardness (scale A), MACS = Melt Assisted Combustion Synthesis, HS = Hot Swaging, VAR = Vacuum Arc Remelting, ~ = Data extracted from plots (in the TiB volume % column it means value is in weight %)